Dynamics of Electronic Excitations in Carbon Nanotube Composites

by

Amirhossein Davoody

A dissertation submitted in partial fulfillment of
the requirements for the degree of

Doctor of Philosophy
(Electrical and Computer Engineering Department)

at the
UNIVERSITY OF WISCONSIN-MADISON
2016

Date of final oral examination: 12/8/2016

The dissertation is approved by the following members of the Final Oral Committee:

Irena Knezevic, Professor, Electrical and Computer Engineering
Michael Arnold, Associate Professor, Material Science and Engineering
Paul Evans, Professor, Material Science and Engineering
Mikhail Kats, Assistant Professor, Electrical and Computer Engineering
Luke Mawst, Professor, Electrical and Computer Engineering
Martin Zanni, Professor, Chemistry

To my beloved parents and my lovely wife.

ACKNOWLEDGMENTS

This dissertation was only possible thanks to the help and support of many people. I apologize that I am not able to list all the people to whom I feel indebted.

Firstly, I would like to express my sincere gratitude to my advisor Prof. Irena Knezevic for the continuous support of my PhD study and related research, for his patience, motivation, and immense knowledge. His guidance and encouragement helped me in all the time of research and writing of this thesis. I could not have imagined having a better advisor and mentor for my Ph.D study.

Besides my advisor, I would like to thank the rest of my thesis committee Prof. Paul Evans, Prof. Mikhail Kats, Prof. Luke Mawst, and Prof. Martin Zanni, for their insightful comments. Special thanks goes to Prof. Michael Arnold for stimulating discussions and critique throughout different stages of this work.

I would like thank my all my fellow labmates, past and present, for creating an enjoyable research environment. I would like to especially thank Dr. Edwin Ramayya for his guidance in the early stage of my graduate studies. I would also like to thank Farhad Karimi for the many useful and stimulating discussions we had over the past couple of years. I am also grateful to all of my friends in Madison and back home, especially Amin Momeni for his true friendships during all the years in Madison.

I would like to thank my parents and grandparents for their support in every aspect of my life and providing the best role models for me. My gratitude also goes to my brother and sister who made me feel connected to home. Last but not least, I would like to thank my wife, Elham, who shared the burden of the last year of my graduate studies by my side.

DISCARD THIS PAGE

TABLE OF CONTENTS

Page

DISCARD THIS PAGE

LIST OF TABLES

DISCARD THIS PAGE

LIST OF FIGURES

Appendix
Figure Page

Appendix
Figure Page

ABSTRACT

Carbon nanotubes (CNTs) are quasi-one-dimensional structures with a unique set of optical and electronic properties. Today, CNT composites are studied as a suitable candidate for photovoltaic applications owing to the tunable band gap, excellent carrier mobility, and chemical stability of CNTs. Improving the efficiency of CNT-based photovoltaic devices is possible through understanding the dynamics of electronic excitations (excitons) in CNT composites. In the past two decades, the intratube dynamics of excitons in CNTs have been studied extensively. However, the physical processes that determine the efficiency of photovoltaic devices depend on intertube exciton dynamics. There have been a number of measurements of the exciton transfer (ET) rates in CNTs, but the reported rates differ widely, within two orders of magnitude, owing to complexity in sample preparation and measurement. This dissertation theoretically studies the resonant and nonresonant ET mechanism in semiconducting CNT composites.

In the first part, we compute the resonant exciton-transfer (RET) rate between semiconducting single-wall carbon nanotubes (SWNTs). We show that the main reasons for the wide range of measured ET rates reported in the literature are (1) exciton confinement in local quantum wells stemming from disorder in the environment and (2) exciton thermalization between dark and bright states due to intratube scattering. The SWNT excitonic states are calculated by solving the Bethe-Salpeter equation within the GW approximation using tight-binding basis functions. The RET rates due to intertube Coulomb interaction are computed via first-order Fermi's Golden Rule. In pristine samples, the RET rate between

parallel (bundled) SWNTs of similar chirality is very high ($\sim 10^{14}$ s^{-1}), while the ET rate for dissimilar or nonparallel tubes is considerably lower ($\sim 10^{12}$ s^{-1}). Exciton confinement reduces the RET rate between same-chirality parallel SWNTs by two orders of magnitude but has little effect otherwise. Consequently, the RET rate in most measurements will be on the order of 10^{12} s^{-1}, regardless of the tube relative orientation or chirality. Exciton thermalization between bright and dark states further reduces the ET rate to $\sim 10^{11}$ s^{-1}. The RET rate also increases with increasing temperature and decreases with increasing dielectric constant of the surrounding medium.

In the second part, we theoretically investigate the phonon-assisted nonresonant exciton transfer (nRET) rates by using second-order Fermi's Golden Rule. In nRET, exciton hopping is a result of a two-step process: intratube exciton–phonon scattering and intertube Coulomb-mediated exciton hopping. Usually, the second-order processes are a few order of magnitude slower than the first-order processes (such as RET) due to their second-order nature, in which two scattering events happen simultaneously. However, we find that the second-order nRET is as fast as RET ($\sim 10^{12}$ s^{-1}), owing to the high density of phononic states that facilitates the second-order process. We also find that nRET facilitates the hopping of dark excitons with large angular momentum into bright excitons with the same rate as bright excitons, unlike the first-order RET, which yields dark-exciton hopping with at least two orders of magnitude smaller rates than their bright counterparts. This finding is important because of the experimental difficulties in studying the dynamics of dark excitons, which are invisible to the usual measurement techniques.

Chapter 1

Introduction

Carbon nanotubes (CNTs) are thin and hollow cylindrical nanostructures made of carbon atoms. These carbon-based structures were discovered by Iijima *et al.* in the form of multi-wall carbon nanotubes (MWNT) and single-wall carbon nanotubes (SWNT) in 1991 and 1993, respectively [3, 4]. SWNTs have a cylindrical shape of various lengths and diameters, on the order of 1 μm and 1 nm, respectively. SWNTs are regarded as quasi-one-dimensional (1D) materials because of their high aspect ratio of length to diameter. One can, in theory, create a SWNT by wrapping a single-atom-thick layer of graphite (known as graphene) into a cylinder. SWNTs are specified by a pair of integers, (n, m), called the chiral vector. Depending on the value of the chiral vector, a SWNT can be either metallic or semiconducting. It has been shown that a third of chiral vectors lead to SWNTs with metallic behavior, while the rest create SWNTs with semiconducting behavior [5]. Owing to their quasi-one-dimensional strucuture, SWNTs have unique electronic properties, which suggest many potential applications of SWNTs, such as logical circuits, metallic wires, nanotube transistors, and optical devices [6, 7, 8].

In particular, recent improvements in the processing [9, 10] and suitable chemical [11, 12] and optical [13] properties of CNTs have enabled the application of CNT-based composites in thin-film solar cells. A schematic of the general structure of a thin-film solar cell is shown in Fig. 1.1. CNTs have the potential to be used in almost all of these layers. Small-diameter semiconducting HiPco CNTs[1] are used in the active layers of thin-film solar cells because

[1]Carbon nanotubes grown via a popular CVD emthod which involves high-pressure carbon monoxcide.

of their ability to form type-II heterojunctions with polymers [14, 11]. The valence band in large-diameter semiconducting P2 CNTs[2] is aligned with perovskites and organic polymers and enables their use as an interfacial hole-transport layer [15, 16]. Moreover, tunable work function, low sheet resistance, and narrow optical absorption in metallic CNTs makes them suitable for transparent conductive layers [17]. Understanding the time response and dynamics of optically induced electronic excitations in SWNTs is fundamental to improving the operation of these devices.

Various aspects of the dynamical behavior of electronic excitations in SWNTs have been studied (see Sec. 1.2). Many studies point out the importance of Coulomb interaction between neighboring SWNTs on the radiative and nonradiative excitation lifetime [18, 19, 20]. The purpose of this dissertation is to investigate the dynamics of electronic excitations between SWNTs. Here, we calculate the Coulomb-interaction matrix element by considering the many-body nature of electronic excitations in SWNTs. We study the effect of various relevant parameters on the Coulomb interaction strength. We calculate the resonant and nonresonant intertube transfer rate of the electronic excitations in SWNT. From now on, we refer to SWNTs simply as CNTs, unless noted otherwise.

1.1 Electronic excitations in single-wall carbon nanotubes

Optical spectroscopy methods, such as the resonance Raman spectroscopy (RRS) and band-gap photoluminescence (PL), provide powerful tools for investigating the geometry and optical properties of CNTs in different samples. They are used to characterize photo-induced electronic transitions[3] between the van Hove singularities (VHSs) in the density of states (DOS), which originate from the 1D structure of CNTs. The electronic transition, S_{ij}, denotes the transition between the i-th VHS in the valence band and the j-th VHS in

[2]Carbon nanotubes which are produced by the arc-discharge growth method.

[3]These electronic transitions result in neutrally charged excitations. These excitations are different than the charges excitations which are created by adding/subtracting an electron from the system.

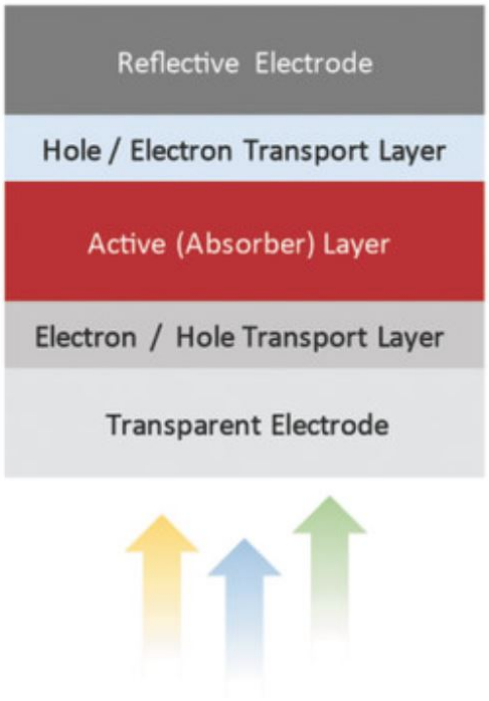

Figure 1.1: Schematic of the general of structure of thin-film solar cells. Figure reproduced from Ref. [1].

the conduction band (i and j increase with increasing distance from the Fermi level). The Kataura plot gives the energy of S_{ii} transitions (E_{ii}) as a function of the tube diameter (d_t) or inverse diameter ($1/d_t$) [13, 21]. The energies in the Kataura plot are arranged in bands ($E_{11}^S, E_{22}^S, E_{11}^M$, etc.) corresponding to electronic transitions S_{ii} in semiconducting and metallic CNTs [Fig. 1.2(a)].

Some important aspects of the electronic transition energies, E_{ii}, such as the dependence on the tube diameter and chirality vector, could be interpreted within the context of a simple noninteracting electron model [21, 22]. However, comparison of the experimental results with noninteracting electron models, such as the simple tight-binding, made it clear that such models underestimate the electronic transition energies [2] [Fig. 1.2(a)]. Many theoretical calculations and experimental measurements have shown the important role of electron–electron (e-e) and electron–hole (e-h) interactions in determining the transition energies [23, 24, 25, 26, 27, 28, 29, 30, 31, 32].

When an electron is excited through photon absorption, an attractive Coulomb force between the excited electron in the conduction band and the hole in valence results in the formation of bound states between the electron and the hole, which is known as an *excitonic state*. The attractive Coulomb force reduces the energy of the photo-induced electronic transition. This reduction in the transition energy is known as the *exciton binding energy*. The electron–electron interaction acts as a repulsive force to add an additional electron to the ground state of the electron gas. This repulsive force is shown in the form of a self-energy, Σ, that increases the effective band gap [Fig. 1.2(b)]. The total effect of many-body interactions is an increase of E_{ii} transition energies over the single-particle tight-binding-model prediction [Fig. 1.2(b)]. These many-body effects generally hold for photo-induced electronic excitations in any type of material. However, the exciton binding energies are usually small (~ 10 meV) in three-dimensional bulk materials owing to the strong screening of Coulomb interaction by the valence band electrons. Therefore, electrons in bound excitonic states are only observable at low temperatures (excitons thermally dissociate when thermal energy becomes comparable to the binding energy). In contrast, the Coulomb interaction

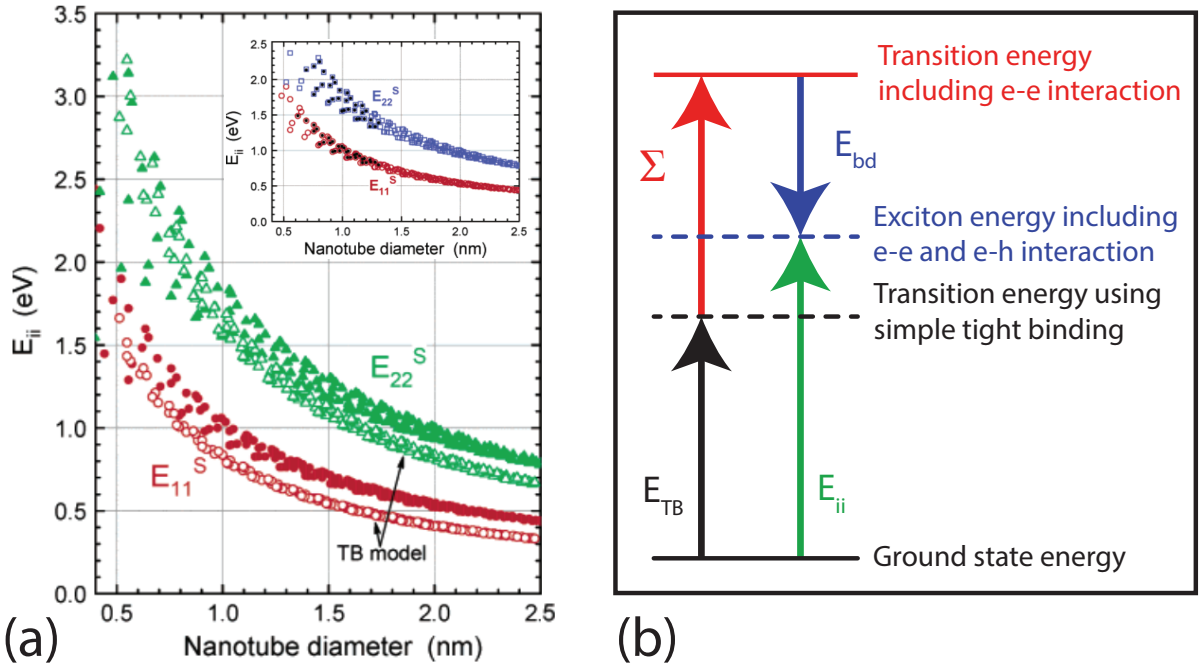

Figure 1.2: (a) Comparison between the Kataura plot based on the simple tight binding model (open symbols) and the empirical model (solid symbols). Inset shows comparison of the empirical model (open symbols) with the experiments (solid symbols). Figure reproduced from Ref. [2]. (b) Schematic of the role of electron–electron and electron–hole interactions in determining the electronic transition energy, E_{ii}.

between an electron and a hole in a CNT is much stronger because of the 1D structure [33] and the exciton binding energy can be as large as 1 eV [24, 34].

Multiple theoretical studies have shown the importance of excitonic effects in CNTs. Early work by Ando, in 1997, addressed excitons in CNTs using a static screened Hartree-Fock approximation [23]. Later on, a variational approach was used to extract a power law for the dependence of the exciton binding energy on the nanotube radius [29]. Although the *ab initio* calculations of the electronic and optical properties of CNTs have shown good agreement with measurements [27, 35, 36, 37], these types of calculations are computationally expensive and difficult to perform on a wide range of CNT chiralities. Therefore, an intermediate levels of theoretical complexity was used to study the family behavior of excitons in CNTs [38, 28]. This intermediate approach is based on solving the Bethe-Salpeter equation (a more comprehensive version of the two-body Schrödinger equation) in the basis of tight-binding wave functions, where e–e interactions are taken into account through the *GW* approximation.

In this work, we use this intermediate approach to calculate exciton wave functions and energies in CNTs.

1.2 Dynamics of electronic excitations in carbon nanotube systems

Carbon nanotubes are direct-bandgap materials. Upon the absorption of a photon, an exciton is created, which can go through a number of dynamical process such as intertube exciton transfer, intratube exciton relaxation, and exciton decay. The exciton decay happens through electron–hole recombination via radiative or nonradiative processes. The quantum efficiency of radiative exciton decay in CNT samples is very sensitive to the sample preparation method. This dependence underlines the importance of intertube dynamical processes. Normally, in samples where semiconducting CNTs bundle together and form CNT fibers, the absorption and emission spectra broaden owing to the interaction between CNTs. The presence of metallic CNTs in the bundles provides a nonradiative pathway for exciton decay

through exciton transfer from semiconducting tubes to zero-bandgap metallic tubes. Therefore, the radiative decay process is most efficient in samples where the CNTs are prevented from bundling by wrapping each CNT in a cylindrical micelle [18]. As we can see, the intertube interaction plays an important role even in understanding the intratube dynamics of electronic excitations in CNTs.

In the next two sections, we review some previous research studies on the intratube exciton dynamics and intertube exciton transfer.

1.2.1 Intratube exciton dynamics

Excitonic states in CNTs are divided into various categories among which only a few can interact with light within the dipole approximation [37]. Figure 1.3 shows a cartoon of different intratube relaxation processes that are possible in an isolated CNT.

The time-resolved spectroscopy of isolated CNTs shows radiative lifetimes ranging from 10 ns [39] to 110 ns [40]. However, theoretical analysis predicts an intrinsic radiative lifetime of 10 ps for the lowest bright excitonic states [37]. The radiative lifetime increases rapidly with increasing exciton center-of-mass momentum. The discrepency between theory and experiment is explained by exciton scattering between bright and low-energy dark excitonic states [41, 37]. The interband exciton relaxation between triplet[4] (dark) and singlet[5] (bright) excitonic states, mediated by lattice vibrations, is the reason for the measured radiative lifetime of 10 ns [41, 37]. These relaxation processes are intrisic to CNTs and present in all measurements. However, sample-dependent extrinsic scattering sources that break the symmetry of excitonic states play a central role in further decreasing the radiative decay rate. These extrinsic scattering sources relax excitons to the symmetric excitonic states[6], which increases the fluorescent lifetime to 100 ns [41].

Although the radiative lifetime of excitons is relatively long, the competing nonradiative decay processes are generally much faster. Time-resolved spectroscopy measurements

[4]Excitons with spin equal to one.
[5]Excitons with spin equal to zero.
[6]These excitonic states are optically in-active based on symmetry considerations.

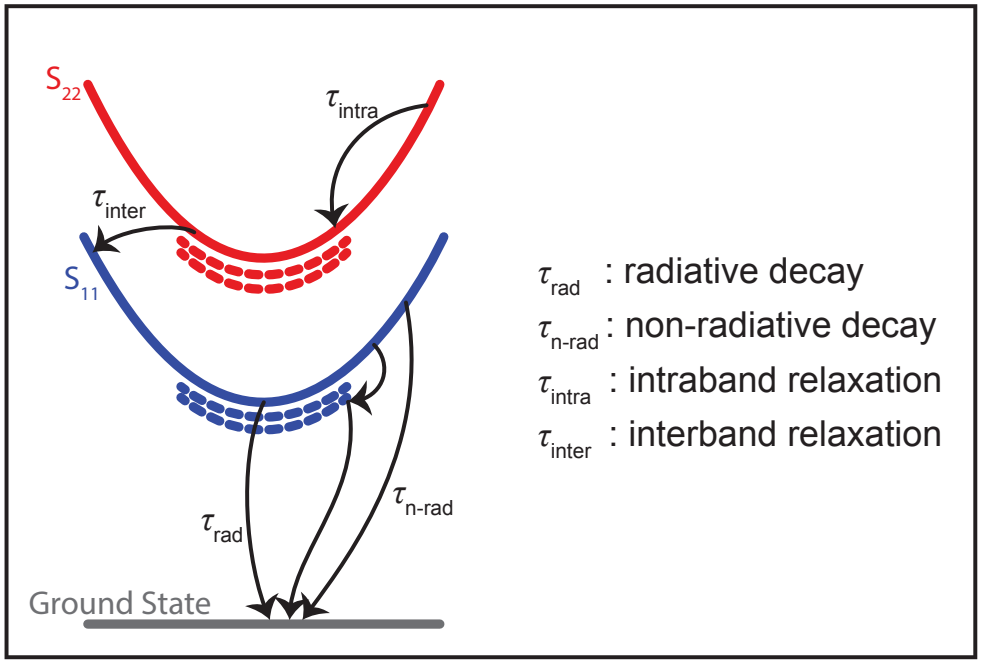

Figure 1.3: Various intraband relaxation processes. Solid dispersion curves represent the optically active excitonic states. Dashed dispersion curves represent the optically inactive excitonic states.

Relaxation process		time constant
radiative	τ_{rad}	$10 - 110$ ns
nonradiative	$\tau_{\text{n-rad}}$	$10 - 200$ ps
intraband	τ_{intra}	$0.2 - 1.2$ ps
interband	τ_{inter}	$5 - 20$ ps

Table 1.1: Time constants of intratube relaxation processes.

of fluorescence from isolated CNTs show nonradiative lifetimes of about 10 ps [39, 40]. An investigation of the temperature dependence of nonradiative exciton lifetimes in isolated CNTs shows the appearance of thermally activated nonradiative decay channels with increasing temperature [42]. In this study, the nonradiative decay lifetimes range from 200 to 20 ps for the temperature range between 48 and 182 K. The nonradiative decay channels vary among different samples and depend on impurity and defect concentration.

Studies of the intraband and interband exciton relaxation processes are possible via pump–probe (PP) experiments. An initial pump pulse excites electrons from the ground state, then a second probe pulse (with a much lower intensity) passes through the sample on a periodic basis. The changes in the absorbance of the sample enable us to extract information about the population of excited electrons and their dynamics between excitonic bands. Performing PP measurements on isolated CNT samples showed that the intraband exciton relaxation time constant is $0.2 - 1.2$ ps [43, 44, 19, 39], whereas the interband relaxation time constant is $5 - 20$ ps [44, 43].

Besides the simple relaxation processes mentioned above, there are some second-order pathways, such as exciton–exciton annihilation processes, that can lead to ultrafast interband relaxation with characteristic times on the order of 100 fs [45, 46]. In another experiment, pump–probe spectroscopy on samples with bundles of CNT showed a much faster relaxation process between S_{22} and S_{11} with only 40 fs time constant [47], which points out the importance of intertube interactions.

1.2.2 Intertube exciton dynamics

Excitons transfer between two CNTs due to the electron–electron Coulomb interaction, which is long range [48]. Generally, the intertube exciton transfer (ET) happens through two pathways: ET via direct interaction and ET via exchange interaction (Fig. 1.4). In the process of ET via direct interaction, a virtual photon is emitted by the donor CNT[7] and is absorbed almost simultaneously by the acceptor CNT [8] [49]. In the ET via exchange interaction, the excited electron from the donor CNT tunnels to the acceptor CNT while an electron from the ground state of the acceptor CNT tunnels back to the donor CNT.

There have been a number of measurements of the exciton transfer rates in CNTs, however, the reported rates differ by about two orders of magnitude because of the important role of sample parameters [50]. pump–probe spectroscopy measurements have shown a time constant of about 0.37 ps for the ET process from semiconducting SWNTs to metalic SWNTs [51]. Time-resolved photoluminescence (PL) spectroscopy found the time constants of 0.9 ps and 0.5 ps for the ET from semiconducting SWNTs to metallic and semiconducting SWNTs, respectively [52]. In another study, time-resolved PL spectroscopy has been used to measure the ET between semiconducting SWNTs, with a time constant $\tau \approx 70$ ps [53]. Qian *et al.* used spatial high-resolution optical spectroscopy to estimate the time constant of ET between two nonparallel semiconducting SWNTs as $\tau \approx 0.5$ ps [54]. Using PP spectroscopy, the ET time constant between bundled SWNTs was measured to be $\tau \approx 10$ fs for S_{11} excitons [55]. The same study estimated the S_{22} exciton transfer to be very slow because to momentum mismatch. Another study showed a long-range fast component ($\tau \approx 0.3$ ps), followed by a short-range slow component ($\tau \approx 10$ ps) for the ET process in SWNT films [56]. Grechko *et al.* used a diffusion-based model to explain their measurement of ET process in bundled semiconducting SWNTs samples [57]. They found the time constants of $\tau \sim 0.2 - 0.4$ ps for ET process between bundles of SWNTs and $\tau \approx 7$ ps for ET process inside the SWNT

[7]The CNT that posseses the exciton *before* the transfer process.
[8]The CNT that posseses the exciton *after* the transfer process.

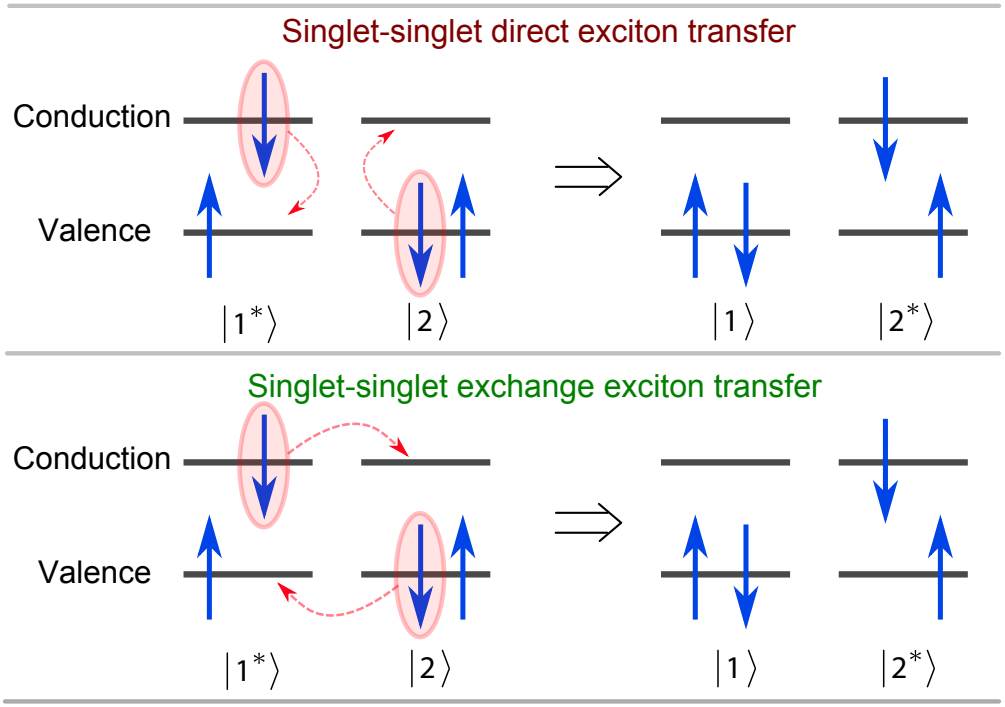

Figure 1.4: (a) Mechanism of intertube exciton transfer via direct Coulomb interaction. (b) Mechanism of intertube exciton transfer via exchange Coulomb interaction.

Transfer process	Experiment	Time constant
Semi. to metal	Maeda [51]	0.37 ps
Semi. to metal	Koyama [52]	0.9 ps
Semi. to semi.	Koyama [52]	0.5 ps
Semi. to semi.	Berger [53]	70 ps
Semi. to semi.	Mehlenbacher [56]	0.3 ps followed by 10 ps
Semi. to semi.	Grechko [57]	0.3 ps intertube, 7 ps intratube
Between nonparallel semi.	Qian [54]	0.5 ps
Between S_{11} of bundled semi.	Lüer [55]	10 fs
Between S_{22} of bundled semi.	Lüer [55]	very slow

Table 1.2: Measurements of intertube exciton transfer time constants.

bundles. A more recent study by Mehlenbacher *et al.* revealed ultrafast S_{22} exciton transfer in semiconducting CNT films [58].

As we can see, despite the large number of experimental data on the ET rate, the underlying mechanisms facilitating ET are relatively unexplored because of the complexities in sample preparation, measurements, and the multitude of pathways through which the ET process can happen. Many difficulties inherent in experiments can be avoided in a theoretical study of the transfer process. However, there have been very limited theoretical studies of the exciton transfer rate between semiconducting SWNTs [59, 60]. Wong *et al.* showed that the ideal dipole approximation (known as the Förster theory) overestimates the exciton transfer rate by three orders of magnitude [59]. Postupna *et al.* showed that the exciton–phonon coupling could have a prominent effect on the exciton transfer process between (6,4) and (8,4) SWNTs [60]. However, none of these studies account for important parameters, such as the existence of low-lying optically dark excitonic states, chirality and diameter of donor and acceptor CNTs, temperature, confinement of excitons, screening due to surrounding media, and the interaction between various exciton subbands, all of which

have been shown, experimentally and theoretically, to play an important role in the exciton dynamics in CNTs [28, 61, 41, 37, 56].

1.3 Outline

This thesis presents a quantum-mechanical study of resonant and nonresonant exciton transfer processes in semiconducting single-wall carbon nanotubes.

In Chapter 2, we present the electronic band structure of CNTs. We introduce the Bethe-Salpeter equation with the GW approximation for the electron–electron interaction which is solved to calculate the excitonic states in CNTs. We calculate the excitonic states in an arbitrary CNT.

In Chapter 3, we introduce the theory of resonant exciton transfer between two arbitrary electronic systems. We apply the theory to the case of two CNTs as the exciton donor and acceptor systems. First, we derive the expressions for the resonant ET rate between confined excitonic states. Then, we derive analytical expressions for the exciton transfer rate between free excitonic states. Finally, we show calculation results for the resonant ET rates in CNTs. We study the effect of various parameters such as exciton confinement, Coulomb screening, and temperature on the resonant ET rates.

Chapter 4 presents a derivation of the exciton–phonon interaction Hamiltonian based on the Su-Schrieffer-Heeger model Hamiltonian. In Chapter 5, we use the exciton–phonon interaction and the Coulomb coupling Hamiltonians that we derived in Chapters 3 and 4 in the second-order Fermi's golden rule to calculate phonon-assisted nonresonant ET rates in CNTs. We show the calculation results for the nonresonant ET rates among bright excitonic states and between bright and dark excitonic states for various CNT chiralities.

Chapter 6 summarizes the main results and discusses some ongoing investigation.

Chapter 2

Electronic Excitations in Carbon Nanotubes

In this Chapter, we review the electronic bandstructure of CNTs. We discuss the process of solving the Bethe-Salpeter equation to calculate the excitonic states in CNTs, which are divided into various classes based on their symmetry and angular momentum.

2.1 Graphene geometry

Graphene has a two-dimensional (2D) honeycomb lattice. The distance between the closest carbon atoms is $a_{CC} \approx 1.42$ Å. The graphene unit cell has two carbon atoms. The underlying lattice is hexagonal, with primitive lattice vectors (also referred to as basis vector)

$$\boldsymbol{a}_1 = a\left(\frac{\sqrt{3}}{2}\hat{\boldsymbol{x}} + \frac{1}{2}\hat{\boldsymbol{y}}\right) \quad , \quad \boldsymbol{a}_2 = a\left(\frac{\sqrt{3}}{2}\hat{\boldsymbol{x}} + \frac{-1}{2}\hat{\boldsymbol{y}}\right), \tag{2.1}$$

where $a = \sqrt{3}a_{CC}$ is the lattice constant.

The reciprocal lattice basis vectors, $\boldsymbol{b}_1$ and $\boldsymbol{b}_2$, are related to the real-space primitive lattice vectors through

$$\boldsymbol{a}_i \cdot \boldsymbol{b}_j = 2\pi\delta_{ij}, \tag{2.2}$$

where δ_{ij} is the Kronecker delta function. The reciprocal lattice basis vectors are

$$\boldsymbol{b}_1 = \frac{2\pi}{a}\left(\frac{1}{\sqrt{3}}\hat{\boldsymbol{x}} + \hat{\boldsymbol{y}}\right) \quad , \quad \boldsymbol{b}_2 = \frac{2\pi}{a}\left(\frac{1}{\sqrt{3}}\hat{\boldsymbol{x}} - \hat{\boldsymbol{y}}\right). \tag{2.3}$$

Figure 2.1 shows the graphene reciprocal lattice basis vectors and the Brillouin zone.

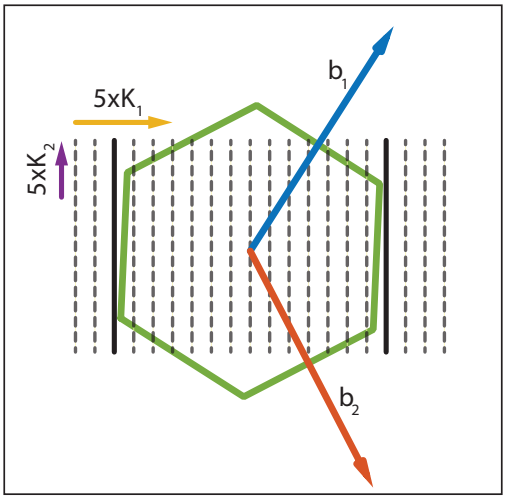

Figure 2.1: Graphene Brillouin zone and the cutting lines of CNT with (7,6) chirality. Bold solid cutting lines represent the degenerate states that pass by the K and K' Dirac points in the graphene Brillouin zone.

2.2 Carbon nanotube geometry

From theoretical point of view, a carbon nanotube is a rolled-up graphene sheet. The chiral vector $\boldsymbol{C}_h$ determines the circumference of the carbon nanotube

$$\boldsymbol{C}_h = n\boldsymbol{a}_1 + m\boldsymbol{a}_2 \quad , \quad L = |\boldsymbol{C}_h| = a\sqrt{n^2 + m^2 + nm}. \tag{2.4}$$

The unrolled graphene sheet has translational symmetry along the axis of carbon nanotube with translational vector $\boldsymbol{T}$:

$$\boldsymbol{T} = t_1\boldsymbol{a}_1 + t_2\boldsymbol{a}_2 \ , \tag{2.5a}$$

where

$$t_1 = \frac{2m+n}{d_R} \quad , \quad t_2 = -\frac{2n+m}{d_R} \quad , \quad d_R = \gcd(2n+m, 2m+n). \tag{2.5b}$$

Therefore, the length of the translational vector is

$$T = |\boldsymbol{T}| = \frac{\sqrt{3}|\boldsymbol{C}_h|}{d_R}. \tag{2.5c}$$

$\boldsymbol{C}_h$ and $\boldsymbol{T}$ define a larger unit cells in the graphene sheet. The total number of number of graphene unit cell in the larger CNT unit cell is

$$N = \frac{2(n^2 + m^2 + nm)}{d_R}. \tag{2.6}$$

The corresponding reciprocal lattice vectors are as follows

$$\boldsymbol{C}_h \cdot \boldsymbol{K}_1 = 2\pi \quad , \quad \boldsymbol{T} \cdot \boldsymbol{K}_1 = 0, \tag{2.7a}$$

$$\boldsymbol{C}_h \cdot \boldsymbol{K}_2 = 0 \quad , \quad \boldsymbol{T} \cdot \boldsymbol{K}_2 = 2\pi, \tag{2.7b}$$

$$\boldsymbol{K}_1 = \frac{1}{N}\left(-t_2\boldsymbol{b}_1 + t_1\boldsymbol{b}_2\right) \quad , \quad \boldsymbol{K}_2 = \frac{1}{N}\left(m\boldsymbol{b}_1 - n\boldsymbol{b}_2\right). \tag{2.7c}$$

2.3 Graphene bandstructure and symmetry

If we neglect the effect of curvature on the orbital overlaps, the carbon-nanotube single-particle bandstructure is based on the graphene bandstructure. Here, we discuss the graphene

bandstructure and its symmetry. In the tight-binding scheme, the single-particle bandstructure is written as

$$\psi_{\alpha \boldsymbol{k}}(\boldsymbol{r}) = \frac{1}{\sqrt{N_u}} \sum_b \sum_u C_{\alpha b}(\boldsymbol{k}) e^{i\boldsymbol{k}.\boldsymbol{R}_{ub}} \phi(\boldsymbol{r} - \boldsymbol{R}_{ub}), \tag{2.8}$$

where $\alpha = c, v$ is the band index. u is the unit cell index. N_u is the total number of unit cells in graphene sheet. $b = A, B$ is the basis atom index inside the unit cell.

The tight-binding wavefunctions and energies are determined by solving the following eigenvalue problem:

$$\begin{bmatrix} \varepsilon_{2p_z} & tf(\boldsymbol{k}) \\ tf^*(\boldsymbol{k}) & \varepsilon_{2p_z} \end{bmatrix} \begin{bmatrix} C_{\alpha A}(\boldsymbol{k}) \\ C_{\alpha B}(\boldsymbol{k}) \end{bmatrix} = \mathcal{E}_a(\boldsymbol{k}) \begin{bmatrix} 1 & sf(\boldsymbol{k}) \\ sf^*(\boldsymbol{k}) & 1 \end{bmatrix} \begin{bmatrix} C_{\alpha A}(\boldsymbol{k}) \\ C_{\alpha B}(\boldsymbol{k}) \end{bmatrix}. \tag{2.9}$$

Here, $f(\boldsymbol{k})$ is the sum of the phase factors over the nearest neighbors given by

$$f(\boldsymbol{k}) = e^{i\boldsymbol{k}.\frac{\boldsymbol{a}_1+\boldsymbol{a}_2}{3}} + e^{i\boldsymbol{k}.\frac{\boldsymbol{a}_1-2\boldsymbol{a}_2}{3}} + e^{i\boldsymbol{k}.\frac{\boldsymbol{a}_2-2\boldsymbol{a}_1}{3}} \tag{2.10}$$

The overlap integrals are

$$\varepsilon_{2p_z} = \int d\boldsymbol{r}\, \phi^*_{2p_z}(\boldsymbol{r}) \hat{\mathcal{H}} \phi_{2p_z}(\boldsymbol{r}), \tag{2.11a}$$

$$t = \int d\boldsymbol{r}\, \phi^*_{2p_z}(\boldsymbol{r}) \hat{\mathcal{H}} \phi_{2p_z}(\boldsymbol{r} - \boldsymbol{R}_{nn}), \tag{2.11b}$$

$$s = \int d\boldsymbol{r}\, \phi^*_{2p_z}(\boldsymbol{r}) \phi_{2p_z}(\boldsymbol{r} - \boldsymbol{R}_{nn}), \tag{2.11c}$$

where $\boldsymbol{R}_{nn}$ is the coordinate of the nearest neighbor atom. We assume ε_{2p_z}, s, and t to be positive quantities.

The energies in this equation are

$$\mathcal{E}_a(\boldsymbol{k}) = \frac{\varepsilon_{2p_z} \pm t|f(\boldsymbol{k})|}{1 \pm s|f(\boldsymbol{k})|}, \tag{2.12}$$

where $(+)$ indicates the conduction band energy and $(-)$ indicates the valence band energy.

The tight-binding coefficients are easily

$$C_{\alpha A}(\boldsymbol{k}) = \frac{1}{\sqrt{2}} \quad , \quad C_{\alpha B}(\boldsymbol{k}) = \pm \frac{1}{\sqrt{2}} \frac{f^*(\boldsymbol{k})}{|f(\boldsymbol{k})|}. \tag{2.13}$$

Using the above relations, we can show the following relations for the wavefunction which are a consequence of the symmetry of graphene lattice

$$C_{cA}(\boldsymbol{k}) = C_{vA}(\boldsymbol{k}) \quad , \quad C_{cB}(\boldsymbol{k}) = -C_{vB}(\boldsymbol{k}) \quad , \quad C_{\alpha b}(-\boldsymbol{k}) = C^*_{\alpha b}(\boldsymbol{k}). \tag{2.14}$$

2.4 Carbon-nanotube bandstructure

If we neglected the effect of curvature of CNTs and the change in screening (many-body effects) due to the quasi-one-dimensional structure of CNTs, the bandstructure of graphene would be identical to the CNT bandstructure, and we would only have to consider the correct values of the wave vectors that corresponds to the periodicity of the wavefunction in the circumference direction. This approximation is enabled by the concept of cutting lines, and is known as the zone-folding technique.

When thinking about a CNT as a rolled-up graphene sheet with periodic wavefunctions in the circumferential direction, one has to bear in mind that this is special in the sense that the lattice has the width of only one unit cell in the circumferential direction, therefore the width of the Brillouin zone is equal to the spacing between the k-vectors in the circumferential direction. Hence, the introduction of the concept of cutting lines is not a very straight forward process.

A weakness of the zone-folding approximation is that it neglects the curvature of the tube walls and many-body effects, which are enhanced by the confinement to 1D. The curvature of the wall and the associated rehybridization of sp^2 to sp^3 orbitals can be relatively easily addressed by a symmetry-adapted nonorthogonal tight-binding model [62]. On the other hand, the many-body effects are much more complicated to capture. These effects are divided into the self-energy part and the electron–hole interaction. The next few sections are dedicated to capturing these many-body effects.

Within the zone-folding technique, the continuous 2D wave vector in the plane of the graphene sheet is replaced by a wave vector that is continuous in the direction of the CNT axis and discrete in the circumferential direction,

$$\boldsymbol{k} = \mu \boldsymbol{K}_1 + k\boldsymbol{K}_2/|\boldsymbol{K}_2|, \tag{2.15}$$

where $\mu = 0, 1, 2, ...$ is an integer quantum number associated with the circumferential direction, and is analogous to the band index (Fig. 2.1).

Assuming the tube axis is aligned with the x-axis and the circumference of the unwrapped graphene sheet is in the y-axis, the wave vectors have the form

$$\boldsymbol{k} = k\hat{\boldsymbol{x}} + \frac{\mu}{r_0}\hat{\boldsymbol{y}}, \tag{2.16}$$

where $r_0 = 2\pi/|\boldsymbol{C}_h|$ is the radius of the tube. Considering the curved structure of CNT, we can write the position of atoms in polar coordinates and convert it to the vector positions in the 2D graphene sheet as

$$\boldsymbol{R}_{ub} = x_{ub}\hat{\boldsymbol{x}} + r_0\theta_{ub}\hat{\boldsymbol{y}} \ . \tag{2.17}$$

Here, x_{ub} (θ_{ub}) is the position (azimuthal angle) of basis atom b in unit cell u along the axis (circumference) of CNT. Therefore, the CNT electronic wavefunction is

$$\psi_{\alpha\boldsymbol{k}}(\boldsymbol{r}) = \frac{1}{\sqrt{N_u}}\sum_b\sum_u C_{\alpha b}(\boldsymbol{k})e^{i(kx_{ub}+\mu\theta_{ub})}\phi(\boldsymbol{r}-\boldsymbol{R}_{ub}). \tag{2.18}$$

This notation becomes useful when we calculate the exciton transfer rate and we have to consider the position of carbon atoms in 3D space instead of a 2D unwrapped graphene sheet.

2.5 General solution of the Bethe-Salpeter equation

In this Section, we will discuss the process of calculating the exciton[1] wavefunction. The exciton wavefunction and energy are calculated by solving the Bethe-Salpeter (BS) equation, which a more complex version of the two-body Schrödinger equation. By writing the BS equation in the basis of the quasi-particle wavefunctions, we get an eigenvalue problem

$$[E_c(\boldsymbol{k}_c) - E_v(\boldsymbol{k}_v)]A_n(\boldsymbol{k}_c,\boldsymbol{k}_v) + \sum_{\boldsymbol{k}'_c,\boldsymbol{k}'_v}\mathcal{K}(\boldsymbol{k}_c,\boldsymbol{k}_v;\boldsymbol{k}'_c,\boldsymbol{k}'_v)A_n(\boldsymbol{k}'_c,\boldsymbol{k}'_v) = \Omega_n A_n(\boldsymbol{k}_c,\boldsymbol{k}_v) \ . \tag{2.19}$$

$E_c(\boldsymbol{k}_c)$ and $E_v(\boldsymbol{k}_v)$ are the quasi-particle energies of electrons with wave vectors $\boldsymbol{k}_c$ and $\boldsymbol{k}_v$ in the conduction and valence bands. n represents all the relevant quantum numbers determining the excitonic state. Ω_n is the exciton energy. $A_n(\boldsymbol{k}_c,\boldsymbol{k}_v)$ is the expansion

[1] bound electron–hole state

coefficient of the exciton wavefunction ($|\mathrm{X}, n\rangle$) in the basis of quasi-particle (electron and hole) wavefunctions (the Tamm-Dancoff approximation)

$$|\mathrm{X}, n\rangle = \sum_{\boldsymbol{k}_c, \boldsymbol{k}_v} A_n(\boldsymbol{k}_c, \boldsymbol{k}_v) \hat{u}^\dagger(\boldsymbol{k}_c) \hat{v}(\boldsymbol{k}_v) |\mathrm{GS}\rangle. \tag{2.20}$$

Here, $|\mathrm{GS}\rangle$ is the ground state where all electrons feel the lowest energy states. Finally, $\mathcal{K}$ is an interaction kernel, which describes the particle–particle interaction. Using the GW approximation [63], we can divide the interaction kernel into two (direct and exchange) terms:

$$\mathcal{K}(\boldsymbol{k}_c, \boldsymbol{k}_v; \boldsymbol{k}'_c, \boldsymbol{k}'_v) = 2\delta_\sigma \mathcal{K}^x(\boldsymbol{k}_c, \boldsymbol{k}_v; \boldsymbol{k}'_c, \boldsymbol{k}'_v) - \mathcal{K}^d(\boldsymbol{k}_c, \boldsymbol{k}_v; \boldsymbol{k}'_c, \boldsymbol{k}'_v), \tag{2.21a}$$

where

$$\begin{aligned} \mathcal{K}^d(\boldsymbol{k}_c, \boldsymbol{k}_v; \boldsymbol{k}'_c, \boldsymbol{k}'_v) =& W(\boldsymbol{k}_c, \boldsymbol{k}'_c; \boldsymbol{k}_v, \boldsymbol{k}'_v) \\ =& \int \mathrm{d}^3\boldsymbol{r}\, \mathrm{d}^3\boldsymbol{r}' \psi^*_{c\boldsymbol{k}_c}(\boldsymbol{r}) \psi_{c\boldsymbol{k}'_c}(\boldsymbol{r}) w(\boldsymbol{r}, \boldsymbol{r}'; \omega = 0) \psi_{v\boldsymbol{k}_v}(\boldsymbol{r}) \psi^*_{v\boldsymbol{k}'_v}(\boldsymbol{r}) \end{aligned} \tag{2.21b}$$

and

$$\begin{aligned} \mathcal{K}^x(\boldsymbol{k}_c, \boldsymbol{k}_v; \boldsymbol{k}'_c, \boldsymbol{k}'_v) =& V(\boldsymbol{k}_c, \boldsymbol{k}_v; \boldsymbol{k}'_c, \boldsymbol{k}'_v) \\ =& \int \mathrm{d}^3\boldsymbol{r}\, \mathrm{d}^3\boldsymbol{r}' \psi^*_{c\boldsymbol{k}_c}(\boldsymbol{r}) \psi_{v\boldsymbol{k}_v}(\boldsymbol{r}) v(\boldsymbol{r}, \boldsymbol{r}') \psi_{c\boldsymbol{k}'_c}(\boldsymbol{r}) \psi^*_{v\boldsymbol{k}'_v}(\boldsymbol{r}). \end{aligned} \tag{2.21c}$$

Here, $\psi_{\alpha\boldsymbol{k}}$ is the quasi-particle wavefunction. w and v are the screened and bare Coulomb interactions. σ is the exciton spin and $\delta_\sigma = 1$ for singlet exciton ($\sigma = 0$) and $\delta_\sigma = 0$ for triplet excitons ($\sigma = 1$).

We use the first-order perturbation theory and the GW approximation to calculate the self-energy corrections in the quasi-particle energies

$$E_c(\boldsymbol{k}_c) = \mathcal{E}_c(\boldsymbol{k}_c) + \Sigma(\boldsymbol{k}_c), \quad E_v(\boldsymbol{k}_v) = \mathcal{E}_v(\boldsymbol{k}_v) + \Sigma_v(\boldsymbol{k}_v). \tag{2.22a}$$

Here, $\mathcal{E}$ is the single-particle state energy and Σ is the self-energy

$$\Sigma_c(\boldsymbol{k}_c) = -\sum_{\boldsymbol{k}'_v} W(\boldsymbol{k}_c, \boldsymbol{k}'_v; \boldsymbol{k}_c, \boldsymbol{k}'_v), \quad \Sigma_v(\boldsymbol{k}_v) = -\sum_{\boldsymbol{k}'_v} W(\boldsymbol{k}_v, \boldsymbol{k}'_v; \boldsymbol{k}_v, \boldsymbol{k}'_v). \tag{2.22b}$$

Furthermore, The screened Coulomb interaction in the direct interaction kernel is in the frequency domain and can be calculated using the random-phase approximation [64, 38]

$$W(\alpha_1\boldsymbol{k}_1, \alpha_2\boldsymbol{k}_2; \alpha_3\boldsymbol{k}_3, \alpha_4\boldsymbol{k}_4) = \frac{V(\alpha_1\boldsymbol{k}_1, \alpha_2\boldsymbol{k}_2; \alpha_3\boldsymbol{k}_3, \alpha_4\boldsymbol{k}_4)}{\kappa\epsilon(\boldsymbol{k}_1 - \boldsymbol{k}_2, \omega = 0)}. \tag{2.23}$$

Here, α_i shows the conduction or valence band of graphene. κ is the static dielectric function, which accounts for the screening effect of environment and core electrons. A typical value of this parameter is $\kappa \sim 2$, however, this value can change dramatically (1 to 7) between different CNT samples. The effect of π-bond electrons is considered in the dielectric function $\epsilon(\boldsymbol{q}, \omega)$ through the Lindhard formula

$$\epsilon(\boldsymbol{q}, 0) = 1 + v(\boldsymbol{q})\Pi(\boldsymbol{q}, 0), \tag{2.24a}$$

$$\Pi(\boldsymbol{q}, 0) = -2 \sum_{\boldsymbol{k},\alpha,\alpha'} \frac{f_{\alpha'}(\boldsymbol{k}+\boldsymbol{q}) - f_{\alpha}(\boldsymbol{k})}{\mathcal{E}_{\alpha'}(\boldsymbol{k}+\boldsymbol{q}) - \mathcal{E}_{\alpha}(\boldsymbol{k}+\boldsymbol{q})} \left| \int \psi^*_{\alpha\boldsymbol{k}}(\boldsymbol{r}) e^{-i\boldsymbol{q}.\boldsymbol{r}} \psi_{\alpha'\boldsymbol{k}+\boldsymbol{q}}(\boldsymbol{r}) \right|^2 \tag{2.24b}$$

where, Π is the polarization and $f_\alpha(\boldsymbol{k})$ is the band occupation number at zero temperature (1 for valence and 0 for conduction). a and a' represent the conduction or valence band in graphene. $\boldsymbol{k}$ and $\boldsymbol{q}$ represent both the continuous 1D wave vector along the tube axis and the discrete circumferential wave vector, there for they are considered to be two-dimensional vectors in the plane of graphene sheet. $v(\boldsymbol{q})$ is the Fourier transform of the bare Coulomb interaction.

Now, we calculate $V(\alpha_1\boldsymbol{k}_1, \alpha_2\boldsymbol{k}_2; \alpha_3\boldsymbol{k}_3, \alpha_4\boldsymbol{k}_4)$ and $\epsilon(\boldsymbol{q}, 0)$ by approximating the quasi-particle wavefunction with tight-binding (TB) model. The bare Coulomb interaction matrix element has the following form

$$\begin{aligned} V(\alpha_1\boldsymbol{k}_1, \alpha_2\boldsymbol{k}_2; \alpha_3\boldsymbol{k}_3, \alpha_4\boldsymbol{k}_4) &= \int \mathrm{d}^3\boldsymbol{r}\, \mathrm{d}^3\boldsymbol{r}' \psi^*_{\alpha_1\boldsymbol{k}_1}(\boldsymbol{r}) \psi_{\alpha_2\boldsymbol{k}_2}(\boldsymbol{r}) v(\boldsymbol{r}, \boldsymbol{r}') \psi_{\alpha_3\boldsymbol{k}_3}(\boldsymbol{r}') \psi^*_{\alpha_4\boldsymbol{k}_4}(\boldsymbol{r}') \\ &= \frac{1}{N_u^2} \sum_{b_1,b_2} \sum_{b_3,b_4} C^*_{\alpha_1 b_1}(\boldsymbol{k}_1) C_{\alpha_2 b_2}(\boldsymbol{k}_2) C_{\alpha_3 b_3}(\boldsymbol{k}_3) C^*_{\alpha_4 b_4}(\boldsymbol{k}_4) \\ &\quad \times \sum_{u_1,u_2} \sum_{u_3,u_4} e^{i(-\boldsymbol{k}_1.\boldsymbol{R}_{u_1 b_1} + \boldsymbol{k}_2.\boldsymbol{R}_{u_2 b_2} + \boldsymbol{k}_3.\boldsymbol{R}_{u_3 b_3} - \boldsymbol{k}_4.\boldsymbol{R}_{u_4 b_4})} \\ \times \int \mathrm{d}^3\boldsymbol{r}\, \mathrm{d}^3\boldsymbol{r}' \phi^*(\boldsymbol{r} - \boldsymbol{R}_{u_1 b_1}) \phi(\boldsymbol{r} - \boldsymbol{R}_{u_2 b_2}) v(|\boldsymbol{r} - \boldsymbol{r}'|) \phi(\boldsymbol{r}' - \boldsymbol{R}_{u_3 b_3}) \phi^*(\boldsymbol{r}' - \boldsymbol{R}_{u_4 b_4}). \end{aligned} \tag{2.25}$$

Now, we use the approximation that the last integral is nonnegligible only when $u_1 b_1 = u_2 b_2 = ub$ and $u_3 b_3 = u_4 b_4 = u'b'$, then the matrix element becomes

$$V(\alpha_1 \boldsymbol{k}_1, \alpha_2 \boldsymbol{k}_2; \alpha_3 \boldsymbol{k}_3, \alpha_4 \boldsymbol{k}_4) = \frac{1}{N_u^2} \sum_{b,b'} C^*_{\alpha_1 b}(\boldsymbol{k}_1) C_{\alpha_2 b}(\boldsymbol{k}_2) C_{\alpha_3 b'}(\boldsymbol{k}_3) C^*_{\alpha_4 b'}(\boldsymbol{k}_4) \sum_{u,u'} e^{i[(\boldsymbol{k}_2 - \boldsymbol{k}_1).\boldsymbol{R}_{ub} + (\boldsymbol{k}_3 - \boldsymbol{k}_4).\boldsymbol{R}_{u'b'}]} \times \int \mathrm{d}^3\boldsymbol{r}\, \mathrm{d}^3\boldsymbol{r}' |\phi(\boldsymbol{r} - \boldsymbol{R}_{ub})|^2 v(|\boldsymbol{r} - \boldsymbol{r}'|) |\phi(\boldsymbol{r}' - \boldsymbol{R}_{u'b'})|^2. \quad (2.26)$$

The last overlap integral is only dependent on the spatial separation vector of the orbitals

$$I(\boldsymbol{R}_{u'b'} - \boldsymbol{R}_{ub}) = \int \mathrm{d}^3\boldsymbol{r}\, \mathrm{d}^3\boldsymbol{r}' |\phi(\boldsymbol{r} - \boldsymbol{R}_{ub})|^2 v(|\boldsymbol{r} - \boldsymbol{r}'|) |\phi(\boldsymbol{r}' - \boldsymbol{R}_{u'b'})|^2, \quad (2.27)$$

and we have

$$\begin{aligned} V(\alpha_1 \boldsymbol{k}_1, \alpha_2 \boldsymbol{k}_2; \alpha_3 \boldsymbol{k}_3, \alpha_4 \boldsymbol{k}_4) =& \frac{1}{N_u^2} \sum_{b,b'} C^*_{\alpha_1 b}(\boldsymbol{k}_1) C_{\alpha_2 b}(\boldsymbol{k}_2) C_{\alpha_3 b'}(\boldsymbol{k}_3) C^*_{\alpha_4 b'}(\boldsymbol{k}_4) \\ & \times \sum_{u,u'} e^{i[(\boldsymbol{k}_2 - \boldsymbol{k}_1).\boldsymbol{R}_{ub} + (\boldsymbol{k}_3 - \boldsymbol{k}_4).\boldsymbol{R}_{u'b'}]} I(\boldsymbol{R}_{u'b'} - \boldsymbol{R}_{ub}) \\ =& \frac{1}{N_u^2} \sum_{b,b'} C^*_{\alpha_1 b}(\boldsymbol{k}_1) C_{\alpha_2 b}(\boldsymbol{k}_2) C_{\alpha_3 b'}(\boldsymbol{k}_3) C^*_{\alpha_4 b'}(\boldsymbol{k}_4) \\ & \times \sum_{u} e^{i(\boldsymbol{k}_2 - \boldsymbol{k}_1 + \boldsymbol{k}_3 - \boldsymbol{k}_4).\boldsymbol{R}_{ub}} \sum_{u'} e^{i(\boldsymbol{k}_3 - \boldsymbol{k}_4).(\boldsymbol{R}_{u'b'} - \boldsymbol{R}_{ub})} I(\boldsymbol{R}_{u'b'} - \boldsymbol{R}_{ub}). \end{aligned} \quad (2.28)$$

Replacing u' with $u'' = u' - u$ in the last expression gives us the following final relation

$$V(\alpha_1 \boldsymbol{k}_1, \alpha_2 \boldsymbol{k}_2; \alpha_3 \boldsymbol{k}_3, \alpha_4 \boldsymbol{k}_4) = \delta(\boldsymbol{k}_2 - \boldsymbol{k}_1, \boldsymbol{k}_4 - \boldsymbol{k}_3) \times \cdots \cdots \sum_{b,b'} C^*_{\alpha_1 b}(\boldsymbol{k}_1) C_{\alpha_2 b}(\boldsymbol{k}_2) C_{\alpha_3 b'}(\boldsymbol{k}_3) C^*_{\alpha_4 b'}(\boldsymbol{k}_4) v_{b,b'}(\boldsymbol{k}_3 - \boldsymbol{k}_4), \quad (2.29)$$

where

$$v_{b,b'}(\boldsymbol{q}) = \frac{1}{N_u} \sum_{u''} e^{i\boldsymbol{q}.(\boldsymbol{R}_{u''b'} - \boldsymbol{R}_{0b})} I(\boldsymbol{R}_{u''b'} - \boldsymbol{R}_{0b}). \quad (2.30)$$

Furthermore, we approximate the overlap integral of the p_z orbitals by the Ohno potential [28, 65]

$$I(\boldsymbol{R}_{u''b'} - \boldsymbol{R}_{0b}) = \frac{U}{\sqrt{\left(\frac{4\pi\epsilon_0}{e^2} U |\boldsymbol{R}_{u''b'} - \boldsymbol{R}_{0b}|\right)^2 + 1}}, \quad (2.31)$$

where U is the energy cost of placing two electrons on a single p_z orbital, which we take to be 11.3 eV [28, 65]. An important point in Eq. (2.29) is the appearance of a delta function which conserves momentum between interacting wavefunctions. As we will see later, this delta function will enable us to do our calculation in the center-of-mass coordinates.

In order to calculate $\epsilon(\boldsymbol{q},0)$, we first calculate the following overlap integral for TB wavefunctions

$$\begin{aligned}
&\int \mathrm{d}^3\boldsymbol{r}\psi^*_{\alpha\boldsymbol{k}}(\boldsymbol{r})e^{-i\boldsymbol{q}.\boldsymbol{r}}\psi_{\alpha'\boldsymbol{k}+\boldsymbol{q}}(\boldsymbol{r}) = \\
&\frac{1}{N_u}\sum_{b,b'}\sum_{u,u'} C^*_{\alpha b}(\boldsymbol{k})C_{\alpha' b'}(\boldsymbol{k}+\boldsymbol{q})e^{i[-\boldsymbol{k}.\boldsymbol{R}_{ub}+(\boldsymbol{k}+\boldsymbol{q}).\boldsymbol{R}_{u'b'}]}\int \mathrm{d}^3\boldsymbol{r}\phi(\boldsymbol{r}-\boldsymbol{R}_{ub})e^{-i\boldsymbol{q}.\boldsymbol{r}}\phi(\boldsymbol{r}-\boldsymbol{R}_{u'b'}) \\
&= \sum_{u,b,b'} C^*_{\alpha b}(\boldsymbol{k})C_{\alpha' b'}(\boldsymbol{k}+\boldsymbol{q})e^{i[-\boldsymbol{k}.\boldsymbol{R}_{ub}+(\boldsymbol{k}+\boldsymbol{q}).\boldsymbol{R}_{0b'}]}\int \mathrm{d}^3\boldsymbol{r}\phi(\boldsymbol{r}-\boldsymbol{R}_{ub})e^{-i\boldsymbol{q}.\boldsymbol{r}}\phi(\boldsymbol{r}-\boldsymbol{R}_{0b'}). \quad (2.32)
\end{aligned}$$

Next, we take the integral in the expression nonnegligible only when $u=0$ and $b=b'$ in which the result of the integral is unity, therefore we get

$$\int \mathrm{d}^3\boldsymbol{r}\psi^*_{\alpha\boldsymbol{k}}(\boldsymbol{r})e^{-i\boldsymbol{q}.\boldsymbol{r}}\psi_{\alpha'\boldsymbol{k}+\boldsymbol{q}}(\boldsymbol{r}) \approx \sum_b C^*_{\alpha b}(\boldsymbol{k})C_{\alpha' b}(\boldsymbol{k}+\boldsymbol{q}). \quad (2.33)$$

Using the above expression and the zero-temperature occupation numbers, we get the following expression for polarization

$$\Pi(\boldsymbol{q}) = 2\sum_{\boldsymbol{k}}\left[\frac{\left|\sum_b C^*_{vb}(\boldsymbol{k})C_{cb}(\boldsymbol{k}+\boldsymbol{q})\right|^2}{\mathcal{E}_c(\boldsymbol{k}+\boldsymbol{q})-\mathcal{E}_v(\boldsymbol{k})} + \frac{\left|\sum_b C^*_{cb}(\boldsymbol{k})C_{vb}(\boldsymbol{k}+\boldsymbol{q})\right|^2}{\mathcal{E}_c(\boldsymbol{k})-\mathcal{E}_v(\boldsymbol{k}+\boldsymbol{q})}\right]. \quad (2.34)$$

The Fourier transform of the bare Coulomb interaction is

$$v(\boldsymbol{q}) = \frac{1}{4}\sum_{b,b'} v_{b,b'}(\boldsymbol{q}). \quad (2.35)$$

The final expression for the interaction kernels has the following format

$$\begin{aligned}
\mathcal{K}^d(\boldsymbol{k}_c,\boldsymbol{k}_v;\boldsymbol{k}'_c,\boldsymbol{k}'_v) =& \delta(\boldsymbol{k}_v-\boldsymbol{k}_c,\boldsymbol{k}'_v-\boldsymbol{k}'_c)\times\cdots \\
&\cdots\sum_{b,b'} C^*_{cb}(\boldsymbol{k}_c)C_{cb}(\boldsymbol{k}'_c)C_{vb'}(\boldsymbol{k}_v)C^*_{vb'}(\boldsymbol{k}'_v)\frac{v_{b,b'}(\boldsymbol{k}_c-\boldsymbol{k}'_c)}{\kappa\epsilon(\boldsymbol{k}_c-\boldsymbol{k}'_c)}, \quad (2.36a)
\end{aligned}$$

$$\mathcal{K}^x(\boldsymbol{k}_c,\boldsymbol{k}_v;\boldsymbol{k}'_c,\boldsymbol{k}'_v) =\delta(\boldsymbol{k}_v-\boldsymbol{k}_c,\boldsymbol{k}'_v-\boldsymbol{k}'_c)\times\cdots \\ \cdots\sum_{b,b'} C^*_{cb}(\boldsymbol{k}_c)C_{vb}(\boldsymbol{k}_v)C_{cb'}(\boldsymbol{k}'_c)C^*_{vb'}(\boldsymbol{k}'_v)v_{b,b'}(\boldsymbol{k}_c-\boldsymbol{k}_v). \tag{2.36b}$$

Now, we define the center-of-mass and relative motion wave vectors in the following manner

$$\boldsymbol{K}=\frac{\boldsymbol{k}_c-\boldsymbol{k}_v}{2}$$

and

$$\boldsymbol{k}_r=\frac{\boldsymbol{k}_c+\boldsymbol{k}_v}{2}.$$

The interaction kernels in terms of the new wave vectors will be

$$\mathcal{K}^d(\boldsymbol{k}_r,\boldsymbol{K};\boldsymbol{k}'_r,\boldsymbol{K}') =\delta(\boldsymbol{K},\boldsymbol{K}')\times\cdots \\ \cdots\sum_{b,b'} C^*_{cb}(\boldsymbol{k}_r+\boldsymbol{K})C_{cb}(\boldsymbol{k}'_r+\boldsymbol{K}')C_{vb'}(\boldsymbol{k}_r-\boldsymbol{K})C^*_{vb'}(\boldsymbol{k}'_r-\boldsymbol{K}')\frac{v_{b,b'}(\boldsymbol{k}_r-\boldsymbol{k}'_r)}{\kappa\epsilon(\boldsymbol{k}_r-\boldsymbol{k}'_r)}, \tag{2.37a}$$

$$\mathcal{K}^x(\boldsymbol{k}_r,\boldsymbol{K};\boldsymbol{k}'_r,\boldsymbol{K}') =\delta(\boldsymbol{K},\boldsymbol{K}')\times\cdots \\ \cdots\sum_{b,b'} C^*_{cb}(\boldsymbol{k}_r+\boldsymbol{K})C_{vb}(\boldsymbol{k}_r-\boldsymbol{K})C_{cb'}(\boldsymbol{k}'_r+\boldsymbol{K}')C^*_{vb'}(\boldsymbol{k}'_r-\boldsymbol{K}')v_{b,b'}(2\boldsymbol{K}). \tag{2.37b}$$

Therefore, we can reorganize the interaction kernel in such a way that it is block-diagonalized. These equations indicate that the center-of-mass wave vector is a good quantum number and the BS equation can be block-diagonalized in terms of this parameter. Therefore, we take $\boldsymbol{K}$ as a constant in the calculation of exciton energy and wavefunctions. Within the Tamm-Dancoff approximation, the excited-state wavefunction can now be written as

$$|s,\boldsymbol{K}\rangle=\sum_{\boldsymbol{k}_r} A_s(\boldsymbol{K},\boldsymbol{k}_r)\hat{u}^\dagger(\boldsymbol{k}_r+\boldsymbol{K})\hat{v}(\boldsymbol{k}_r-\boldsymbol{K})|\mathrm{GS}\rangle. \tag{2.38}$$

2.6 Application to single-wall carbon nanotubes

In this Section, we introduce some simplifications based on the specific physics of CNTs and show the calculation results for exciton energy dispersions for a (7,5) CNT.

First, we note that both the center-of-mass and relative-motion wave vectors in a CNT are two-dimensional vectors consisting of two components. (i) A discrete circumferential

part, which determines the electron and hole subband indices

$$\mathscr{M} = (\mu_c - \mu_v)/2 \quad , \quad \mu_r = (\mu_c + \mu_v)/2. \tag{2.39}$$

$\mathscr{M}$ determines the angular momentum of the exciton center of mass. (ii) A continuous part, parallel to the axis of the CNT, which determines how fast they are moving along the CNT

$$K = (k_c - k_v)/2 \quad , \quad k_r = (k_c + k_v)/2. \tag{2.40}$$

Now, as a further approximation, we take the off-diagonal elements of the kernel $\mathcal{K}$ to be small for the cutting lines that are energetically different. In practice, this means that we have to include $\boldsymbol{k}_r$ and $\boldsymbol{k}'_r$ that represent electronic transitions with almost similar energies.

As a result of the symmetry of the graphene Brillouin zone, there are two cutting lines with equal energies: one close to the K-point and another close to K'-point (Fig. 2.1). When a transition is made from the two highest valence subbands to the two lowest conduction subbands (S_{11}), if the electron and the hole are from the same cutting line, the exciton is A type, and if electron is from the cutting line near K-point and hole from the cutting line near K'-point (or vice versa) the excitation is E type (Figure 2.2).

By using the symmetry of graphene wavefunctions [Eq. (2.14)], we can show that, for an A-type exciton ($\mathscr{M} = 0$),

$$\mathcal{K}^d(\boldsymbol{k}_r, \boldsymbol{k}'_r; \boldsymbol{K}) = \mathcal{K}^d(-\boldsymbol{k}_r, -\boldsymbol{k}'_r; \boldsymbol{K}), \tag{2.41a}$$

$$\mathcal{K}^x(\boldsymbol{k}_r, \boldsymbol{k}'_r; \boldsymbol{K}) = \mathcal{K}^x(-\boldsymbol{k}_r, -\boldsymbol{k}'_r; \boldsymbol{K}), \tag{2.41b}$$

$$\mathcal{K}^x(\boldsymbol{k}_r, \boldsymbol{k}'_r; \boldsymbol{K}) = \mathcal{K}^x(\boldsymbol{k}_r, -\boldsymbol{k}'_r; \boldsymbol{K}), \tag{2.41c}$$

which results in symmetric (A_1) and antisymmetric (A_2) excitons [66]:

$$A_1 \text{ exciton} \rightarrow A_s(\boldsymbol{K}, \boldsymbol{k}_r) = -A_s(\boldsymbol{K}, -\boldsymbol{k}_r), \tag{2.42a}$$

$$A_2 \text{ exciton} \rightarrow A_s(\boldsymbol{K}, \boldsymbol{k}_r) = +A_s(\boldsymbol{K}, -\boldsymbol{k}_r). \tag{2.42b}$$

Figure 2.3 shows the energy dispersions for singlet ($\sigma = 0$) and triplet ($\sigma = 1$) excitons with various symmetries and center-of-mass momentum. Among the A-type excitons discussed

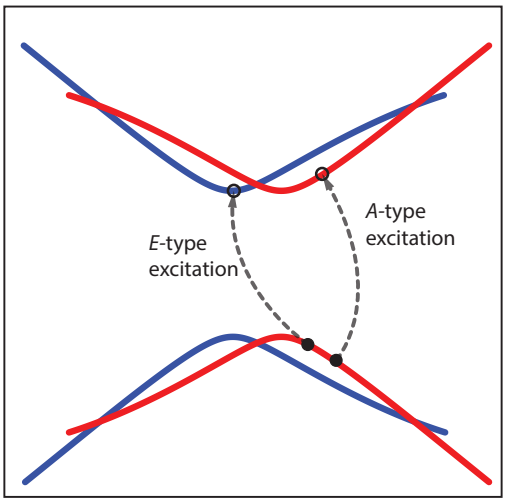

Figure 2.2: Schematic of excitation type based on the cutting lines of electron and hole. The dispersion curves in red (blue) color correspond to energy dispersions of cutting lines which pass by K (K') Dirac points in graphene Brillouin zone.

here, only the singlet A_2 exciton is bright and the rest are dark excitons [Fig. 2.3(b)]. We note that the center-of-mass of E-type excitons can have positive [blue curves in Fig. 2.3(d)–(e)] or negative [red curves in Fig. 2.3(d)–(e)] angular momenta.

Using the eigenvectors of the Bethe-Salpeter equation and the symmetry of excitonic states we can calculate the electron-hole amplitude [63], which is interpreted as the exciton wavefunction in the electron-hole picture:

$$\begin{aligned}\chi_{s,\boldsymbol{K}}(\boldsymbol{r},\boldsymbol{r'}) =& \frac{1}{\sqrt{2}}\sum_{\boldsymbol{k}_r} A_s(\boldsymbol{K},\boldsymbol{k}_r)\left(\psi_{c,\boldsymbol{k}_r+\boldsymbol{K}}(\boldsymbol{r})\psi^*_{v,\boldsymbol{k}_r-\boldsymbol{K}}(\boldsymbol{r'}) \pm \psi_{c,-\boldsymbol{k}_r+\boldsymbol{K}}(\boldsymbol{r})\psi^*_{v,-\boldsymbol{k}_r-\boldsymbol{K}}(\boldsymbol{r'})\right)\\ =& \frac{1}{N_u\sqrt{2}}\sum_{b,b'}\sum_{u,u'} e^{i\boldsymbol{K}.(\boldsymbol{R}_{ub}+\boldsymbol{R}_{u'b'})}\phi(\boldsymbol{r}-\boldsymbol{R}_{ub})\phi(\boldsymbol{r'}-\boldsymbol{R}_{u'b'})\times\\ &\sum_{\boldsymbol{k}_r} A_s(\boldsymbol{K},\boldsymbol{k}_r)\left(C_{cb}(\boldsymbol{k}_r+\boldsymbol{K})C^*_{vb'}(\boldsymbol{k}_r-\boldsymbol{K})e^{i\boldsymbol{k}_r.(\boldsymbol{R}_{ub}-\boldsymbol{R}_{u'b'})}\pm\right.\\ &\left. C_{cb}(-\boldsymbol{k}_r+\boldsymbol{K})C^*_{vb'}(-\boldsymbol{k}_r-\boldsymbol{K})e^{-i\boldsymbol{k}_r.(\boldsymbol{R}_{ub}-\boldsymbol{R}_{u'b'})}\right).\end{aligned} \tag{2.43}$$

Here, negative sign represents the symmetric excitonic states and the positive sign represents the antisymmetric excitonic states. Furthermore, $|\chi_{s,\boldsymbol{K}}(\boldsymbol{r},\boldsymbol{r'})|^2$ is the probability distribution function of find electron and the hole at coordinates $\boldsymbol{r}$ and $\boldsymbol{r'}$, respectively. Figure 2.4 shows this probability for finding the hole in the excitonic states at the bottom of ($\boldsymbol{K}=0$) lowest first ($s=1$) and second ($s=2$) in (7,5) CNT. We have assume that the electron is fixed in the position of one of the carbon atoms. As we can see, the probability in the first excited state is highest around the electron position and decays exponentialy as we move away. This is reminiscent of the S orbital in hydrogen atom. Likewise, the second excited state is reminiscent of the P orbital is hydrogen atom by having a node for the probability around the center.

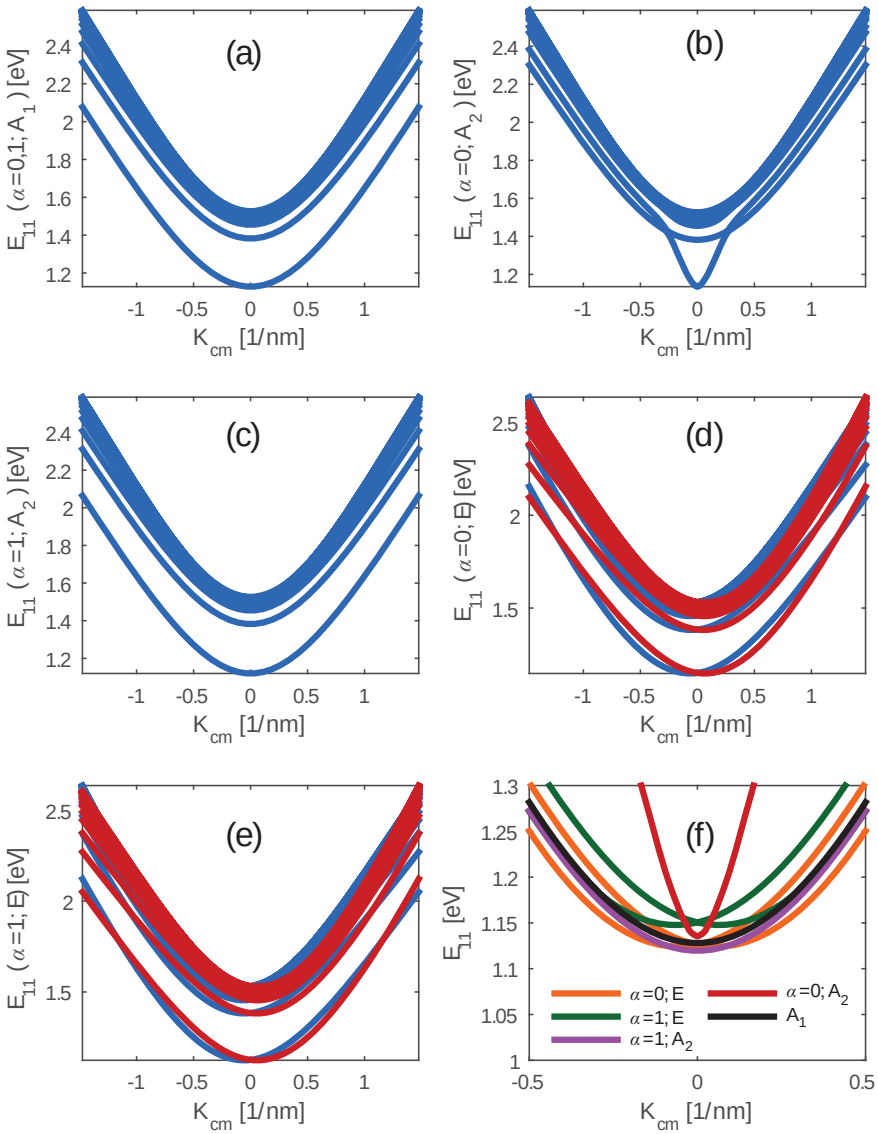

Figure 2.3: Energy dispersion of (a) A_1 singlet and triplet exciton, (b) A_2 singlet, (c) A_2 triplet exciton, (d) E type singlet excitons with positive (blue) and negative (red) circumferential momentum, and (e) E type triplet excitons with positive (blue) and negative (red) circumferential momentum for S_{11} transition in (7,5) carbon nanotube. Panel (f) shows a comparison of lowest-subband exciton dispersions for various exciton types.

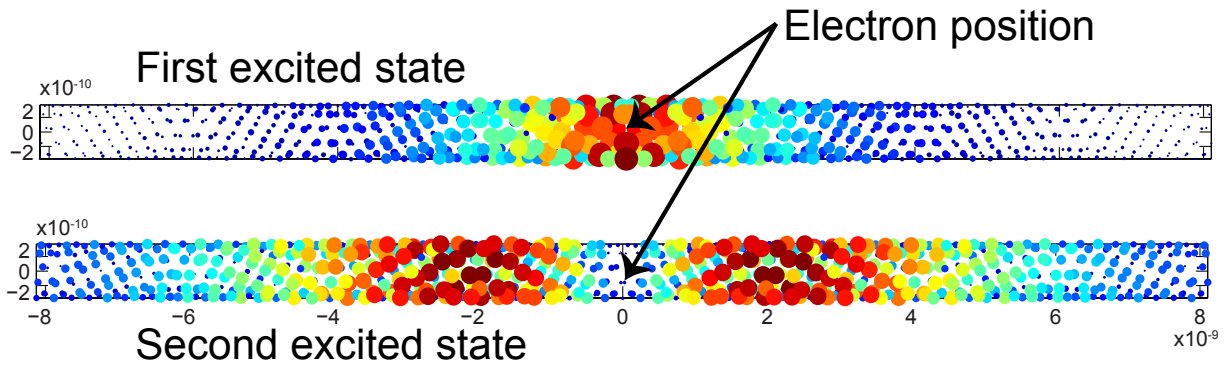

Figure 2.4: Probability of finding a hole in carbon sites inside a (7,5) CNT when assuming the electron is fixed on a carbon atom at the center. The top figure is the first excited state and the bottom figure is the second excited state.

Chapter 3

Resonant Exciton Transfer

In this Chapter, we review the underlying theory of resonant exciton transfer (RET) between two electronic systems. Then, we apply the theory to the excitonic states in CNTs. We derive expressions for the RET rate in CNTs with finite and infinite length. We discuss the dependence of the RET rate on the CNT length. The rest of the Chapter is devoted to the calculating the RET rate between CNTs with various chiralities and various lengths. We discuss effects of parameters such as tube orientation, exciton types, confinement length, and temperature on the RET rate.

3.1 Theory of resonance exciton transfer

The second-quantization Hamiltonian of two electronic systems without any interaction is

$$\hat{H}^{(0)} = \hat{H}_1 + \hat{H}_2, \tag{3.1}$$

where $\hat{H}_n$ is the Hamiltonian of the n-th isolated system

$$\hat{H}_n = \sum_{r_n,s_n} \langle r_n | \frac{\hat{\boldsymbol{p}}^2}{2m} + V_n(\boldsymbol{x}) | s_n \rangle \hat{w}^\dagger_{r_n} \hat{w}_{s_n} + \frac{1}{2} \sum_{r_n,s_n,t_n,u_n} \frac{e^2}{4\pi\epsilon} \langle r_n s_n | \frac{1}{|\boldsymbol{x} - \boldsymbol{x}'|} | t_n u_n \rangle \hat{w}^\dagger_{r_n} \hat{w}^\dagger_{s_n} \hat{w}_{u_n} \hat{w}_{t_n}. \tag{3.2}$$

Here, r_n, s_n, t_n, u_n are indices for the quasiparticle wavefunctions localized around the n-th system. The summations run over all wave vectors and all the band indices. $\hat{w}_r$ and $\hat{w}^\dagger_r$ are the annihilation and creation operators for the quasiparticle state $|r\rangle$. $V_n(\boldsymbol{x})$ is the potential due to the background atoms and external field in the n-th system, respectively.

However, electrons and atoms in the two systems interact via the Coulomb force and the total Hamiltonian of the two interacting systems is

$$\hat{H} = \hat{H}^{(0)} + \hat{H}^{(1)}, \tag{3.3}$$

where $\hat{H}^{(1)}$ is the interaction Hamiltonian between the two systems

$$\begin{aligned}\hat{H}^{(1)} =& \sum_{r_1,s_1} \langle r_1|V_2(\boldsymbol{x})|s_1\rangle \hat{w}^\dagger_{r_1}\hat{w}_{s_1} + \sum_{r_2,s_2} \langle r_2|V_1(\boldsymbol{x})|s_2\rangle \hat{w}^\dagger_{r_2}\hat{w}_{s_2} \\ &+ \frac{1}{2}\sum_{r_1,s_1,t_1}\sum_{u_2} \frac{e^2}{4\pi\epsilon}\langle r_1 s_1|\frac{1}{|\boldsymbol{x}-\boldsymbol{x}'|}|t_1 u_2\rangle \hat{w}^\dagger_{r_1}\hat{w}^\dagger_{s_1}\hat{w}_{u_2}\hat{w}_{t_1} \\ &+ \begin{pmatrix}\text{other permutations of choosing functions} \\ r,\ s,\ t,\text{ and } u \text{ from system \#1 or \#2}\end{pmatrix}.\end{aligned} \tag{3.4}$$

If the interaction between the two systems is weak enough[1] we can treat it as a perturbation to the Hamiltonian $\hat{H}^{(0)}$. Therefore, the resonant exciton transfer (RET) rate is calculated using first-order Fermi's Golden Rule

$$S(i \to f) = \frac{2\pi}{\hbar}\left|\langle i|\hat{H}^{(1)}|f\rangle\right|^2 \delta(E_i - E_f), \tag{3.5}$$

where, in the initial state, system 1 is excited and system 2 is in the ground state

$$|i\rangle = |1^*\rangle \otimes |2\rangle = \sum_{k_1,l_1} A(k_1,l_1)\hat{u}^\dagger_{k_1}\hat{v}_{l_1}|\mathrm{GS}\rangle, \tag{3.6}$$

and, in the final, state system 1 is in the ground state and system 2 is excited

$$|f\rangle = |1\rangle \otimes |2^*\rangle = \sum_{k_2,l_2} A(k_2,l_2)\hat{u}^\dagger_{k_2}\hat{v}_{l_2}|\mathrm{GS}\rangle. \tag{3.7}$$

Here, k_n and l_n are the quantum numbers corresponding to the quasiparticle states in conduction band and valence band in the n-th system, respectively. Also, $\hat{u}^\dagger_{k_n}$ and $\hat{v}_{l_n}$ are the creation and annihilation operators in the conduction and valence bands, respectively. $A(k_n,l_n)$ is the expansion coefficient of the excited state that is calculated by solving the

[1]For example because of the spatial distance between the two systems.

Bethe-Salpeter equation (see Sec. 2.5). $|\mathrm{GS}\rangle$ is the state where electrons in both systems are in the valence band, $|\mathrm{GS}\rangle = |\mathrm{GS}\rangle_1 \otimes |\mathrm{GS}\rangle_2$.

The first two expressions in the perturbation Hamiltonian, $\hat{H}^{(1)}$, refers to the interaction between electrons of one system and the atoms of the other system. These two expressions do not contribute to exciton transfer (ET) because they only perturb the electrons of one of the systems, as can be shown easily by forming the matrix element between the two states $|i\rangle$ and $|f\rangle$ and looking at the number of creation and annihilation operators corresponding to each electronic system.

The rest of the expressions in the perturbation Hamiltonian correspond to the interactions between electrons of the two systems that contribute to the ET process. We form the matrix elements between $|i\rangle$ and $|f\rangle$ by arbitrarily choosing wavefunctions r, s, t, and u from the first or second systems

$$M = \frac{e^2}{8\pi\epsilon} \sum_{k_1,l_1} \sum_{k_2,l_2} \sum_{r,s,t,u} A^*(k_1,l_1)A(k_2,l_2)\langle rs|\frac{1}{|\boldsymbol{x}-\boldsymbol{x}'|}|tu\rangle\langle \mathrm{GS}|\hat{v}^\dagger_{l_1}\hat{u}_{k_1}(\hat{w}^\dagger_r\hat{w}^\dagger_s\hat{w}_u\hat{w}_t)\hat{u}^\dagger_{k_2}\hat{v}_{l_2}|\mathrm{GS}\rangle. \tag{3.8}$$

Based on the number of creation and annihilation operators in the conduction and valence bands of each system, we conclude that the matrix element is nonzero only for the following cases

$$\begin{pmatrix} \hat{w}_r = \hat{u}_{k_1} \\ \hat{w}_s = \hat{v}_{l_2} \\ \hat{w}_u = \hat{u}_{k_2} \\ \hat{w}_t = \hat{v}_{l_1} \end{pmatrix} \text{ or } \begin{pmatrix} \hat{w}_r = \hat{v}_{l_2} \\ \hat{w}_s = \hat{u}_{k_1} \\ \hat{w}_u = \hat{v}_{l_1} \\ \hat{w}_t = \hat{u}_{k_2} \end{pmatrix} \text{ or } \begin{pmatrix} \hat{w}_r = \hat{u}_{k_1} \\ \hat{w}_s = \hat{v}_{l_2} \\ \hat{w}_u = \hat{u}_{l_1} \\ \hat{w}_t = \hat{v}_{k_2} \end{pmatrix} \text{ or } \begin{pmatrix} \hat{w}_r = \hat{v}_{l_2} \\ \hat{w}_s = \hat{u}_{k_1} \\ \hat{w}_u = \hat{v}_{k_2} \\ \hat{w}_t = \hat{u}_{l_1} \end{pmatrix}. \tag{3.9}$$

The matrix elements of the first two cases are practically the same and correspond to ET due to direct Coulomb interaction between electrons [see Fig. 1.4(a)]. The matrix elements of the last two cases are also practically the same and correspond to ET via exchange Coulomb interaction [see Fig. 1.4(b)]. The second-quantization matrix element, $\langle \mathrm{GS}|\hat{v}^\dagger_{l_1}\hat{u}_{k_1}(\hat{w}^\dagger_r\hat{w}^\dagger_s\hat{w}_u\hat{w}_t)\hat{u}^\dagger_{k_2}\hat{v}_{l_2}|\mathrm{GS}\rangle$, is $+1$ for direct processes and -1 for exchange processes.

The remaining task is to calculate the matrix element of the Coulomb interaction between quasiparticle wavefunctions. The Coulomb interaction matrix elements corresponding to the

exchange ET process depends on the overlap of the quasiparticle wavefunctions,

$$\int d\boldsymbol{r}\psi^*_{k_1}(\boldsymbol{r})\psi_{l_2}(\boldsymbol{r}), \tag{3.10}$$

across the two systems, which tends to be negligible if the systems are far from each other. However, the Coulomb matrix element for the direct ET process can be considered as the Coulomb interaction between transition charge densities,

$$q_{\rm tr}(\boldsymbol{r}) = \psi^*_k(\boldsymbol{r})\psi_l(\boldsymbol{r}), \tag{3.11}$$

across the two system, which is a long range effect. It can be shown that, when the size of each individual system is much smaller than the spatial separation of the donor and acceptor systems, the direct interaction matrix element can be approximated as a dipole–dipole interaction between the transition charges in the two systems; this is known as Förster exciton transfer [49]. However, for large polymers and the CNTs with a separation of only a couple of nanometers, this approximation fails to produce accurate ET rates and we should use a more comprehensive method for the calculation of the direct-interaction matrix element [67, 59].

3.2 Direct-interaction matrix element in CNTs

In this Section, we calculate the matrix element of the Coulomb interaction between two CNTs beyond the transition-dipole approximation. Figure 3.1 shows the geometry of the donor and acceptor CNTs with respect to each other. Here, we calculate the direct interaction matrix element in Eq. (3.8) between single excitation states in the donor CNT, $|s_1, \boldsymbol{K}_1\rangle$, and in the acceptor CNT, $|s_2, \boldsymbol{K}_2\rangle$. A single excitation states means that there is one exciton in one of the CNTs and the other CNT is in the ground state. The direct

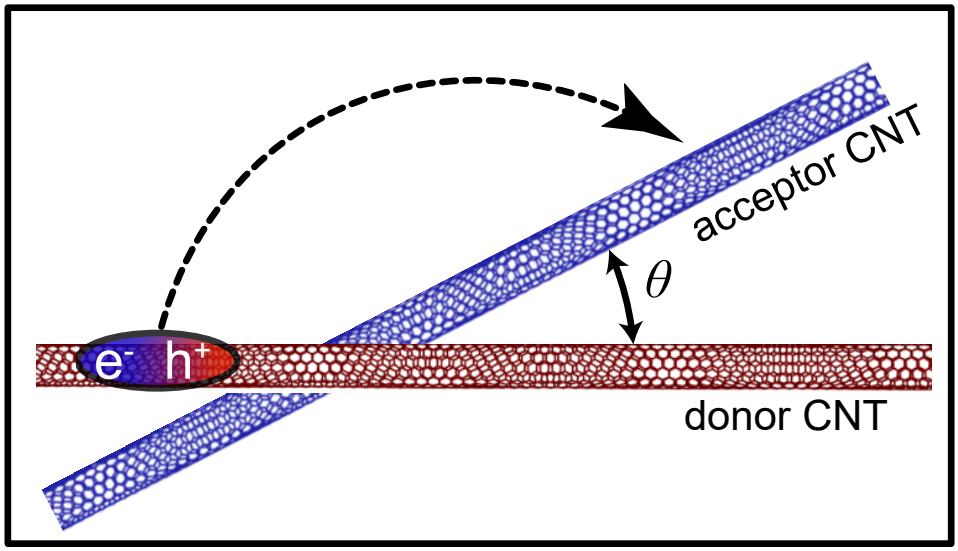

Figure 3.1: Geometry of donor (red) and acceptor (blue) carbon nanotubes.

interaction matrix element is

$$\begin{aligned} M_d =& \langle s_1, \boldsymbol{K}_1 | \hat{H}_d^{(1)} | s_2, \boldsymbol{K}_2 \rangle \\ =& 2 \times \frac{1}{2} \sum_{\boldsymbol{k}_{r_1}} \sum_{\boldsymbol{k}_{r_2}} A^*_{s_1}(\boldsymbol{K}_1, \boldsymbol{k}_{r_1}) A_{s_2}(\boldsymbol{K}_2, \boldsymbol{k}_{r_2}) \langle \boldsymbol{k}_{v_2}, \boldsymbol{k}_{c_1} | v(\boldsymbol{r} - \boldsymbol{r}') | \boldsymbol{k}_{c_2}, \boldsymbol{k}_{v_1} \rangle \\ =& \sum_{\boldsymbol{k}_{r_1}} \sum_{\boldsymbol{k}_{r_2}} A^*_{s_1}(\boldsymbol{K}_1, \boldsymbol{k}_{r_1}) A_{s_2}(\boldsymbol{K}_2, \boldsymbol{k}_{r_2}) \times V(c, \boldsymbol{k}_{c_1}, v, \boldsymbol{k}_{v_1}; c, \boldsymbol{k}_{c_2}, v, \boldsymbol{k}_{v_2}). \end{aligned} \tag{3.12}$$

In the last equation, the factor of 2 stands for the two permutations of choosing the quasi-particle states in direct ET process. The factor of $\frac{1}{2}$ is to avoid double counting of electron pairs in the second-quantization formalism [see Eq. (3.4)]. We also have

$$\begin{aligned} \boldsymbol{k}_{c_1} &= \boldsymbol{k}_{r_1} + \boldsymbol{K}_1 \quad , \quad \boldsymbol{k}_{v_1} = \boldsymbol{k}_{r_1} - \boldsymbol{K}_1, \\ \boldsymbol{k}_{c_2} &= \boldsymbol{k}_{r_2} + \boldsymbol{K}_2 \quad , \quad \boldsymbol{k}_{v_2} = \boldsymbol{k}_{r_2} - \boldsymbol{K}_2. \end{aligned} \tag{3.13}$$

Next, we calculate the overlap integral, V, by using the tight-binding wavefunctions

$$\psi_{\alpha \boldsymbol{k}}(\boldsymbol{r}) = \frac{1}{\sqrt{N_u}} \sum_b \sum_u C_{\alpha b}(\boldsymbol{k}) e^{i \boldsymbol{k} . \boldsymbol{R}_{ub}} \phi(\boldsymbol{r} - \boldsymbol{R}_{ub}). \tag{3.14}$$

Here, u runs over all the graphene unit cells in the donor or the acceptor system with the total number of N_u. b runs over the atoms in graphene unit cell. Wave vector $\boldsymbol{k}$ includes both

the continuous one-dimensional wave vector along the tube axis (k) as well as the discrete circumferential wave vector (given by its integer proxy μ). The index α shows the conduction or the valence band in CNT. Therefore, the overlap integral is

$$\begin{aligned}
V(c,\boldsymbol{k}_{c_1},v,\boldsymbol{k}_{v_2};c,\boldsymbol{k}_{c_2},v,\boldsymbol{k}_{v_2}) &= \int d^3\boldsymbol{r}\ d^3\boldsymbol{r}'\psi^*_{c\boldsymbol{k}_{c_1}}(\boldsymbol{r})\psi_{v\boldsymbol{k}_{v_1}}(\boldsymbol{r})v(|\boldsymbol{r}-\boldsymbol{r}'|)\psi_{c\boldsymbol{k}_{c_2}}(\boldsymbol{r}')\psi^*_{v\boldsymbol{k}_{v_2}}(\boldsymbol{r}') \\
&= \frac{1}{N_{u_1}N_{u_2}}\sum_{b_1,b_2}\sum_{b_3,b_4} C^*_{cb_1}(\boldsymbol{k}_{c_1})C_{vb_2}(\boldsymbol{k}_{v_1})C_{cb_3}(\boldsymbol{k}_{c_2})C^*_{vb_4}(\boldsymbol{k}_{v_2})\times\cdots \\
&\quad \cdots\sum_{u_1,u_2}\sum_{u_3,u_4} e^{i(-\boldsymbol{k}_{c_1}.\boldsymbol{R}_{u_1b_1}+\boldsymbol{k}_{v_1}.\boldsymbol{R}_{u_2b_2}+\boldsymbol{k}_{c_2}.\boldsymbol{R}_{u_3b_3}-\boldsymbol{k}_{v_2}.\boldsymbol{R}_{u_4b_4})}\times\cdots \\
&\quad \cdots\int d^3\boldsymbol{r}\ d^3\boldsymbol{r}'\phi(\boldsymbol{r}-\boldsymbol{R}_{u_1b_1})\phi(\boldsymbol{r}-\boldsymbol{R}_{u_2b_2})v(|\boldsymbol{r}-\boldsymbol{r}'|)\phi(\boldsymbol{r}'-\boldsymbol{R}_{u_3b_3})\phi(\boldsymbol{r}'-\boldsymbol{R}_{u_4b_4}).
\end{aligned} \tag{3.15}$$

Now, we assume the last integral is non-negligible only when $u_1b_1 = u_2b_2 = ub$ and $u_3b_3 = u_4b_4 = u'b'$, then the overlap integral becomes

$$\begin{aligned}
&V(c,\boldsymbol{k}_{c_1},v,\boldsymbol{k}_{v_2};c,\boldsymbol{k}_{c_2},v,\boldsymbol{k}_{v_2}) = \\
&\quad\frac{1}{N_{u_1}N_{u_2}}\sum_{b,b'} C^*_{cb}(\boldsymbol{k}_{c_1})C_{vb}(\boldsymbol{k}_{v_1})C_{cb'}(\boldsymbol{k}_{c_2})C^*_{vb'}(\boldsymbol{k}_{v_2})\sum_{u,u'} e^{i\left[(\boldsymbol{k}_{v_1}-\boldsymbol{k}_{c_1}).\boldsymbol{R}_{ub}+(\boldsymbol{k}_{c_2}-\boldsymbol{k}_{v_2}).\boldsymbol{R}_{u'b'}\right]} \\
&\qquad\qquad\times\int \mathrm{d}^3\boldsymbol{r}\,\mathrm{d}^3\boldsymbol{r}'|\phi(\boldsymbol{r}-\boldsymbol{R}_{ub})|^2 v(|\boldsymbol{r}-\boldsymbol{r}'|)|\phi(\boldsymbol{r}'-\boldsymbol{R}_{u'b'})|^2.
\end{aligned} \tag{3.16}$$

Considering the relatively small size of the atomic orbitals with respect to the separation of the atoms in the two system, we can use the transition monopole approximation (TMA) [68, 59]:

$$\begin{aligned}
I(\boldsymbol{R}_{u'b'}-\boldsymbol{R}_{ub}) &= \int \mathrm{d}^3\boldsymbol{r}\,\mathrm{d}^3\boldsymbol{r}'|\phi(\boldsymbol{r}-\boldsymbol{R}_{ub})|^2 v(|\boldsymbol{r}-\boldsymbol{r}'|)|\phi(\boldsymbol{r}'-\boldsymbol{R}_{u'b'})|^2 \\
&\approx \int d^3\boldsymbol{r}\ d^3\boldsymbol{r}'|\phi(\boldsymbol{r}-\boldsymbol{R}_{ub})|^2 v(|\boldsymbol{R}_{ub}-\boldsymbol{R}_{u'b'}|)|\phi(\boldsymbol{r}'-\boldsymbol{R}_{u'b'})|^2 \\
&= v(|\boldsymbol{R}_{ub}-\boldsymbol{R}_{u'b'}|) \\
&= \frac{e^2}{4\pi\epsilon|\boldsymbol{R}_{ub}-\boldsymbol{R}_{u'b'}|}.
\end{aligned} \tag{3.17}$$

Therefore, we have

$$V(c,\boldsymbol{k}_{c_1},v,\boldsymbol{k}_{v_1};c,\boldsymbol{k}_{c_2},v,\boldsymbol{k}_{v_2}) = \frac{e^2}{4\pi\epsilon N_{u_1}N_{u_2}}\sum_{b,b'} C^*_{cb}(\boldsymbol{k}_{c_1})C_{vb}(\boldsymbol{k}_{v_1})C_{cb'}(\boldsymbol{k}_{c_2})C^*_{vb'}(\boldsymbol{k}_{v_2})\sum_{u,u'} e^{i(-2\boldsymbol{K}_1.\boldsymbol{R}_{ub}+2\boldsymbol{K}_2.\boldsymbol{R}_{u'b'})}\frac{1}{|\boldsymbol{R}_{ub}-\boldsymbol{R}_{u'b'}|}. \tag{3.18}$$

Taking the wall-to-wall separation between the tubes to be large enough that the relative position of atoms in donor and acceptor CNTs are not important in calculating the ET rate, we have

$$\frac{1}{|\boldsymbol{R}_{ub}-\boldsymbol{R}_{u'b'}|} \approx \frac{1}{|\boldsymbol{R}_{u}-\boldsymbol{R}_{u'}|}, \tag{3.19}$$

where we have $\boldsymbol{R}_{ub} = \boldsymbol{R}_u + \boldsymbol{d}_b$. Therefore, the overlap integral is

$$V(c,\boldsymbol{k}_{c_1},v,\boldsymbol{k}_{v_1};c,\boldsymbol{k}_{c_2},v,\boldsymbol{k}_{v_2}) = \frac{1}{4\pi\epsilon N_{u_1}N_{u_2}}\left(\sum_{b,b'} C^*_{cb}(\boldsymbol{k}_{c_1})C_{vb}(\boldsymbol{k}_{v_1})C_{cb'}(\boldsymbol{k}_{c_2})C^*_{vb'}(\boldsymbol{k}_{v_2})e^{i(-2\boldsymbol{K}_1.\boldsymbol{d}_b+2\boldsymbol{K}_2.\boldsymbol{d}_{b'})}\right) \times \left(\sum_{u,u'} e^{i(-2\boldsymbol{K}_1.\boldsymbol{R}_u+2\boldsymbol{K}_2.\boldsymbol{R}_{u'})}\frac{1}{|\boldsymbol{R}_u-\boldsymbol{R}_{u'}|}\right). \tag{3.20}$$

3.2.1 Finite-length CNTs

We call the last sum in Eq. (3.20) the geometric part of the matrix element

$$J_\theta(\boldsymbol{K}_1,\boldsymbol{K}_2) = \sum_{u,u'} e^{i(-2\boldsymbol{K}_1.\boldsymbol{R}_u+2\boldsymbol{K}_2.\boldsymbol{R}_{u'})}\frac{1}{|\boldsymbol{R}_u-\boldsymbol{R}_{u'}|}. \tag{3.21}$$

Therefore, the matrix element is

$$M_d = \frac{e^2}{4\pi\epsilon N_{u_1}N_{u_2}}J_\theta(\boldsymbol{K}_1,\boldsymbol{K}_2)\sum_{\boldsymbol{k}_{r_1}}\sum_{\boldsymbol{k}_{r_2}} A^*_{s_1}(\boldsymbol{K}_1,\boldsymbol{k}_{r_1})A_{s_2}(\boldsymbol{K}_2,\boldsymbol{k}_{r_2}) \times \sum_{b,b'} C^*_{cb}(\boldsymbol{k}_{c_1})C_{vb}(\boldsymbol{k}_{v_1})C_{cb'}(\boldsymbol{k}_{c_2})C^*_{vb'}(\boldsymbol{k}_{v_2})e^{i(-2\boldsymbol{K}_1.\boldsymbol{d}_b+2\boldsymbol{K}_2.\boldsymbol{d}_{b'})}. \tag{3.22}$$

In order to use the calculated matrix element in Fermi's Golden Rule, it is better to write this equations in terms of the CNT length, which is a continous quantity. Therefore, we use

the following relations,

$$N_{u_1} = \frac{2\pi r_1 L_1}{A_u} \quad , \quad N_{u_2} = \frac{2\pi r_2 L_2}{A_u}, \tag{3.23}$$

where A_u is the area of graphene unit cell, and r_n is the radius of the n-th CNT. Therefore, we get

$$M_d = \frac{e^2 A_u^2}{16\pi^3 \epsilon\, r_1 r_2 L_1 L_2} J_\theta(\boldsymbol{K}_1, \boldsymbol{K}_2) \sum_{\boldsymbol{k}_{r_1}} \sum_{\boldsymbol{k}_{r_2}} A^*_{s_1}(\boldsymbol{K}_1, \boldsymbol{k}_{r_1}) A_{s_2}(\boldsymbol{K}_2, \boldsymbol{k}_{r_2}) \\ \times \sum_{b,b'} C^*_{cb}(\boldsymbol{k}_{c_1}) C_{vb}(\boldsymbol{k}_{v_1}) C_{cb'}(\boldsymbol{k}_{c_2}) C^*_{vb'}(\boldsymbol{k}_{v_2}) e^{i(-2\boldsymbol{K}_1.\boldsymbol{d}_b + 2\boldsymbol{K}_2.\boldsymbol{d}_{b'})}. \tag{3.24}$$

Note that, based on the normalization of the exciton wavefunction, we have $A_s(\boldsymbol{K}, \boldsymbol{k}_r) \propto \frac{1}{\sqrt{L}}$, whereas the number of terms in the summation over $\boldsymbol{k}_r$ increases linearly with L (see Appendix A for more details). Therefore, in order to extract the size dependence of the matrix element, we introduce a size-independent k-space part of the matrix element,

$$Q(\boldsymbol{K}_1, \boldsymbol{K}_2) = \frac{e^2 A_u^2}{16\pi^3 \epsilon\, r_1 r_2 \sqrt{L_1 L_2}} \sum_{\boldsymbol{k}_{r_1}} \sum_{\boldsymbol{k}_{r_2}} A^*_{s_1}(\boldsymbol{K}_1, \boldsymbol{k}_{r_1}) A_{s_2}(\boldsymbol{K}_2, \boldsymbol{k}_{r_2}) \\ \times \sum_{b,b'} C^*_{cb}(\boldsymbol{k}_{c_1}) C_{vb}(\boldsymbol{k}_{v_1}) C_{cb'}(\boldsymbol{k}_{c_2}) C^*_{vb'}(\boldsymbol{k}_{v_2}) e^{i(-2\boldsymbol{K}_1.\boldsymbol{d}_b + 2\boldsymbol{K}_2.\boldsymbol{d}_{b'})}. \tag{3.25}$$

Therefore, we have

$$M_d = \frac{1}{\sqrt{L_1 L_2}} J_\theta(\boldsymbol{K}_1, \boldsymbol{K}_2) \times Q(\boldsymbol{K}_1, \boldsymbol{K}_2). \tag{3.26}$$

Here, the matrix element is composed of two parts. The k-space part of the matrix element, $Q(\boldsymbol{K}_1, \boldsymbol{K}_2)$, is dependent on the details of the exciton wavefunction in isolated CNTs. We paid attention to make Q independent of the length and relative orientation of the CNTs (see Appendix A). However, the geometric part of the matrix element, $J_\theta(\boldsymbol{K}_1, \boldsymbol{K}_2)$, is very sensitive to the orientation and length of the CNTs. Therefore, in order to calculate the Coulomb-coupling matrix element for CNTs with a certain length, it is sufficient to calculate Q for long CNTs (which is easier for numerical reasons) and only calculate J_θ for the tubes with a specific finite length and mutual orientation.

Figure 3.2 shows J_θ for two pairs of CNTs. When the CNTs are parallel ($\theta = 0$) and the length of CNTs increases, the maximum of the J_θ increases without any upper limit

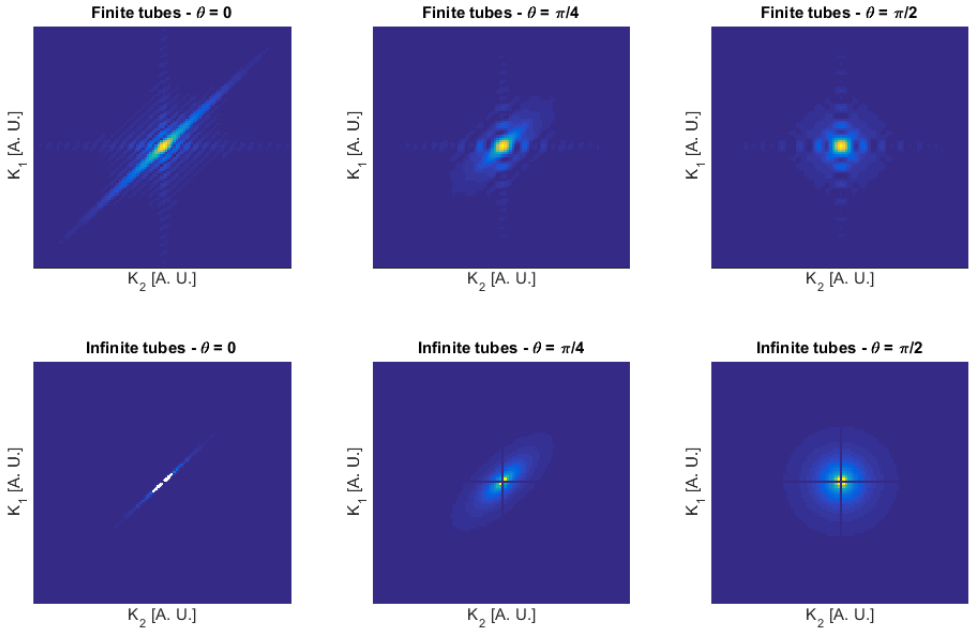

Figure 3.2: Geometric part of the matrix element (J_θ), presented by color (bright-high, dark-low), for short (top) and very long (bottom) pairs of CNTs as a function of the initial and final center-of-mass wave vectors. θ is the angle between the tube axes.

($J_\theta \to \infty$). However, when the CNTs are nonparallel, the geometric part of the matrix element is not very sensitive to the length of the CNTs. In order to better understand the effect of the CNT length on the ET rate, we derive the Coulomb matrix element for infinitely long CNTs in the following subsection.

3.2.2 Infinite-length CNTs

Let us assume that the CNTs are far enough that from the point of view of each CNT that the other one looks like a continuum and we can convert the last sum in Eq. (3.20) to an integral

$$\sum_{u,u'} e^{i(-2\boldsymbol{K}_1.\boldsymbol{R}_{ub}+2\boldsymbol{K}_2.\boldsymbol{R}_{u'b'})}\frac{1}{|\boldsymbol{R}_{ub}-\boldsymbol{R}_{u'b'}|} \approx \frac{1}{A_u^2}\times\int d^2\boldsymbol{r}\; d^2\boldsymbol{r}'\frac{e^{-2i\boldsymbol{K}_1.\boldsymbol{r}}\times e^{2i\boldsymbol{K}_2.\boldsymbol{r}'}}{|\boldsymbol{r}-\boldsymbol{r}'|}, \tag{3.27}$$

where the surface integrals are over CNT surfaces. A_u is the area of the primitive unit cell in graphene.

Assuming that the CNTs are shifted by center-to-center distance D along the z-axis and they are misoriented by angle θ in the x-y plane, the position vectors are

$$\boldsymbol{r} = (x, r_1\cos\phi, r_1\sin\phi), \tag{3.28a}$$

$$\boldsymbol{r}' = (x'\cos\theta - r_2\cos\phi'\sin\theta, x'\sin\theta + r_2\cos\phi'\cos\theta, D + r_2\sin\phi'). \tag{3.28b}$$

Therefore, the last integral would be

$$\begin{aligned} J_\theta(\boldsymbol{K}_1,\boldsymbol{K}_2) = \\ \frac{r_1 r_2}{A_u^2}\int dx\; dx'\; d\phi\; d\phi'\; e^{-2i(K_1 x+\mathscr{M}_1\phi)+2i(K_2 x'+\mathscr{M}_2\phi')}\Big((x'\cos\theta - r_2\cos\phi'\sin\theta - x)^2+\cdots \\ \cdots(x'\sin\theta + r_2\cos\phi'\cos\theta - r_1\cos\phi)^2 + (D + r_2\sin\phi' - r_1\sin\phi)^2\Big)^{-\frac{1}{2}}, \end{aligned} \tag{3.29}$$

where r_1 and r_2 are the diameters of the donor and acceptor CNTs, respectively. For infinitely long pairs of CNTs, the integrals over x and x' in the geometric part of the matrix element

can be calculated analytically (see Appendix B):

$$J_\theta(\boldsymbol{K}_1,\boldsymbol{K}_2)=\frac{\pi r_1 r_2}{{A_u}^2}\int d\phi\, d\phi'\,\exp\big(2i(\mathscr{M}_2\phi'-\mathscr{M}_1\phi)\big)$$
$$\times\exp\left(2i\frac{K_1(r_2\cos\phi'-r_1\cos\phi\cos\theta)+K_2(r_1\cos\phi-r_2\cos\phi'\cos\theta)}{\sin\theta}\right)$$
$$\times\frac{\exp(-2\frac{|D+r_2\sin\phi'-r_1\sin\phi|}{\sin\theta}\sqrt{K_2^2+K_1^2-2K_1K_2\cos\theta})}{\sqrt{K_2^2+K_1^2-2K_1K_2\cos\theta}}. \quad (3.30)$$

When CNTs are nonparallel ($\theta\neq 0$), this expression is finite and nonzero, which means that ET is possible between excitonic states with arbitrary center-of-mass momentum. However, when the CNTs are parallel ($\theta=0$), the geometric part of the matrix element is divergent when $K_1=K_2$ and zero everywhere else. This means that the center-of-mass momentum needs to be conserved in the ET process between parallel CNTs.

Furthermore, since Eq. (3.30) is divergent in this case, we need to first take the limits of $\theta\to 0$ and $K_1\to K_2$ before taking the limits of $L_1\to\infty$ and $L_2\to\infty$. By performing this calculation, we arrive at the following expression for the geometric part of the matrix element

$$J_0(\boldsymbol{K}_1,\boldsymbol{K}_2)=L\times\delta_{K_1,K_2}\times C(\mathscr{M}_1,\mathscr{M}_2;K_1), \quad (3.31)$$

$$C(\mathscr{M}_1,\mathscr{M}_2;K_1)=\frac{2r_1r_2}{A_u^2}\int d\phi\, d\phi'\, e^{2i(\mathscr{M}_2\phi'-\mathscr{M}_1\phi)}\times\cdots$$
$$\cdots\mathcal{K}_0(|2K_1|\sqrt{(r_1\sin\phi-r_2\sin\phi')^2+(D+r_1\cos\phi-r_2\cos\phi')^2}), \quad (3.32)$$

where we have $L_1=L_2=L\to\infty$ and $\mathcal{K}_0$ is the modified Bessel function of the second kind. δ_{K_1,K_2} is the Dirac delta function, which enforces the center-of-mass momentum conservation in the ET process.

3.3 Resonant exciton-transfer rate in CNTs

The RET rate between single-exciton states is given by first-order Fermi's Golden Rule

$$S(s_1,\boldsymbol{K}_1;s_2,\boldsymbol{K}_2)=\frac{2\pi}{\hbar}|M_d|^2\delta\big(\Omega_{s_1}(\boldsymbol{K}_1)-\Omega_{s_2}(\boldsymbol{K}_2)\big), \quad (3.33)$$

where $\Omega_{s_n}(\boldsymbol{K}_n)$ is the energy of exciton in the n-th CNT. Assuming that the excitons have thermal equilibrium distribution in the donor CNT, the effective RET rate is given by summing over all the final states (s_2 and $\boldsymbol{K}_2$) and averaging over all initial states (s_1 and $\boldsymbol{K}_1$)

$$\Gamma_{12} = \frac{2\pi}{\hbar} \sum_{s_1,s_2} \sum_{\boldsymbol{K}_1,\boldsymbol{K}_2} \frac{e^{-\beta\Omega_{s_1}}}{\mathcal{Z}} |M_d|^2 \delta(\Omega_{s_1} - \Omega_{s_2}). \tag{3.34}$$

Here, $\mathcal{Z} = \mathrm{tr}\{\exp(-\beta\hat{H}^{(0)})\}$ is the partition function

$$\mathcal{Z} = \mathrm{tr}\{e^{-\hat{H}^{(0)}/k_BT}\} = \sum_{s_1} \sum_{\boldsymbol{K}_1} e^{-\beta\Omega_{s_1}}. \tag{3.35}$$

Assuming the tubes are long enough that we can convert the summation over $\boldsymbol{K}_2$ into integration we get

$$\begin{aligned}
\Gamma_{12} =& \frac{2\pi}{\hbar} \frac{1}{\Delta K_2} \sum_{s_1,s_2} \sum_{\boldsymbol{K}_1} \sum_{\mathscr{M}_2} \int dK_2 \frac{e^{-\beta\Omega_{s_1}}}{\mathcal{Z}} |M_d|^2 \delta(\Omega_{s_1} - \Omega_{s_2}) \\
=& \frac{2\pi}{\hbar} \frac{1}{\Delta K_2} \sum_{s_1,s_2} \sum_{\boldsymbol{K}_1} \sum_{\mathscr{M}_2} \frac{e^{-\beta\Omega_{s_1}}}{\mathcal{Z}} |M_d|^2 \left(\frac{dK_2}{d\Omega_{s_2}}\right)_{\Omega_{s_1}} \\
=& \frac{2\pi}{\hbar} \frac{1}{L_1 L_2 \Delta K_2} \sum_{s_1,s_2} \sum_{\boldsymbol{K}_1} \sum_{\mathscr{M}_2} \frac{e^{-\beta\Omega_{s_1}}}{\mathcal{Z}} |J_\theta(\boldsymbol{K}_1, \boldsymbol{K}_2) \times Q(\boldsymbol{K}_1, \boldsymbol{K}_2)|^2 \left(\frac{dK_2}{d\Omega_{s_2}}\right)_{\Omega_{s_1}}.
\end{aligned} \tag{3.36}$$

Using the relation

$$\Delta K_2 = \frac{2\pi}{L_2}, \tag{3.37}$$

we get

$$\Gamma_{12} = \frac{1}{\hbar L_1} \sum_{s_1,s_2} \sum_{\boldsymbol{K}_1} \sum_{\mathscr{M}_2} \frac{e^{-\beta\Omega_{s_1}}}{\mathcal{Z}} |J_\theta(\boldsymbol{K}_1, \boldsymbol{K}_2) \times Q(\boldsymbol{K}_1, \boldsymbol{K}_2)|^2 \left(\frac{dK_2}{d\Omega_{s_2}}\right)_{\Omega_{s_1}}. \tag{3.38}$$

As we can see, there is an inverse dependence on the length of the donor CNT (L_1) which suggests that the RET rate would tend to zero when the CNT length increases. Therefore, it is nessecary to understand the dependence of the Coulomb matrix element ($J_\theta \times Q$) on the length of the CNTs. In Appendix A, we discuss that the k-space part of the matrix element, Q, does not have any length dependence. In contrast, the geometric part of the matrix element, J_θ, is dependent on the size of both CNTs. In Sec. 3.2.2, the showed that, in the case of parallel CNTs, the geometric part of the matrix element increases linearly

with length; however, in the case of nonparallel CNTs, J_θ has an upper limit. As a result of this behavior, the ET rate between nonparallel CNTs is inversely dependent on the donor CNT length. In a CNT film, the number of acceptor CNTs increases with the length of the donor CNT and the more relevant quantity is the normalized RET rate, $\tilde{\Gamma} = L \times \Gamma$, which is dependent on the density of the CNTs in the film.

As for the case of very long parallel CNTs, the RET has a much more complicated dependence on the length. We will derive the RET rates for this special case in the following section and discuss the dependence of the RET rates on the length of the CNTs in Sec. 3.4.2.

3.3.1 Special case of infinite parallel CNTs

When the CNTs are very long and parallel to each other the geometric part of the matrix element is given by Eq. (3.31). Therefore, the Coulomb-coupling matrix element is

$$M_d = \delta_{K_1,K_2} C(\mathscr{M}_1, \mathscr{M}_2; K_1) \times Q(\boldsymbol{K}_1, \boldsymbol{K}_2). \tag{3.39}$$

The average RET rate is given by

$$\Gamma_{12} = \frac{2\pi}{\hbar} \sum_{s_1,s_2} \sum_{\boldsymbol{K}_1,\boldsymbol{K}_2} \frac{e^{-\beta\Omega_{s_1}}}{\mathcal{Z}} |M_d|^2 \delta(\Omega_{s_1} - \Omega_{s_2}), \tag{3.40}$$

where $\mathcal{Z} = \mathrm{tr}\{\exp(-\beta\mathcal{H})\}$ is the partition function corresponding to $1/\beta = k_B T$. Considering the conservation of the continuous components of wave vectors $\boldsymbol{K}_1$ and $\boldsymbol{K}_2$ in the matrix element M_d, we get

$$\begin{aligned}
\Gamma_{12} =& \frac{2\pi}{\hbar} \sum_{s_1,s_2} \sum_{\boldsymbol{K}_1} \sum_{\mathscr{M}_2} \frac{e^{-\beta\Omega_{s_1}}}{\mathcal{Z}} \left| C(\mathscr{M}_1, \mathscr{M}_2; K_1) \times Q(\boldsymbol{K}_1, \boldsymbol{K}_2') \right|^2 \delta(\Omega_{s_1} - \Omega_{s_2}') \\
=& \frac{2\pi}{\hbar} \frac{L}{2\pi} \sum_{s_1,s_2} \sum_{\mathscr{M}_1} \sum_{\mathscr{M}_2} \int dK_1 \frac{e^{-\beta\Omega_{s_1}}}{\mathcal{Z}} \left| C(\mathscr{M}_1, \mathscr{M}_2; K_1) Q(\boldsymbol{K}_1, \boldsymbol{K}_2') \right|^2 \delta(\Omega_{s_1} - \Omega_{s_2}') \\
=& \frac{L}{\hbar} \sum_{s_1,s_2} \sum_{\boldsymbol{K}_1''} \sum_{\mathscr{M}_2} \frac{e^{-\beta\Omega_{s_1}}}{\mathcal{Z}} \left| C(\mathscr{M}_1, \mathscr{M}_2; K_1'') \times Q(\boldsymbol{K}_1'', \boldsymbol{K}_2') \right|^2 \left(\frac{dK_1}{d\Omega_{s_1}} \right)_{\Omega_{s_1}''}
\end{aligned} \tag{3.41}$$

The primed quantities in the last relation show the excitonic states in the acceptor CNT that conserve the continuous component of the center-of-mass wave vector, i.e., $K_2 = K_1$. The

double-primed quantities represent the excitonic states on the donor CNT that conserve both the energy and the continuous part of the center-of-mass momentum in the transfer process, i.e., $\Omega_{s_1}(\mathscr{M}_1, K_1) = \Omega_{s_2}(\mathscr{M}_2, K_1)$. We should note that the final RET rate is independent of the CNT length as the partition function, $\mathscr{Z}$, is linearly dependent on the length of the donor CNT

$$\begin{aligned}\mathscr{Z} =& \sum_{s_1}\sum_{\boldsymbol{K}_1} e^{-\beta\Omega_{s_1}(\boldsymbol{K}_1)} \\ =& \frac{L}{2\pi}\sum_{s_1}\sum_{\mathscr{M}_1}\int dK_1\ e^{-\beta\Omega_{s_1}(\boldsymbol{K}_1)},\end{aligned} \tag{3.42}$$

which cancels the parameter L in the Eq. (3.41), so we obtain

$$\begin{aligned}\Gamma_{12} =& \frac{2\pi}{\hbar}\left[\sum_{s_1}\sum_{\mathscr{M}_1}\int dK_1\ e^{-\beta\Omega_{s_1}(\boldsymbol{K}_1)}\right]^{-1} \times \\ & \left[\sum_{s_1,s_2}\sum_{\boldsymbol{K}_1''}\sum_{\mathscr{M}_2} e^{-\beta\Omega_{s_1}}\left|C(\mathscr{M}_1,\mathscr{M}_2;K_1'')\times Q(\boldsymbol{K}_1'',\boldsymbol{K}_2')\right|^2\left(\frac{dK_1}{d\Omega_{s_1}}\right)_{\Omega_{s_1}''}\right].\end{aligned} \tag{3.43}$$

3.4 Results and discussion

In this Section, we calculate the resonant exciton transfer (RET) rates between four different tube chiralities: (7,5), (7,6), (8,6), and (8,7). The energies of the lowest bright excitonic states in these CNTs are shown in Table 3.1. Figure 3.3 shows a comparison of the dispersions of optically active S_{11} and S_{22} excitonic states in (7,5) and (8,7) CNTs. We have taken the separation between the centers of donor and acceptor CNTs to be 1.2 nm, which provides enough wall-to-wall distance ($\approx 2\,\text{Å}$) between the CNTs under consideration that the exchange Coulomb interaction is negligible.

We calculate the RET rates across different combinations of transition subbands (i.e., $S_{ii} \to S_{jj}$). Moreover, we calculate the RET rate between optically bright and optically dark excitonic states. We report on the dependence of the RET rate on the angle between the donor and acceptor tubes. Next, we study the effect of exciton confinement on the RET rate. Furthermore, we show that the exciton thermalization among both dark and bright states

Chirality	S_{11} energy [eV]	S_{22} energy [eV]
$(7,5)$	1.136	2.08
$(7,6)$	1.053	1.974
$(8,6)$	1.014	1.849
$(8,7)$	0.9004	1.697

Table 3.1: Energy of the lowest bright excitonic states for selected SWNTs.

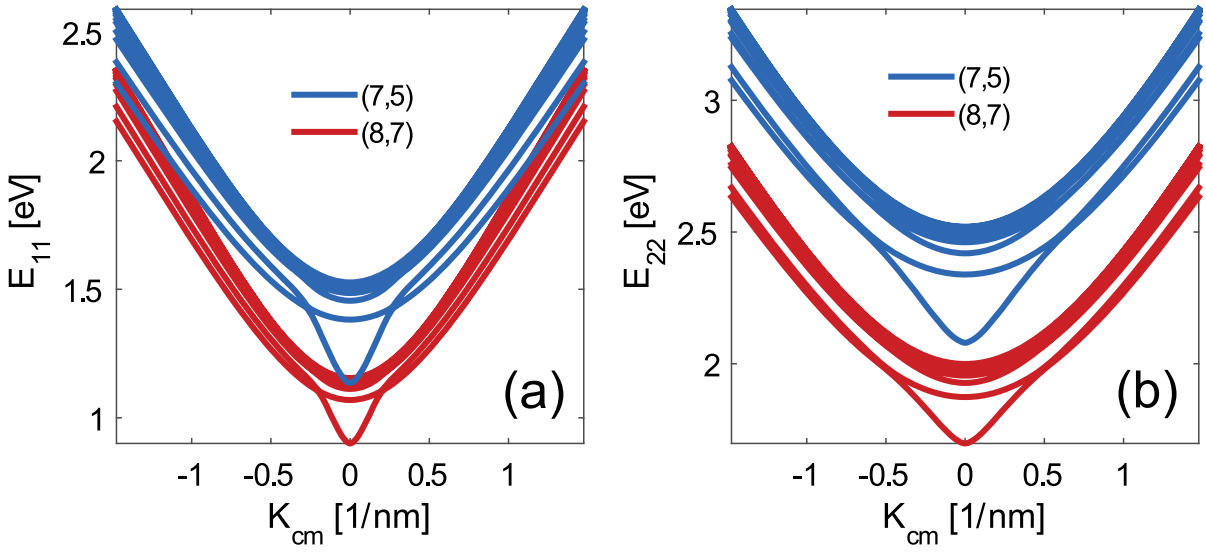

Figure 3.3: Comparison of S_{11} (a) and S_{22} (b) excitonic energy dispersions in (7,5) and (8,7) CNTs.

can reduce the RET rate by an order of magnitude. Also, we study the RET-rate variation with varying electrostatic screening due to inhomogeneities in the surrounding medium.

3.4.1 Interband and intraband exciton-transfer rates

First, we calculate the RET rate as a function of the relative angle between donor and acceptor CNTs (angle θ in Fig. 3.1). Owing to the radiative nature of the direct RET (Figure 1.4), we expect the exciton transfer between bright excitonic states to be the dominant transfer process. Figure 3.4 shows the transfer rate of bright excitons (A_2) from donor CNTs

with larger band gaps to acceptor CNTs with smaller band gaps (downhill transfer). The uphill RET process is usually a couple of orders of magnitude smaller, because in this case the excitonic states in the donor tube that can resonate with the acceptor-tube states have low exciton population. In Fig. 3.4, the excitons belong to the same transition subbands in donor and acceptor CNTs (intraband exciton transfer). We assume that the excitons are confined inside a 10 nm long quantum well, similar to the work by Wong *et al.* [59] We observe a relatively small dependence of the RET rate on the relative angle between CNTs. This is in contrast with the prediction by Wong *et al.* [59], who calculated that the transfer rate would drop to zero when the donor and acceptor tubes are perpendicular. This discrepancy stems from the method employed by Wong *et al.*: they used a formulation that assumes that the Coulomb interaction matrix element, Eq. (3.12), is almost constant between excitonic states with different energies. However, our detailed derivation shows that one needs to calculate the interaction matrix element for each pair of states in donor and acceptor CNTs [see Eq. (3.26)]. In addition, our calculated rates is in excellent agreement with the study by Qian *et al.*, who measured a lifetime of $\tau \approx 0.5$ ps for exciton transfer between two nonparallel CNTs [54].

Moreover, the RET rate is slightly higher between S_{11} states than the transfer rate between S_{22} states. This lower transfer rate can be explained from the point of view that the direct RET is a process of simultaneous emission and absorption of a virtual photon by the donor and acceptor systems, respectively. The S_{22} excitonic states that are in resonance between the donor and acceptor tubes on average have a higher center-of-mass momentum, which yields a lower photon emission rate [27, 69]. The lower rate of photon emission yields a lower RET rate between S_{22} states.

Next, we look at the contribution of dark excitonic states in the RET process. When the separation between the donor and acceptor molecules is larger than the size of each molecule, the traditional Förster theory is applied to calculate the exciton-transfer rate. In this case, the transfer process depends on the overlap between the emission and absorption spectra of the donor and acceptor molecules, respectively. Therefore, the dark excitonic states do

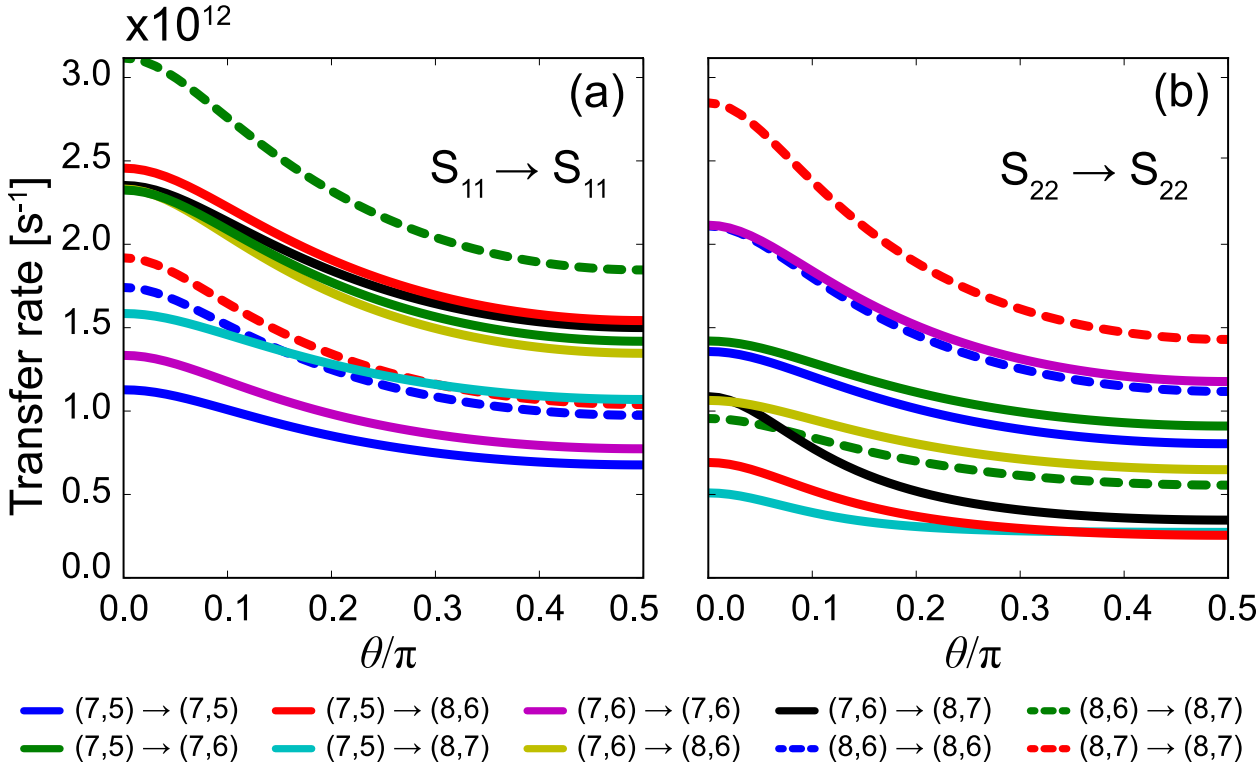

Figure 3.4: A_2 exciton-transfer rate versus relative angle between donor and acceptor CNTs. (a) $S_{11} \rightarrow S_{11}$ and (b) $S_{22} \rightarrow S_{22}$.

not contribute to the exciton transfer process. However, in the case of exciton transfer between neighboring CNTs, the Förster theory fails, as the donor and acceptor molecules are relatively large [59]. Therefore, some dark excitonic states could contribute to the energy-transfer process. Figure 3.5 shows the downhill RET rate to or from dark E-type excitonic states among four CNT types. These transfer rates are about two orders of magnitude smaller than the transfer rates among bright excitonic states (Fig. 3.4), owing to the large angular momentum of E-type excitons. However, Postupna *et al.* [60] suggested that the phonon-assisted processes could facilitate efficient exciton transfer from/to dark excitonic states [60]. Postupna *et al.* used time-dependent density functional theory (TDDFT) in conjunction with molecular dynamic (MD) to study phonon-assisted exciton hopping. Owing to numerical reasons, their study was limited to the ET process between two arrays of CNTs with a relative angle of 90°.

We should note that the dark A_1 excitonic states still do not contribute to the exciton transfer process because of symmetry considerations that hold beyond the dipole approximation [38].

Next, we look at the RET process from the S_{22} excitonic states in the donor tube to the S_{11} excitonic states in the acceptor tube (interband exciton transfer). As we see in Fig. 3.6, the interband energy transfer process occurs almost as fast as the intraband exciton transfer process shown in Fig. 3.4. In order to better understand the role of different excitonic states in the excitation energy transfer process, we calculated the intraband ($S_{11} \rightarrow S_{11}$ and $S_{22} \rightarrow S_{22}$) and interband ($S_{22} \rightarrow S_{11}$) exciton-transfer rates considering only the exciton transfer process between tightly bound excitonic states below the continuum level[2] [white dashed line in the inset to Fig. 3.6(a)]. The calculated *intraband* transfer rates did not change significantly from the case that included both tightly bound excitonic states and the continuum states (in other words, they remain similar to those depicted in Fig. 3.4). However, the *interband* exciton-transfer rates decreased by about two orders of

[2]The continuum level is the minimum energy level beyond which the excitonic state can essentially be considered as free-electron and free-hole states.

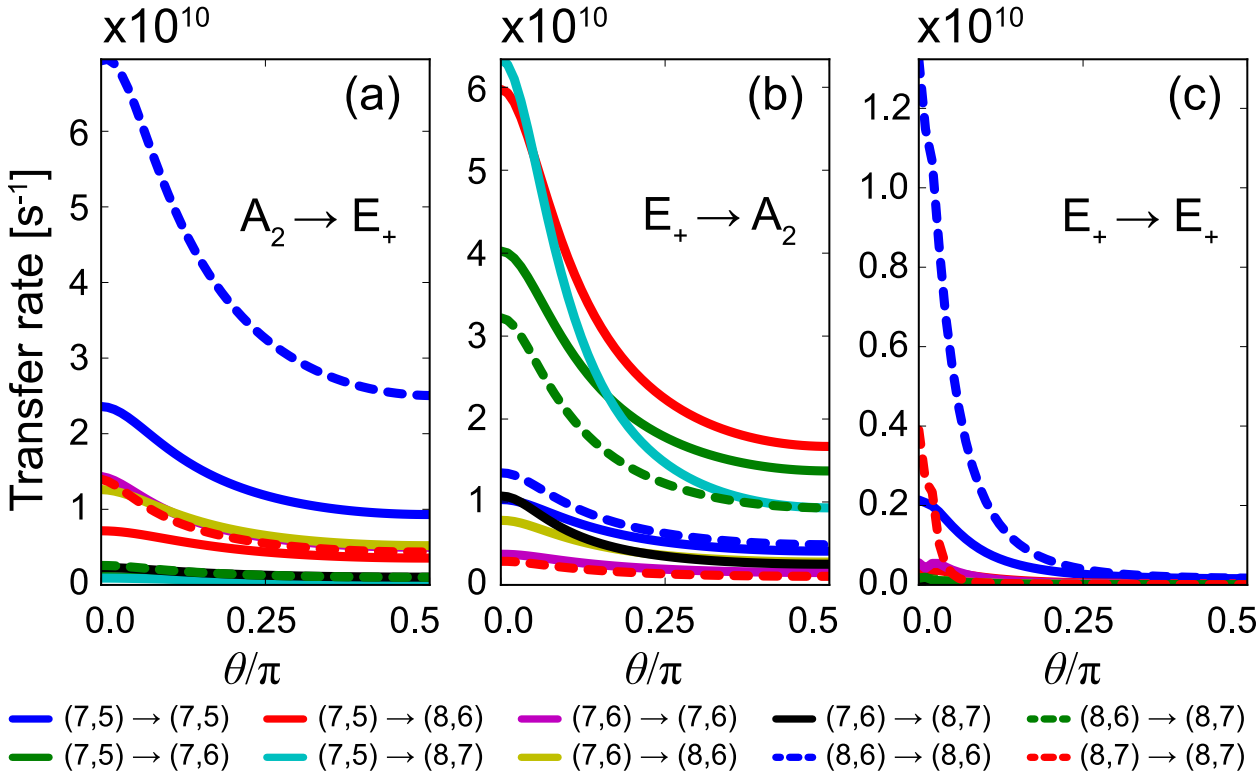

Figure 3.5: Transfer rate for processes involving dark E_+ excitons versus relative orientation of the donor and acceptor tubes and for different tube chiralities. (a) A_2 to E_+, (b) E_+ to A_2, and (c) E_+ to E_+.

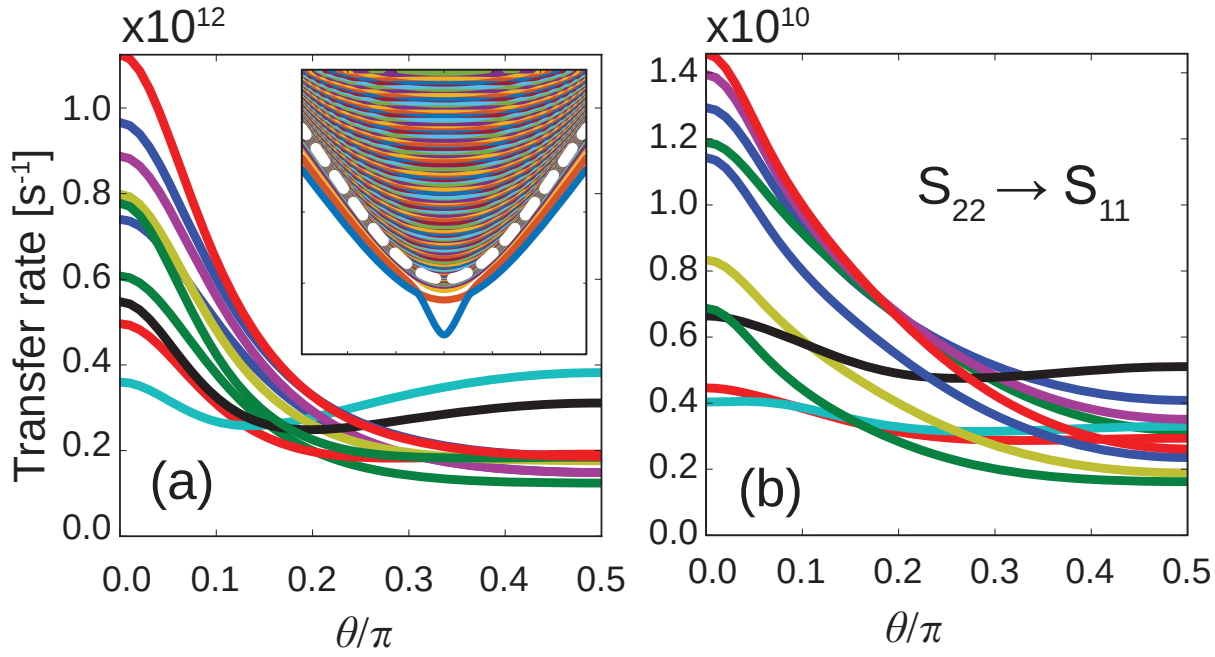

Figure 3.6: (a) Transfer rate of bright S_{22} excitonic states to bright S_{11} excitonic states as a function of tube orientation when considering all excitonic states, both tightly bound and continuum. (Inset) Dispersions of bound and continuum excitonic states, separated by a dashed white line that denotes the lowest continuum level. (b) Transfer rate of bright S_{22} excitonic states to bright S_{11} excitonic states as a function of tube orientation when considering only bound excitonic states.

magnitude when the continuum states were eliminated [compare Fig. 3.6(a) to Fig. 3.6(b)]. We conclude that, although there are many transition states in the continuum region that resonate between the donor and acceptor states, they do not contribute to the intraband exciton transfer process. In contrast, most of the interband exciton transfer processes occur from tightly bound excitonic states to these continuum states.

3.4.2 Exciton confinement effect

Owing to various forms of disorder (e.g., the nonuniformity in the dielectric properties of the surrounding environment and the presence of charged impurities in the CNT samples),

an exciton can be confined in quantum wells along the CNT. In this section, we study the effect of quantum-well size on the resonant exciton-transfer rate. For relatively wide quantum wells, which yield excitonic states with small energy spacing, the matrix element of the Coulomb interaction and the calculated ET rate are affected only by the change in the geometric part of the matrix element [Eq. (3.21)]. Therefore, we calculate the ET rate through Eq. (3.38), where the spatial extent of the quantum well is used in calculating the geometric part of the matrix element [Eq. (3.21)].

Figure 3.7(a) [Figure 3.7(b)] shows the RET rate between bright excitonic states when the donor and acceptor SWNTs have similar (different) chiralities. It is assumed that the sizes of quantum wells in donor and acceptor SWNTs are the same.

When the CNTs are not parallel, the exciton-transfer rate drops with increasing size of the quantum wells because the average spacing between the donor and acceptor systems increases. We can see this length dependence in Eq. (3.38). However, in a CNT sample with a constant density of tubes, the number of available acceptor tubes is proportional to the length of the donor CNT. Therefore, we introduce the exciton-transfer rate per unit length of the donor tube [Fig. 3.8(a)]. The exciton-transfer rate per unit length changes up to a factor of three due to the variation of the geometric part of matrix element [Eq. (3.38)]. Nevertheless, the transfer rate stays relatively constant as we go to the limit of free-exciton-transfer rates.

We observe a different behavior when the donor and acceptor tubes are parallel. This case is particularly important because, in many samples, the CNTs stick together and form CNT bundles. Unlike the case of nonparallel CNTs, we do not observe a drop in the resonant exciton-transfer rate with increasing size of quantum wells, as the average distance between the donor and acceptor states is almost independent of this size. We can predict this behavior based on the analytical expressions from previous sections.

Furthermore, based on the chirality of the donor and acceptor CNTs, the exciton-transfer rates follow different trends as the size of quantum wells increases. For small confinement lengths, the exciton center-of-mass momenta in initial and final states are not important

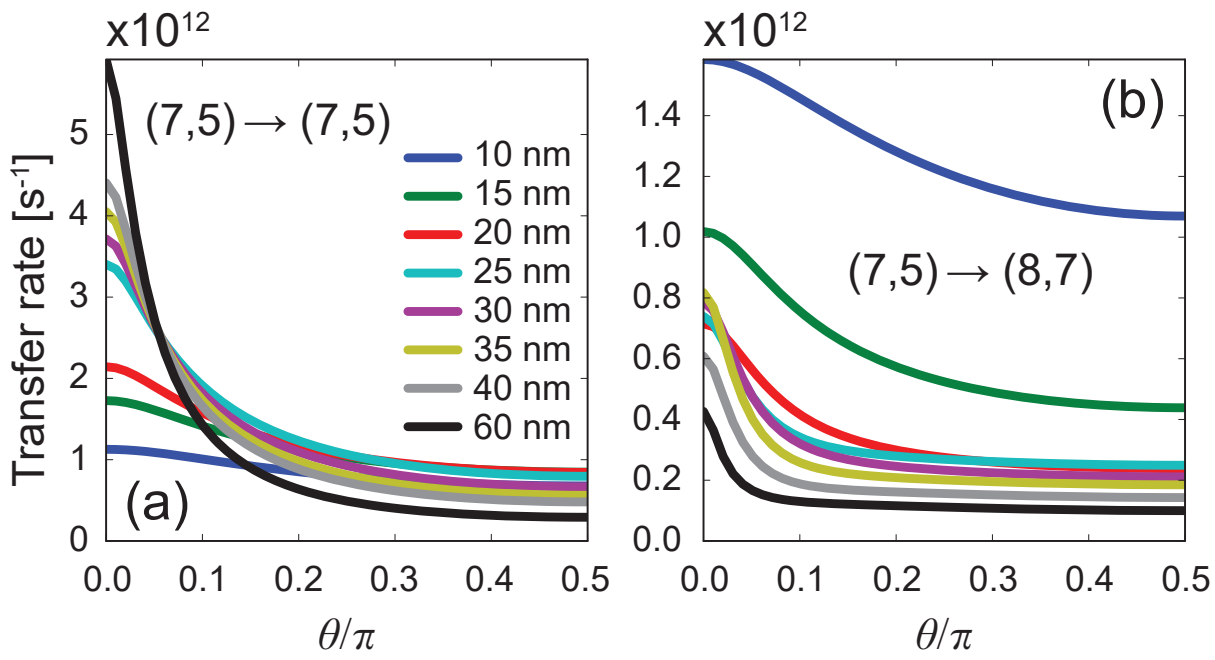

Figure 3.7: Exction transfer rate from bright excitonic states of a donor (7,5) SWNT to the bright excitonic states of (7,5) (panel a) and (8,7) (panel b) acceptor SWNTs. Different colors show the transfer rates of excitons with various quantum well sizes.

factors in determining the strength of Coulomb coupling; therefore, there are many states in the acceptor tube that can resonate with the donor-tube excitonic states. However, as the confinement length increases, the contribution from the excitonic states that do not conserve momentum drops. In the limit of free-exciton transfer, only the states that conserve both the center-of-mass momentum and energy can transfer between the CNTs. Therefore, when the excitonic energy dispersions in the donor and acceptor tubes are dissimilar (e.g., due to different chiralities), a limited number of states contribute to the exciton transfer process. This results in a decrease of the exciton-transfer rate. On the other hand, if the donor and acceptor CNTs have similar dispersion curves, there are many excitonic states that conserve both momentum and energy in donor and acceptor CNTs, which increases the exciton-transfer rate by about two orders of magnitude (Fig. 3.8).

These findings are in excellent agreements with measurements. Lüer *et al.* have measured ET rates between S_{11} states within bundles of CNTs that exceed 10^{14} s^{-1} [55]. They also reported limited ET rate between S_{22} states which is due to the same momentum-matching considerations that we have discussed here. Recently, Mehlenbacher *et al.* studied ET in samples where CNTs are wrapped in polymers and in samples with no residual surfactant [56, 58, 70]. They found that, in the samples with no polymer wrapping, the ET rate between parallel CNTs is extremely fast, with < 60 fs time scales. Two-dimensional anisotropy measurements showed much slower ET rates between nonparallel CNTs in these samples. On the other hand, Mehlenbacher *et al.* found picosecond time scales for ET rates in samples where CNTs are wrapped in polymers. In these samples, ET shows no preference between parallel and nonparallel relative orientation of donor and acceptor CNTs. Our calculations agree very well with these experimental findings: in pristine samples (thus no exciton confinement), we expect high transfer rates between same-chirality parallel tubes (10^{14} s^{-1}) and much lower rates when the tubes are misoriented. In samples with polymer residue, excitons exhibit confinement, which drastically reduces the rate of transfer between parallel tubes and results in isotropic ET rates of around 10^{12} s^{-1}.

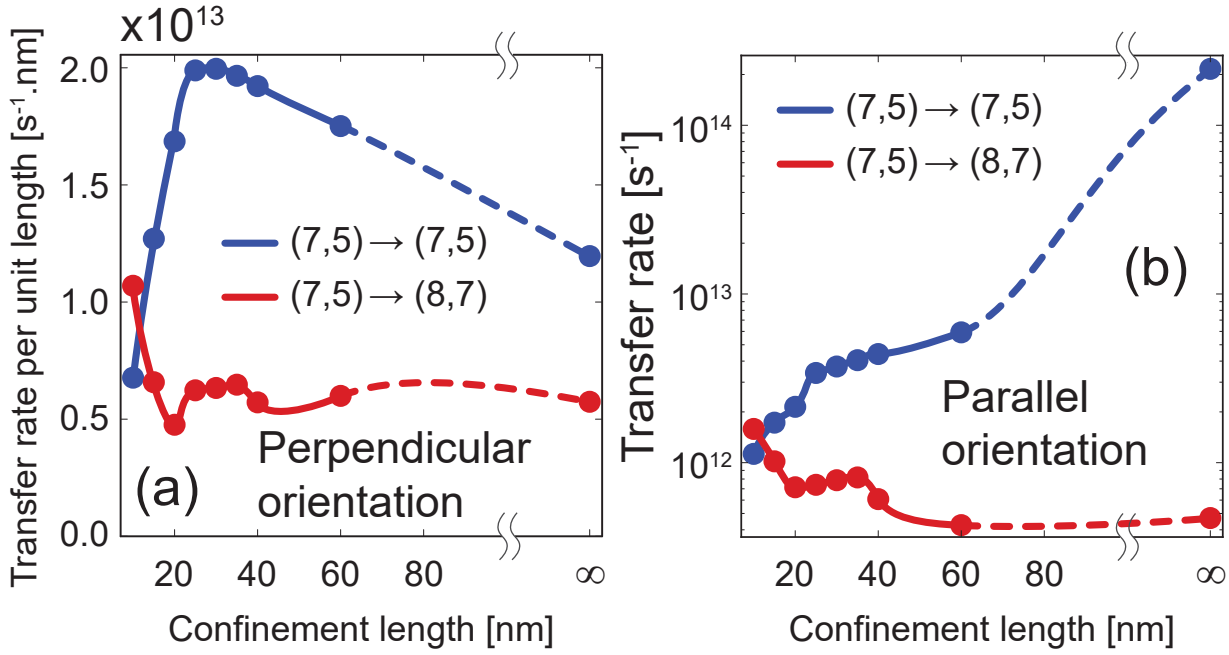

Figure 3.8: (a) The exciton-transfer rate per unit length between perpendicular donor and acceptor SWNTs as a function of exciton confinement length. (b) The exciton-transfer rate between parallel donor and acceptor SWNTs as a function of exciton confinement length.

3.4.3 Effect of static screening by surrounding medium

Like most quasi-one-dimensional nanostructures, the electronic and optical properties of CNTs are influenced by their surrounding medium. One of these environmental effects is the screening of electrostatic electron–electron and electron–hole interactions inside a CNT. As we discussed before, the relative dielectric permittivity κ in Eq. (2.23) accounts for the screening due to the surrounding medium and the core electrons in CNTs. As κ increases, the self-energy due to repulsive electron–electron interaction and the binding energy due to the attractive electron–hole interaction decreases [71]. As shown in Fig. 3.9(a), the net effect is a decrease in exciton energy with increasing permittivity. In the limit of infinite permittivity, we retrieve the noninteracting electron results. Figure 3.9 shows the energy dispersions for bright excitonic states assuming various values of κ. As expected, the binding energy and the number of tightly bound excitonic states decrease with increasing permittivity.

Screening of the Coulomb interactions via the surrounding medium affects the ET rates in two ways: by changing the exciton wavefunction and dispersion energy (intratube screening effect) and by changing the electron–electron interaction between the donor and acceptor CNTs (intertube screening effect). The first effect stems from the change in the permittivity of the environment in the small area around the donor/acceptor CNT (we denote this permittivity by κ), whereas the second effect happens through changes in the average permittivity of the environment over long distances in the sample (we capture this effect through $\bar{\kappa}$). While $\bar{\kappa}$ and κ are generally not the same, for simplicity here we assume that they are. Figure 3.10(a) shows the RET rate between bright excitonic states as a function of the environment relative permittivity when only the first effect is taken into account. The drop in the RET rate with increasing relative permittivity can be explained by looking at the photon absorption and emission rates. For higher permittivities, the excitonic states are more like free-electron and free-hole states than like bound excitons, and thus have lower photon absorption and emission rates [69]. Consequently, the rate of RET, which is simultaneous photon emission and photon absorption by the two tubes, decreases. Figure 3.10(b) shows the exciton-transfer rate between bright excitonic states as a function of Coulomb screening

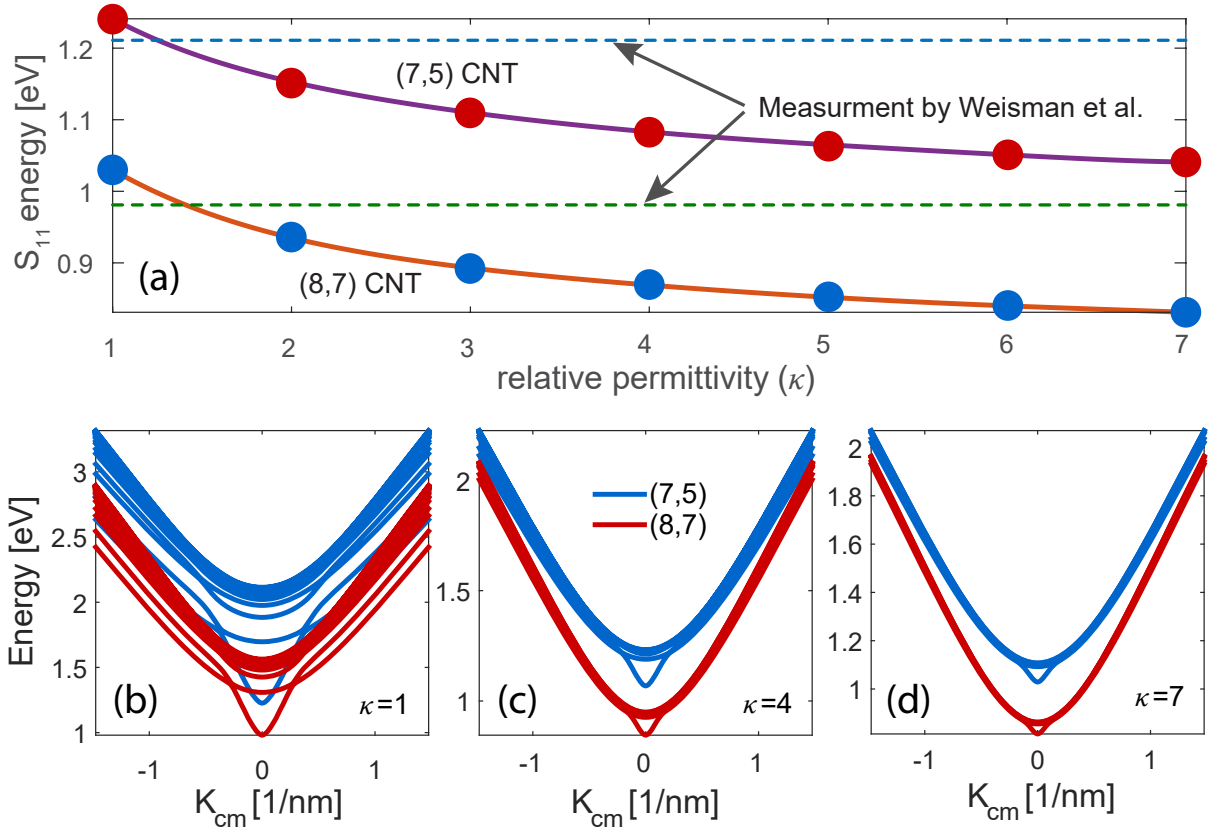

Figure 3.9: (a) Lowest transition energies in (7,5) and (8,7) SWNTs as a function of relative permittivity. (b) – (d) Exciton dispersions with various relative dielectric permittivities of the environment.

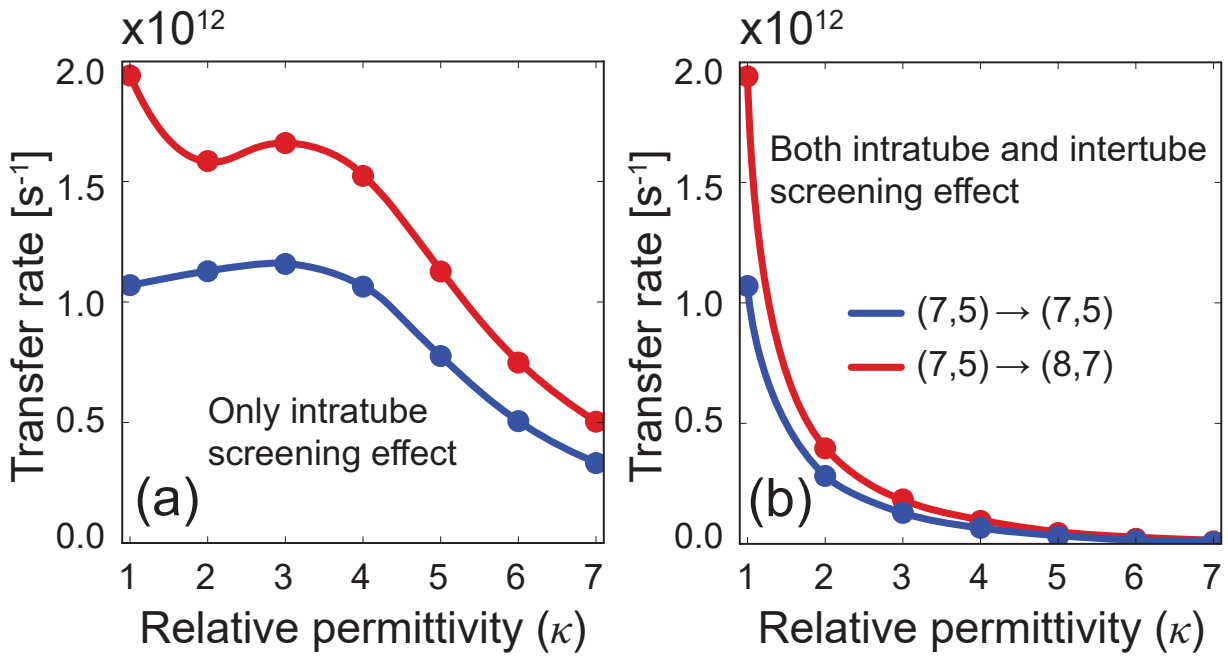

Figure 3.10: Exciton-transfer rate between (7,5) and (8,7) CNTs as a function of environment relative permittivity when (a) only the intratube screening effect is taken into account and (b) both intertube and intratube screening effects are taken into account.

when accounting for both effects of screening. In this case, the drop in the RET rate with increasing permittivity is much more significant than in the previous case. This major drop is a result of a smaller perturbing Hamiltonian, which has a dependence of $\hat{H}_{\mathrm{d}} \propto \frac{1}{\kappa}$.

3.4.4 Interband exciton thermalization

As we discussed earlier, the excitonic states in CNTs are classified as bright and dark states. The former exciton type is created via optical stimulation of ground-state electrons and the latter is usually populated through some second-order processes, such as Raman scattering or the scattering of bright excitons into dark excitons by phonons and impurities. So far, we have studied the intrinsic exciton-transfer rate from either bright or dark excitonic states. However, if the exciton scattering between bright and dark states is fast enough

(compared to the exciton transfer process), the excitons are thermalized among both bright and dark states and we have to consider both in the transfer process.

Figure 3.11 shows the exciton-transfer rate as a function of temperature for the full exciton thermalization among bright and dark excitonic states [Fig. 3.11(a)] and among bright states only [Fig. 3.11(b)]. In the presence of exciton thermalization process between bright and dark excitonic states, we observe a twentyfold decrease in the exciton-transfer rate. This is because of the presence of low-lying triplet states and the symmetric singlet states that do not transfer through the direct Coulomb interaction. As the temperature decreases to $T = 0$ K, the excitons only populate these low-lying states and the transfer rate goes to zero. In addition, we note that the intrisic transfer rate between bright excitonic decreases when temperature drops. This trend is contrary to the behavior of the radiative exciton decay rate predicted by Perebeinos *et al.* [41]

3.5 Conclusion

In summary, we calculated the resonant exciton-transfer rates between semiconducting CNTs of different chiralities and relative orientations. The resonant exciton-transfer rate is weakly dependent on the orientation of the tubes. This finding is in contradiction with previous theoretical studies, but in good agreement with experiments. The resonant exciton-transfer rate between bright excitonic states is about 2×10^{12} s^{-1}. The transfer rates between bright and dark states are at least two orders of magnitude smaller that the transfer rates among bright excitonic states. We also looked at the exciton transfer from S_{22} to S_{11} transition energies. We found that this type of exciton transfer process is as fast as transfer from S_{11} to S_{11} and from S_{22} to S_{22} states. This process is facilitated by coupling of tightly bound excitonic states in S_{22} to the continuum-level states (equivalent of free-electron/free-hole states) in S_{11}.

Furthermore, we studied the environmental effects on the resonant exciton-transfer rates. We calculated the exciton-transfer rate for excitons confined to quantum wells with various sizes. When the quantum-well size increases, we observed a decrease in the transfer rate

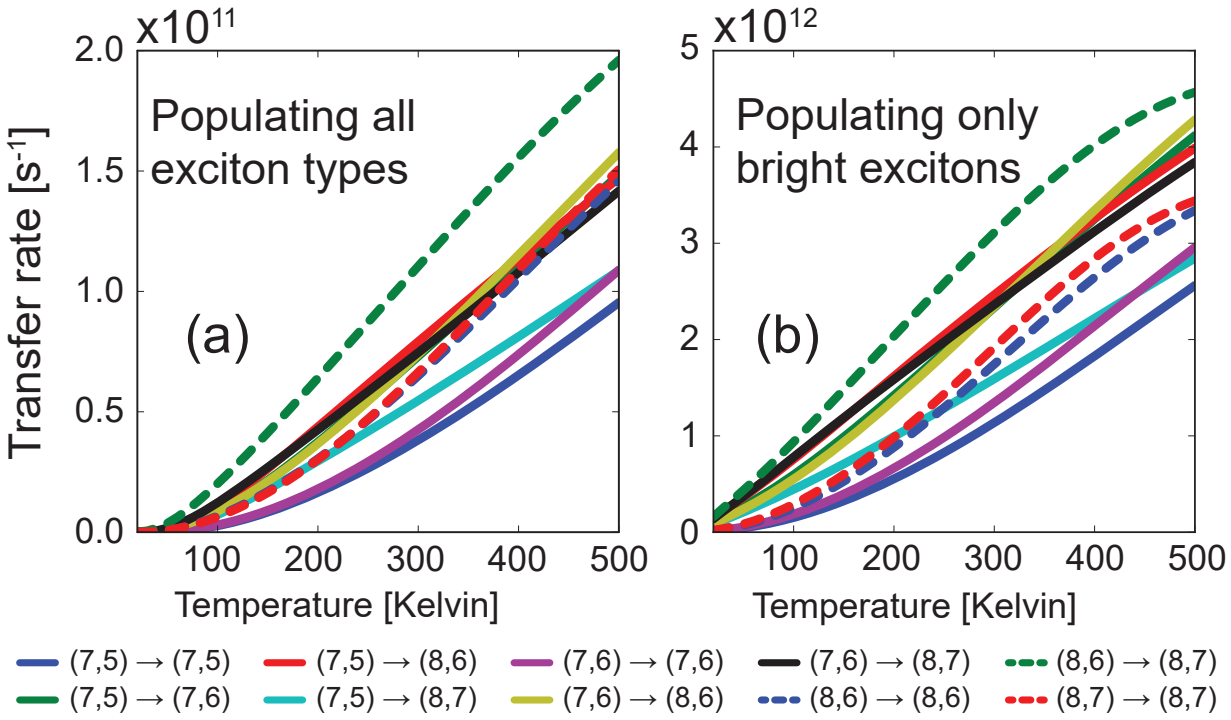

Figure 3.11: The exciton-transfer rate of excitons between CNTs (a) when the excitons are thermalized between both bright and dark excitonic states and (b) when only the bright excitonic states are populated. The donor and acceptor CNTs are parallel and the excitons are assumed to be confined in a 10 nm wide quantum well.

between nonparallel tubes. This is because of the increase in the average distance between donor and acceptor systems. By introducing a more relevant quantity (i.e., transfer rate per donor tube length), we showed that the exciton-transfer rate is almost independent of the exciton confinement length. However, exciton transfer between parallel tubes follows a different trend: transfer between same-chirality donor and acceptor tubes is extremely sensitive to confinement and free excitons have the highest transfer rate ($> 10^{14}$ s^{-1}). The transfer rates between different-chirality tubes are not as sensitive to confinement and only slightly increase with decreasing confinement length. These findings are a result of momentum conservation rules.

Moreover, we looked at the effect of Coulomb screening due to the surrounding medium. The exciton-transfer rate decreases with increasing screening. We also showed that the exciton-transfer rate increases with increasing temperature. This behavior is the opposite of what one would expect based on the emission and absorption spectra of donor and acceptor systems. Also, we showed that the exciton-transfer rate drops by about one order of magnitude if excitons are thermalized between bright and dark excitonic states via extrinsic scattering sources (e.g., impurities and phonons).

We conclude that the wide range of ET-rate measurements, spanning two orders of magnitude, stems from variations in sample preparation and thus the degree of environmental disorder and homogeneity, as the ET rates in pristine samples and in the samples in which environmental disorder results in exciton confinement differ by two orders of magnitude.

Chapter 4

Exciton–Phonon Interaction

In this Chapter, we use the Su-Schrieffer-Heeger model to derive the interaction Hamiltonian between excitons and phonons in CNTs. The derived Hamiltonian is used in the next Chapter to study the nonresonant exciton transfer in CNTs.

4.1 Model Hamiltonian

Here, we use the Su-Schrieffer-Heeger (SSH) model Hamiltonian to calculate the electron–phonon scattering rate in graphene. As a first approximation, we can use the same relation for the calculation of electron–phonon scattering rate in carbon nanotubes (CNTs). However, more calculations are needed if we want to include scattering by the radial breathing mode (RBM) phonons, which are specific to CNTs.

The tight-binding Hamiltonian for an electron in graphene sheet in the second-quantization representation is

$$\hat{H} = \sum_{\langle u,u' \rangle} t_{u,u'} \left(\hat{a}^{\dagger}_{uA} \hat{a}_{u'B} + \hat{a}^{\dagger}_{u'B} \hat{a}_{uA} \right), \tag{4.1}$$

where $\hat{a}_{uA}$ and $\hat{a}_{uB}$ are the annihilation operator of an electron in an orbital located in basis atom A and B of unit cell u, respectively. We have assumed that the orbital centered around different atoms are normalized and have zero overlap. We have also taken the reference of potential energy so that the energy of putting a single electron in one of the orbitals is zero. The sum over $\langle u, u' \rangle$ represents the sum over the first nearest-neightbors. $t_{u,u'}$ is called the hopping energy from atom uA to one of its nearest-neighbor atoms $u'B$.

The SSH model assumes that the hopping energy changes linearly with respect to the change in the distance of atoms uA and $u'B$

$$t_{u,u'} = t_0 - g\boldsymbol{e}_{uu'}.(\boldsymbol{r}_{uA} - \boldsymbol{r}_{u'B}). \tag{4.2}$$

Here, t_0 is the hopping energy when atoms are in equilibrium position and g is the electron–phonon coupling constant, which is 5.3 eV/Åin graphene [72]. $\boldsymbol{e}_{uu'}$ is the unit vector in the direction of the bond between atoms uA and $u'B$. $\boldsymbol{r}_{uA}$ and $\boldsymbol{r}_{u'B}$ are the atomic displacements of atoms uA and $u'B$ due to phonons, respectively. The displacement field of basis atom b in the unit cell u is

$$\hat{\boldsymbol{r}}_{ub} = \sum_{q,\lambda} \left(\frac{\hbar}{2N_u m_b \omega_\lambda(\boldsymbol{q})} \right)^{\frac{1}{2}} e^{-i\boldsymbol{q}.\boldsymbol{R}_u} \boldsymbol{e}_{b,\lambda}(\boldsymbol{q}) \left(\hat{c}^\dagger_\lambda(\boldsymbol{q}) + \hat{c}_\lambda(-\boldsymbol{q}) \right), \tag{4.3}$$

where N_u is the number of unit cells in graphene and m_b is the mass of atom b in the basis. $\boldsymbol{R}_u$ is the position vector of unit cell u and $\boldsymbol{e}_{b,\lambda}(\boldsymbol{q})$ is the unit vector in the direction of displacement of atom b due to the propagation of a phonon in branch λ with wave vector $\boldsymbol{q}$. The atomic displacement fields are Hermitian given that

$$\boldsymbol{e}_{b,\lambda}(\boldsymbol{q}) = \boldsymbol{e}^*_{b,\lambda}(-\boldsymbol{q}) \quad \text{and} \quad \omega_\lambda(\boldsymbol{q}) = \omega_\lambda(-\boldsymbol{q}). \tag{4.4}$$

Now, we can split the total Hamiltonian into the unperturbed electron ($\hat{H}_{\text{el}}$) and electron–phonon interaction ($\hat{H}_{\text{el-ph}}$) Hamiltonians

$$\hat{H} = \hat{H}_{\text{el}} + \hat{H}_{\text{el-ph}}, \tag{4.5a}$$

$$\hat{H}_{\text{el}} = t_0 \sum_{\langle u,u' \rangle} \left(\hat{a}^\dagger_{uA} \hat{a}_{u'B} + \hat{a}^\dagger_{u'B} \hat{a}_{uA} \right), \tag{4.5b}$$

$$\hat{H}_{\text{el-ph}} = -g \sum_{\langle u,u' \rangle} \boldsymbol{e}_{uu'}.(\hat{\boldsymbol{r}}_{uA} - \hat{\boldsymbol{r}}_{u'B}) \left(\hat{a}^\dagger_{uA} \hat{a}_{u'B} + \hat{a}^\dagger_{u'B} \hat{a}_{uA} \right). \tag{4.5c}$$

In the following two sections, we write $\hat{H}_{\text{el}}$ and $\hat{H}_{\text{el-ph}}$ in terms of the creation and annihilation operators in the k-space.

4.2 Electronic States

Now, we find a basis to diagonalize the unperturbed electronic Hamiltonian $\hat{H}_{\text{el}}$. We introduce the following creation and annihilation operators as the Fourier transform of previous creation and annihilation operators of local orbitals

$$\hat{d}_A(\boldsymbol{k}) = \frac{1}{\sqrt{N_u}} \sum_u e^{-i\boldsymbol{k}.\boldsymbol{R}_{uA}} \hat{a}_{uA} \quad , \quad \hat{d}_A^\dagger(\boldsymbol{k}) = \frac{1}{\sqrt{N_u}} \sum_u e^{+i\boldsymbol{k}.\boldsymbol{R}_{uA}} \hat{a}_{uA}^\dagger, \tag{4.6a}$$

$$\hat{d}_B(\boldsymbol{k}) = \frac{1}{\sqrt{N_u}} \sum_u e^{-i\boldsymbol{k}.\boldsymbol{R}_{uB}} \hat{a}_{uB} \quad , \quad \hat{d}_B^\dagger(\boldsymbol{k}) = \frac{1}{\sqrt{N_u}} \sum_u e^{+i\boldsymbol{k}.\boldsymbol{R}_{uB}} \hat{a}_{uB}^\dagger. \tag{4.6b}$$

Likewise, we can use the inverse Fourier transform to get the creation and annihilation operators of local orbitals

$$\hat{a}_{uA} = \frac{1}{\sqrt{N_u}} \sum_u e^{+i\boldsymbol{k}.\boldsymbol{R}_{uA}} \hat{d}_A(\boldsymbol{k}) \quad , \quad \hat{a}_{uA}^\dagger = \frac{1}{\sqrt{N_u}} \sum_u e^{-i\boldsymbol{k}.\boldsymbol{R}_{uA}} \hat{d}_A^\dagger(\boldsymbol{k}), \tag{4.7a}$$

$$\hat{a}_{uB} = \frac{1}{\sqrt{N_u}} \sum_u e^{+i\boldsymbol{k}.\boldsymbol{R}_{uB}} \hat{d}_B(\boldsymbol{k}) \quad , \quad \hat{a}_{uB}^\dagger = \frac{1}{\sqrt{N_u}} \sum_u e^{-i\boldsymbol{k}.\boldsymbol{R}_{uB}} \hat{d}_B^\dagger(\boldsymbol{k}). \tag{4.7b}$$

The unperturbed electron Hamiltonian in terms of the new operators is

$$\begin{aligned} \hat{H}_{\text{el}} = t_0 \sum_{\boldsymbol{k},\boldsymbol{k}'} \Bigg(& \hat{d}_A^\dagger(\boldsymbol{k})\ \hat{d}_B(\boldsymbol{k}') \frac{1}{N_u} \sum_{\langle u,u' \rangle} e^{i(\boldsymbol{k}.\boldsymbol{R}_{u'B} - \boldsymbol{k}.\boldsymbol{R}_{uA})} + \cdots \\ & \cdots \hat{d}_B^\dagger(\boldsymbol{k}')\ \hat{d}_A(\boldsymbol{k}) \frac{1}{N_u} \sum_{\langle u,u' \rangle} e^{i(\boldsymbol{k}.\boldsymbol{R}_{uA} - \boldsymbol{k}'.\boldsymbol{R}_{u'B})} \Bigg). \end{aligned} \tag{4.8}$$

Now, we have

$$\begin{aligned} \frac{1}{N_u} \sum_{\langle u,u' \rangle} e^{i(\boldsymbol{k}'.\boldsymbol{R}_{u'B} - \boldsymbol{k}.\boldsymbol{R}_{uA})} &= \frac{1}{N_u} \sum_{\langle u,u' \rangle} e^{i\boldsymbol{k}'.(\boldsymbol{R}_{u'B} - \boldsymbol{R}_{uA})} e^{i(\boldsymbol{k}' - \boldsymbol{k}).\boldsymbol{R}_{uA}} \\ &= \delta(\boldsymbol{k}, \boldsymbol{k}')\ f(\boldsymbol{k}), \end{aligned} \tag{4.9}$$

where we have defined

$$f(\boldsymbol{k}) = \sum_{\langle 0,u' \rangle} e^{i\boldsymbol{k}.(\boldsymbol{R}_{u'B} - \boldsymbol{R}_{0A})}. \tag{4.10}$$

$f(\boldsymbol{k})$ for graphene is

$$f(\boldsymbol{k}) = \exp\left(i\boldsymbol{k}.\frac{\boldsymbol{a_1} + \boldsymbol{a_2}}{3}\right) + \exp\left(i\boldsymbol{k}.\frac{\boldsymbol{a_1} - 2\boldsymbol{a_2}}{3}\right) + \exp\left(i\boldsymbol{k}.\frac{\boldsymbol{a_2} - 2\boldsymbol{a_1}}{3}\right). \tag{4.11}$$

Likewise we can show that

$$\begin{aligned}\frac{1}{N_u}\sum_{\langle u,u'\rangle} e^{i(\boldsymbol{k}.\boldsymbol{R}_{uA}-\boldsymbol{k}'.\boldsymbol{R}_{u'B})} &= \frac{1}{N_u}\sum_{\langle u,u'\rangle} e^{i\boldsymbol{k}'.(\boldsymbol{R}_{uA}-\boldsymbol{R}_{u'B})}e^{i(\boldsymbol{k}-\boldsymbol{k}').\boldsymbol{R}_{uA}} \\ &= \delta(\boldsymbol{k},\boldsymbol{k}')\ f^*(\boldsymbol{k}).\end{aligned} \tag{4.12}$$

Now, the unperturbed Hamiltonian is

$$\begin{aligned}\hat{H}_{\text{el}} &= t_0\sum_{\boldsymbol{k}}\left(\hat{d}_A^\dagger(\boldsymbol{k})\ \hat{d}_B(\boldsymbol{k})f(\boldsymbol{k}) + \hat{d}_B^\dagger(\boldsymbol{k})\hat{d}_A(\boldsymbol{k})f^*(\boldsymbol{k})\right) \\ &= t_0\sum_{\boldsymbol{k}}|f(\boldsymbol{k})|\left(\hat{d}_A^\dagger(\boldsymbol{k})\hat{d}_B(\boldsymbol{k})e^{i\phi(\boldsymbol{k})} + \hat{d}_B^\dagger(\boldsymbol{k})\hat{d}_A(\boldsymbol{k})e^{-i\phi(\boldsymbol{k})}\right).\end{aligned} \tag{4.13}$$

Here, $\phi(\boldsymbol{k})$ is the phase of the function $f(\boldsymbol{k})$, therefore we have

$$e^{i\phi(\boldsymbol{k})} = \frac{f(\boldsymbol{k})}{|f(\boldsymbol{k})|}. \tag{4.14}$$

We define the new creation and annihilation operators as

$$\hat{\tilde{d}}_B(\boldsymbol{k}) = \hat{d}_B(\boldsymbol{k})e^{i\phi(\boldsymbol{k})} \quad , \quad \hat{\tilde{d}}_B^\dagger(\boldsymbol{k}) = \hat{d}_B^\dagger(\boldsymbol{k})e^{-i\phi(\boldsymbol{k})}. \tag{4.15}$$

Therefore, the unperturbed electron Hamiltonian is

$$\hat{H}_{\text{el}} = t_0\sum_{\boldsymbol{k}}|f(\boldsymbol{k})|\left(\hat{d}_A^\dagger(\boldsymbol{k})\hat{\tilde{d}}_B(\boldsymbol{k}) + \hat{\tilde{d}}_B^\dagger(\boldsymbol{k})\hat{d}_A(\boldsymbol{k})\right), \tag{4.16}$$

where it can be diagonalized by using the following operators

$$\hat{u}(\boldsymbol{k}) = \frac{1}{\sqrt{2}}\left(\hat{d}_A(\boldsymbol{k}) + \hat{\tilde{d}}_B(\boldsymbol{k})\right) \quad , \quad \hat{v}(\boldsymbol{k}) = \frac{1}{\sqrt{2}}\left(\hat{d}_A(\boldsymbol{k}) - \hat{\tilde{d}}_B(\boldsymbol{k})\right). \tag{4.17}$$

Here, $\hat{u}$ and $\hat{v}$ can be understood as the conduction band and valence band annihilation operators, respectively. The final form of the unperturbed electron Hamiltonian is

$$\hat{H}_{\text{el}} = t_0\sum_{\boldsymbol{k}}|f(\boldsymbol{k})|\left(\hat{u}^\dagger(\boldsymbol{k})\hat{u}(\boldsymbol{k}) - \hat{v}^\dagger(\boldsymbol{k})\hat{v}(\boldsymbol{k})\right), \tag{4.18}$$

which is diagonal in the basis of single-particle wavefunctions. We can see that, the energy of electrons in the conduction band is $+t_0 f(\boldsymbol{k})$, while the energy of electrons in the valence band is $-t_0 f(\boldsymbol{k})$.

4.3 Electron–phonon Interaction Hamiltonian

Now, we write the electron–phonon interaction Hamiltonian in terms of the conduction and valence band operators

$$
\begin{aligned}
\hat{H}_{\text{el-ph}} =& -g\sum_{\langle u,u'\rangle} \boldsymbol{e}_{uu'}.(\hat{\boldsymbol{r}}_{uA}-\hat{\boldsymbol{r}}_{u'B})\big(\hat{a}^{\dagger}_{uA}\hat{a}_{u'B}+\hat{a}^{\dagger}_{u'B}\hat{a}_{uA}\big)\\
=& -g\sum_{\boldsymbol{q},\lambda}\Bigg[\Big(\frac{\hbar}{2N_u m\omega_\lambda(\boldsymbol{q})}\Big)^{\frac{1}{2}}\big(\hat{c}^{\dagger}_{\lambda}(\boldsymbol{q})+\hat{c}_{\lambda}(-\boldsymbol{q})\big)\times\cdots\\
&\qquad\cdots\sum_{\langle u,u'\rangle}\boldsymbol{e}_{uu'}.\big(\boldsymbol{e}_{A,\lambda}(\boldsymbol{q})e^{-i\boldsymbol{q}.\boldsymbol{R}_u}-\boldsymbol{e}_{B,\lambda}(\boldsymbol{q})e^{-i\boldsymbol{q}.\boldsymbol{R}_{u'}}\big)\big(\hat{a}^{\dagger}_{uA}\hat{a}_{u'B}+\hat{a}^{\dagger}_{u'B}\hat{a}_{uA}\big)\Bigg]\\
=& -g\sum_{\boldsymbol{q},\lambda}\Bigg[\Big(\frac{\hbar}{2N_u m\omega_\lambda(\boldsymbol{q})}\Big)^{\frac{1}{2}}\big(\hat{c}^{\dagger}_{\lambda}(\boldsymbol{q})+\hat{c}_{\lambda}(-\boldsymbol{q})\big)\times\cdots\\
&\qquad\cdots\sum_{\langle u,u'\rangle}\Big[\boldsymbol{e}_{uu'}.\big(\boldsymbol{e}_{A,\lambda}(\boldsymbol{q})-\boldsymbol{e}_{B,\lambda}(\boldsymbol{q})e^{-i\boldsymbol{q}.(\boldsymbol{R}_{u'}-\boldsymbol{R}_u)}\big)e^{-i\boldsymbol{q}.\boldsymbol{R}_u}\times\cdots\\
&\qquad\cdots\frac{1}{N_u}\sum_{\boldsymbol{k},\boldsymbol{k}'}\big(\hat{d}^{\dagger}_{A}(\boldsymbol{k})\hat{d}_{B}(\boldsymbol{k}')e^{i(\boldsymbol{k}'.\boldsymbol{R}_{u'B}-\boldsymbol{k}.\boldsymbol{R}_{uA})}+\hat{d}^{\dagger}_{B}(\boldsymbol{k}')\hat{d}_{A}(\boldsymbol{k})e^{i(\boldsymbol{k}.\boldsymbol{R}_{uA}-\boldsymbol{k}'.\boldsymbol{R}_{u'B})}\big)\Big]\Bigg]\\
=& -g\sum_{\boldsymbol{q},\lambda}\sum_{\boldsymbol{k},\boldsymbol{k}'}\Bigg[\Big(\frac{\hbar}{2N_u m\omega_\lambda(\boldsymbol{q})}\Big)^{\frac{1}{2}}\big(\hat{c}^{\dagger}_{\lambda}(\boldsymbol{q})+\hat{c}_{\lambda}(-\boldsymbol{q})\big)\times\cdots\\
&\Big[\ \frac{1}{N_u}\sum_{\langle u,u'\rangle}\boldsymbol{e}_{uu'}.\big(\boldsymbol{e}_{A,\lambda}(\boldsymbol{q})-\boldsymbol{e}_{B,\lambda}(\boldsymbol{q})e^{-i\boldsymbol{q}.(\boldsymbol{R}_{u'}-\boldsymbol{R}_u)}\big)\,e^{-i\boldsymbol{q}.\boldsymbol{R}_u}e^{i(\boldsymbol{k}'.\boldsymbol{R}_{u'B}-\boldsymbol{k}.\boldsymbol{R}_{uA})}\ \hat{d}^{\dagger}_{A}(\boldsymbol{k})\hat{d}_{B}(\boldsymbol{k}')\\
&+\frac{1}{N_u}\sum_{\langle u,u'\rangle}\boldsymbol{e}_{uu'}.\big(\boldsymbol{e}_{A,\lambda}(\boldsymbol{q})-\boldsymbol{e}_{B,\lambda}(\boldsymbol{q})e^{-i\boldsymbol{q}.(\boldsymbol{R}_{u'}-\boldsymbol{R}_u)}\big)\,e^{-i\boldsymbol{q}.\boldsymbol{R}_u}e^{i(\boldsymbol{k}.\boldsymbol{R}_{uA}-\boldsymbol{k}'.\boldsymbol{R}_{u'B})}\ \hat{d}^{\dagger}_{B}(\boldsymbol{k}')\hat{d}_{A}(\boldsymbol{k})\Big]\Bigg].
\end{aligned}
\tag{4.19}
$$

Here, m is the mass of carbon atom. The first term in the second square bracket in the last equation is

$$\begin{aligned}
&\frac{1}{N_u}\sum_{\langle u,u'\rangle} \boldsymbol{e}_{uu'}.\left(\boldsymbol{e}_{A,\lambda}(\boldsymbol{q}) - \boldsymbol{e}_{B,\lambda}(\boldsymbol{q})e^{-i\boldsymbol{q}.(\boldsymbol{R}_{u'}-\boldsymbol{R}_u)}\right) e^{-i\boldsymbol{q}.\boldsymbol{R}_u} e^{i(\boldsymbol{k}'.\boldsymbol{R}_{u'B}-\boldsymbol{k}.\boldsymbol{R}_{uA})} \\
&= \frac{1}{N_u}\sum_{\langle u,u'\rangle} \boldsymbol{e}_{uu'}.\left(\boldsymbol{e}_{A,\lambda}(\boldsymbol{q}) - \boldsymbol{e}_{B,\lambda}(\boldsymbol{q})e^{-i\boldsymbol{q}.(\boldsymbol{R}_{u'}-\boldsymbol{R}_u)}\right) e^{i(\boldsymbol{k}'.\boldsymbol{d}_B-\boldsymbol{k}.\boldsymbol{d}_A)} e^{i\boldsymbol{k}'.(\boldsymbol{R}_{u'}-\boldsymbol{R}_u)} e^{i(\boldsymbol{k}'-\boldsymbol{q}-\boldsymbol{k}).\boldsymbol{R}_u} \\
&= \delta(\boldsymbol{k}+\boldsymbol{q},\boldsymbol{k}')\sum_{\langle 0,u'\rangle} \boldsymbol{e}_{0u'}.\left(\boldsymbol{e}_{A,\lambda}(\boldsymbol{q}) - \boldsymbol{e}_{B,\lambda}(\boldsymbol{q})e^{-i\boldsymbol{q}.(\boldsymbol{R}_{u'}-\boldsymbol{R}_0)}\right) e^{i(\boldsymbol{k}'.\boldsymbol{d}_B-\boldsymbol{k}.\boldsymbol{d}_A)} e^{i\boldsymbol{k}'.(\boldsymbol{R}_{u'}-\boldsymbol{R}_0)} \\
&= \delta(\boldsymbol{k}+\boldsymbol{q},\boldsymbol{k}') f_1(\boldsymbol{k},\boldsymbol{q}),
\end{aligned} \tag{4.20}$$

where we have defined

$$f_1(\boldsymbol{k},\boldsymbol{q}) = \sum_{\langle 0,u'\rangle} \boldsymbol{e}_{0u'}.\left(\boldsymbol{e}_{A,\lambda}(\boldsymbol{q})e^{-i\boldsymbol{q}.\boldsymbol{R}_0} - \boldsymbol{e}_{B,\lambda}(\boldsymbol{q})e^{-i\boldsymbol{q}.\boldsymbol{R}_{u'}}\right) e^{-i\boldsymbol{k}.\boldsymbol{R}_{0A}} e^{i(\boldsymbol{k}+\boldsymbol{q}).\boldsymbol{R}_{u'B}}. \tag{4.21}$$

Likewise, the second term in the square bracket of Eq. (4.19) is

$$\begin{aligned}
&\frac{1}{N_u}\sum_{\langle u,u'\rangle} \boldsymbol{e}_{uu'}.\left(\boldsymbol{e}_{A,\lambda}(\boldsymbol{q}) - \boldsymbol{e}_{B,\lambda}(\boldsymbol{q})e^{-i\boldsymbol{q}.(\boldsymbol{R}_{u'}-\boldsymbol{R}_u)}\right) e^{-i\boldsymbol{q}.\boldsymbol{R}_u} e^{i(\boldsymbol{k}.\boldsymbol{R}_{uA}-\boldsymbol{k}'.\boldsymbol{R}_{u'B})} \\
&= \frac{1}{N_u}\sum_{\langle u,u'\rangle} \boldsymbol{e}_{uu'}.\left(\boldsymbol{e}_{A,\lambda}(\boldsymbol{q}) - \boldsymbol{e}_{B,\lambda}(\boldsymbol{q})e^{-i\boldsymbol{q}.(\boldsymbol{R}_{u'}-\boldsymbol{R}_u)}\right) e^{i(\boldsymbol{k}.\boldsymbol{d}_A-\boldsymbol{k}'.\boldsymbol{d}_B)} e^{i\boldsymbol{k}'.(\boldsymbol{R}_u-\boldsymbol{R}_{u'})} e^{i(\boldsymbol{k}-\boldsymbol{q}-\boldsymbol{k}').\boldsymbol{R}_u} \\
&= \delta(\boldsymbol{k}-\boldsymbol{q},\boldsymbol{k}')\sum_{\langle 0,u'\rangle} \boldsymbol{e}_{0u'}.\left(\boldsymbol{e}_{A,\lambda}(\boldsymbol{q}) - \boldsymbol{e}_{B,\lambda}(\boldsymbol{q})e^{-i\boldsymbol{q}.(\boldsymbol{R}_{u'}-\boldsymbol{R}_0)}\right) e^{i(\boldsymbol{k}.\boldsymbol{d}_A-\boldsymbol{k}'.\boldsymbol{d}_B)} e^{i\boldsymbol{k}'.(\boldsymbol{R}_0-\boldsymbol{R}_{u'})} \\
&= \delta(\boldsymbol{k}-\boldsymbol{q},\boldsymbol{k}') f_2(\boldsymbol{k},\boldsymbol{q}),
\end{aligned} \tag{4.22}$$

where we have defined

$$f_2(\boldsymbol{k},\boldsymbol{q}) = \sum_{\langle 0,u'\rangle} \boldsymbol{e}_{0u'}.\left(\boldsymbol{e}_{A,\lambda}(\boldsymbol{q})e^{-i\boldsymbol{q}.\boldsymbol{R}_0} - \boldsymbol{e}_{B,\lambda}(\boldsymbol{q})e^{-i\boldsymbol{q}.\boldsymbol{R}_{u'}}\right) e^{i\boldsymbol{k}.\boldsymbol{R}_{0A}} e^{-i(\boldsymbol{k}-\boldsymbol{q}).\boldsymbol{R}_{u'B}}. \tag{4.23}$$

Therefore, the electron–phonon interaction Hamiltonian is

$$\begin{aligned}\hat{H}_{\text{el-ph}} =& -g\sum_{\boldsymbol{k},\boldsymbol{q},\lambda}\Bigg[\Big(\frac{\hbar}{2N_u m\omega_\lambda(\boldsymbol{q})}\Big)^{\frac{1}{2}}\big(\hat{c}^\dagger_\lambda(\boldsymbol{q})+\hat{c}_\lambda(-\boldsymbol{q})\big)\times\cdots \\ &\qquad\cdots\big(\hat{d}^\dagger_A(\boldsymbol{k})\hat{d}_B(\boldsymbol{k}+\boldsymbol{q})f_1(\boldsymbol{k},\boldsymbol{q})+\hat{d}^\dagger_B(\boldsymbol{k}-\boldsymbol{q})\hat{d}_A(\boldsymbol{k})f_2(\boldsymbol{k},\boldsymbol{q})\big)\Bigg] \\ =& -g\sum_{\boldsymbol{k},\boldsymbol{q},\lambda}\Bigg[\Big(\frac{\hbar}{2N_u m\omega_\lambda(\boldsymbol{q})}\Big)^{\frac{1}{2}}\big(\hat{c}^\dagger_\lambda(\boldsymbol{q})+\hat{c}_\lambda(-\boldsymbol{q})\big)\times\cdots \\ &\cdots\big(\hat{d}^\dagger_A(\boldsymbol{k})\hat{\tilde{d}}_B(\boldsymbol{k}+\boldsymbol{q})e^{-i\phi(\boldsymbol{k}+\boldsymbol{q})}f_1(\boldsymbol{k},\boldsymbol{q})+\hat{\tilde{d}}^\dagger_B(\boldsymbol{k}-\boldsymbol{q})\hat{d}_A(\boldsymbol{k})e^{i\phi(\boldsymbol{k}-\boldsymbol{q})}f_2(\boldsymbol{k},\boldsymbol{q})\big)\Bigg].\end{aligned} \tag{4.24}$$

We note that $\phi(\boldsymbol{k})$ is the phase of function $f(\boldsymbol{k})$ defined in Eq. (4.10). Now, we define the following functions

$$\tilde{f}_1(\boldsymbol{k},\boldsymbol{q})=e^{-i\phi(\boldsymbol{k}+\boldsymbol{q})}f_1(\boldsymbol{k},\boldsymbol{q}) \quad , \quad \tilde{f}_2(\boldsymbol{k},\boldsymbol{q})=e^{i\phi(\boldsymbol{k}-\boldsymbol{q})}f_2(\boldsymbol{k},\boldsymbol{q}). \tag{4.25}$$

Substituting $\hat{d}_A(\boldsymbol{k})$ and $\hat{\tilde{d}}_B(\boldsymbol{k})$ with $\hat{u}(\boldsymbol{k})$ and $\hat{v}(\boldsymbol{k})$ operators gives the final form of the electron–phonon interaction Hamiltonian

$$\begin{aligned}\hat{H}_{\text{el-ph}} =& -g\sum_{\boldsymbol{k},\boldsymbol{q},\lambda}\Big(\frac{\hbar}{2N_u m\omega_\lambda(\boldsymbol{q})}\Big)^{\frac{1}{2}}\big(\hat{c}^\dagger_\lambda(\boldsymbol{q})+\hat{c}_\lambda(-\boldsymbol{q})\big)\times\cdots \\ &\cdots\Bigg[\frac{\tilde{f}_1(\boldsymbol{k}-\boldsymbol{q},\boldsymbol{q})+\tilde{f}_2(\boldsymbol{k},\boldsymbol{q})}{2}\Big(\hat{u}^\dagger(\boldsymbol{k}-\boldsymbol{q})\hat{u}(\boldsymbol{k})-\hat{v}^\dagger(\boldsymbol{k}-\boldsymbol{q})\hat{v}(\boldsymbol{k})\Big) \\ &\quad-\frac{\tilde{f}_1(\boldsymbol{k}-\boldsymbol{q},\boldsymbol{q})-\tilde{f}_2(\boldsymbol{k},\boldsymbol{q})}{2}\Big(\hat{u}^\dagger(\boldsymbol{k}-\boldsymbol{q})\hat{v}(\boldsymbol{k})-\hat{v}^\dagger(\boldsymbol{k}-\boldsymbol{q})\hat{u}(\boldsymbol{k})\Big)\Bigg].\end{aligned} \tag{4.26}$$

Introducing the following factors

$$\begin{aligned}g_{\text{intra}}(\lambda,\boldsymbol{q},\boldsymbol{k}) &= -g\left(\frac{\hbar}{2N_u m\omega_\lambda(\boldsymbol{q})}\right)^{\frac{1}{2}}\frac{\tilde{f}_1(\boldsymbol{k}-\boldsymbol{q},\boldsymbol{q})+\tilde{f}_2(\boldsymbol{k},\boldsymbol{q})}{2}, \\ g_{\text{inter}}(\lambda,\boldsymbol{q},\boldsymbol{k}) &= -g\left(\frac{\hbar}{2N_u m\omega_\lambda(\boldsymbol{q})}\right)^{\frac{1}{2}}\frac{\tilde{f}_1(\boldsymbol{k}-\boldsymbol{q},\boldsymbol{q})-\tilde{f}_2(\boldsymbol{k},\boldsymbol{q})}{2}.\end{aligned} \tag{4.27}$$

We can write the electron–phonon interaction Hamiltonian in a more compact notation

$$\begin{aligned}\hat{H}_{\text{el-ph}} = &+\sum_{\boldsymbol{k},\boldsymbol{q},\lambda} g_{\text{intra}}(\lambda,\boldsymbol{q},\boldsymbol{k})\ \hat{u}^{\dagger}(\boldsymbol{k}-\boldsymbol{q})\ \hat{u}(\boldsymbol{k})\left(\hat{c}^{\dagger}_{\lambda}(\boldsymbol{q})+\hat{c}_{\lambda}(-\boldsymbol{q})\right)\\ &-\sum_{\boldsymbol{k},\boldsymbol{q},\lambda} g_{\text{intra}}(\lambda,\boldsymbol{q},\boldsymbol{k})\ \hat{v}^{\dagger}(\boldsymbol{k}-\boldsymbol{q})\ \hat{v}(\boldsymbol{k})\left(\hat{c}^{\dagger}_{\lambda}(\boldsymbol{q})+\hat{c}_{\lambda}(-\boldsymbol{q})\right)\\ &-\sum_{\boldsymbol{k},\boldsymbol{q},\lambda} g_{\text{inter}}(\lambda,\boldsymbol{q},\boldsymbol{k})\ \hat{u}^{\dagger}(\boldsymbol{k}-\boldsymbol{q})\ \hat{v}(\boldsymbol{k})\left(\hat{c}^{\dagger}_{\lambda}(\boldsymbol{q})+\hat{c}_{\lambda}(-\boldsymbol{q})\right)\\ &+\sum_{\boldsymbol{k},\boldsymbol{q},\lambda} g_{\text{inter}}(\lambda,\boldsymbol{q},\boldsymbol{k})\ \hat{v}^{\dagger}(\boldsymbol{k}-\boldsymbol{q})\ \hat{u}(\boldsymbol{k})\left(\hat{c}^{\dagger}_{\lambda}(\boldsymbol{q})+\hat{c}_{\lambda}(-\boldsymbol{q})\right),\end{aligned} \tag{4.28}$$

where the first two lines yield the intraband electron scattering and the last two lines yield the interband electron scattering via phonons. Here, the interaction Hamiltonian is Hermitian because we have

$$g(\lambda,\boldsymbol{q},\boldsymbol{k}) = g^{*}(\lambda,-\boldsymbol{q},\boldsymbol{k}-\boldsymbol{q}). \tag{4.29}$$

4.4 Electron–phonon scattering rates in CNTs

According to Fermi's Golden Rule, the transition rate from a quasiparticle state $|c,\boldsymbol{k}\rangle = \hat{u}^{\dagger}(\boldsymbol{k})|\text{GS}\rangle$ into a quasiparticle state $|c,\boldsymbol{k}-\boldsymbol{q}\rangle = \hat{u}^{\dagger}(\boldsymbol{k}-\boldsymbol{q})|\text{GS}\rangle$ is

$$\begin{aligned}S(\boldsymbol{k},\boldsymbol{k}-\boldsymbol{q}) =& \frac{2\pi}{\hbar}\sum_{\lambda}\left(n_{\lambda}(\pm\boldsymbol{q})+\tfrac{1}{2}\pm\tfrac{1}{2}\right)\left|g_{\text{intra}}(\lambda,\boldsymbol{q},\boldsymbol{k})\right|^{2}\delta\big(E_c(\boldsymbol{k}-\boldsymbol{q})-E_c(\boldsymbol{k})\pm\hbar\omega_{\lambda}(\pm\boldsymbol{q})\big)\\ =& \frac{g^2\pi}{4N_u m}\sum_{\lambda}\left[\frac{n_{\lambda}(\pm\boldsymbol{q})+\frac{1}{2}\pm\frac{1}{2}}{\omega_{\lambda}(\boldsymbol{q})}\left|\tilde{f}_1(\boldsymbol{k}-\boldsymbol{q},\boldsymbol{q})+\tilde{f}_2(\boldsymbol{k},\boldsymbol{q})\right|^{2}\times\cdots\right.\\ &\left.\cdots\delta\big(E_c(\boldsymbol{k}-\boldsymbol{q})-E_c(\boldsymbol{k})\pm\hbar\omega_{\lambda}(\pm\boldsymbol{q})\big)\right]\end{aligned} \tag{4.30}$$

Here, the plus sign represents emission of a phonon with wave vector $\boldsymbol{q}$ and the minus sign represents absorption of a phonon with wave vector $-\boldsymbol{q}$.

Therefore, the scattering rate out of state $|c,\boldsymbol{k}\rangle$ is

$$\begin{aligned}\Gamma(\boldsymbol{k}) =& \sum_{\boldsymbol{q}} S(\boldsymbol{k},\boldsymbol{k}-\boldsymbol{q}) \\ =& \frac{g^2\pi}{4N_u m}\sum_{\lambda,\boldsymbol{q}}\left[\frac{n_\lambda(\pm\boldsymbol{q})+\frac{1}{2}\pm\frac{1}{2}}{\omega_\lambda(\boldsymbol{q})}\left|\tilde{f}_1(\boldsymbol{k}-\boldsymbol{q},\boldsymbol{q})+\tilde{f}_2(\boldsymbol{k},\boldsymbol{q})\right|^2\times\cdots\right. \\ &\left.\cdots\delta\big(E_c(\boldsymbol{k}-\boldsymbol{q})-E_c(\boldsymbol{k})\pm\hbar\omega_\lambda(\pm\boldsymbol{q})\big)\right] \qquad (4.31)\\ =& \frac{g^2\pi}{4N_u m}\sum_{\lambda,\mu}\frac{1}{\Delta q}\int dq\left[\frac{n_\lambda(\pm\boldsymbol{q})+\frac{1}{2}\pm\frac{1}{2}}{\omega_\lambda(\boldsymbol{q})}\times\cdots\right. \\ &\left.\cdots\left|\tilde{f}_1(\boldsymbol{k}-\boldsymbol{q},\boldsymbol{q})+\tilde{f}_2(\boldsymbol{k},\boldsymbol{q})\right|^2\delta\big(E_c(\boldsymbol{k}-\boldsymbol{q})-E_c(\boldsymbol{k})\pm\hbar\omega_\lambda(\pm\boldsymbol{q})\big)\right].\end{aligned}$$

For a carbon nanotube of length L and radius r, the total number of graphene unit cells is

$$N_u = \frac{2\pi r L}{A_u}, \qquad (4.32)$$

where A_u is the graphene unit-cell area. We also have $\Delta q = \frac{2\pi}{L}$. Therefore, the scattering rate is

$$\begin{aligned}\Gamma(\boldsymbol{k}) =& \frac{g^2 A_u}{16\,\pi\,m\,r}\sum_{\lambda,\mu}\int dq\left[\frac{n_\lambda(\pm\boldsymbol{q})+\frac{1}{2}\pm\frac{1}{2}}{\omega_\lambda(\boldsymbol{q})}\times\cdots\right. \\ &\left.\cdots\left|\tilde{f}_1(\boldsymbol{k}-\boldsymbol{q},\boldsymbol{q})+\tilde{f}_2(\boldsymbol{k},\boldsymbol{q})\right|^2\delta\big(E_c(\boldsymbol{k}-\boldsymbol{q})-E_c(\boldsymbol{k})\pm\hbar\omega_\lambda(\pm\boldsymbol{q})\big)\right] \qquad (4.33)\\ =& \frac{g^2 A_u}{16\,\pi\,m\,r}\sum_{\lambda,\mu}\frac{\left(n_\lambda(\pm\boldsymbol{q}_0)+\frac{1}{2}\pm\frac{1}{2}\right)\left|\tilde{f}_1(\boldsymbol{k}-\boldsymbol{q}_0,\boldsymbol{q}_0)+\tilde{f}_2(\boldsymbol{k},\boldsymbol{q}_0)\right|^2}{\omega_\lambda(\boldsymbol{q}_0)\left|-E_c'(\boldsymbol{k}-\boldsymbol{q}_0)+\hbar\omega_\lambda'(\pm\boldsymbol{q}_0)\right|}.\end{aligned}$$

4.5 Exciton–phonon Interaction Hamiltonian

The creation and annihilation operators of single excitonic states are written as

$$\begin{aligned}\hat{B}_s^\dagger(\boldsymbol{K}) &= \sum_{\boldsymbol{k}_r} A_s(\boldsymbol{K},\boldsymbol{k}_r)\;\hat{u}^\dagger(\boldsymbol{k}_r+\boldsymbol{K})\;\hat{v}(\boldsymbol{k}_r-\boldsymbol{K}),\\ \hat{B}_s(\boldsymbol{K}) &= \sum_{\boldsymbol{k}_r} A_s^*(\boldsymbol{K},\boldsymbol{k}_r)\;\hat{v}^\dagger(\boldsymbol{k}_r-\boldsymbol{K})\;\hat{u}(\boldsymbol{k}_r+\boldsymbol{K}).\end{aligned} \qquad (4.34)$$

Here, s is the discrete excitonic state quantum number, $\boldsymbol{K}$ is the exciton center-of-mass wave number, $\boldsymbol{k}_r$ is the wave number associated with the relative position.

In the space of single-excitation states (i.e., $|\boldsymbol{K}, s\rangle = \hat{B}_s^\dagger(\boldsymbol{K})|\mathrm{GS}\rangle$), the exciton–phonon interaction Hamiltonian is written as

$$\hat{H}_{\text{ex-ph}} = \sum_{\boldsymbol{K},s} \sum_{\boldsymbol{K}',s'} \langle \boldsymbol{K}', s'|\hat{H}_{\text{el-ph}}|\boldsymbol{K}, s\rangle \hat{B}_{s'}^\dagger(\boldsymbol{K}')\hat{B}_s(\boldsymbol{K}). \tag{4.35}$$

Using Eq. (4.28), the matrix element in the equation above becomes

$$\begin{aligned}\langle \boldsymbol{K} - \tfrac{\boldsymbol{q}}{2}, s'|\hat{H}_{\text{ep}}|\boldsymbol{K}, s\rangle = \Bigg[&\sum_{\boldsymbol{k}_r,\lambda} A_{s'}^*(\boldsymbol{K} - \tfrac{\boldsymbol{q}}{2}, \boldsymbol{k}_r - \tfrac{\boldsymbol{q}}{2}) A_s(\boldsymbol{K}, \boldsymbol{k}_r)\; g_{\text{intra}}(\lambda, \boldsymbol{q}, \boldsymbol{k}_r + \boldsymbol{K}) \\ &+ \sum_{\boldsymbol{k}_r,\lambda} A_{s'}^*(\boldsymbol{K} - \tfrac{\boldsymbol{q}}{2}, \boldsymbol{k}_r + \tfrac{\boldsymbol{q}}{2}) A_s(\boldsymbol{K}, \boldsymbol{k}_r)\; g_{\text{intra}}(\lambda, \boldsymbol{q}, \boldsymbol{k}_r - \boldsymbol{K} + \boldsymbol{q}) \Bigg] \Big(\hat{c}_\lambda^\dagger(\boldsymbol{q}) + \hat{c}_\lambda(-\boldsymbol{q})\Big).\end{aligned} \tag{4.36}$$

Here, the first term in the square bracket accounts for intraband electron scattering and the second term accounts for intraband hole scattering. Interband electron–phonon interaction does not play a role here, since it would result in exciton creation or annihilation (would not conserve exciton number).

Therefore, the exciton–phonon interaction Hamiltonian can be written in the following form

$$\hat{H}_{\text{ex-ph}} = \sum_{s,s'} \sum_{\lambda} \sum_{\boldsymbol{K},\boldsymbol{q}} g_{s,s'}(\lambda, \boldsymbol{q}, \boldsymbol{K})\, \hat{B}_{s'}^\dagger(\boldsymbol{K} - \tfrac{\boldsymbol{q}}{2})\, \hat{B}_s(\boldsymbol{K}) \left(\hat{c}_\lambda^\dagger(\boldsymbol{q}) + \hat{c}_\lambda(-\boldsymbol{q})\right), \tag{4.37}$$

where

$$\begin{aligned} g_{s,s'}(\lambda, \boldsymbol{q}, \boldsymbol{K}) = \quad &\sum_{\boldsymbol{k}_r} A_{s'}^*(\boldsymbol{K} - \tfrac{\boldsymbol{q}}{2}, \boldsymbol{k}_r - \tfrac{\boldsymbol{q}}{2}) A_s(\boldsymbol{K}, \boldsymbol{k}_r)\; g_{\text{intra}}(\lambda, \boldsymbol{q}, \boldsymbol{k}_r + \boldsymbol{K}) \\ &+ \sum_{\boldsymbol{k}_r} A_{s'}^*(\boldsymbol{K} - \tfrac{\boldsymbol{q}}{2}, \boldsymbol{k}_r + \tfrac{\boldsymbol{q}}{2}) A_s(\boldsymbol{K}, \boldsymbol{k}_r)\; g_{\text{intra}}(\lambda, \boldsymbol{q}, \boldsymbol{k}_r - \boldsymbol{K} + \boldsymbol{q}). \end{aligned} \tag{4.38}$$

4.6 Exciton–phonon scattering rates in CNTs

According to Fermi's Golden Rule, the exciton transition rate due to phonon emission and absorption from an initial state $|\boldsymbol{K}, s\rangle = \hat{B}_s^\dagger(\boldsymbol{K})|\mathrm{GS}\rangle$ into a final state $|\boldsymbol{K} - \frac{\boldsymbol{q}}{2}, s'\rangle =$

$\hat{B}^{\dagger}_{s'}(\boldsymbol{K}-\frac{\boldsymbol{q}}{2})|\mathrm{GS}\rangle$ is

$$
\begin{aligned}
S(s,\boldsymbol{K};s',\boldsymbol{K}-\tfrac{\boldsymbol{q}}{2}) &= \frac{2\pi}{\hbar}\sum_{\lambda}\left(n_{\lambda}(\pm\boldsymbol{q})+\tfrac{1}{2}\pm\tfrac{1}{2}\right)\left|g_{s,s'}(\lambda,\boldsymbol{q},\boldsymbol{K})\right|^2\times\cdots \\
&\qquad\qquad \cdots\delta\big(\Omega_s(\boldsymbol{K})-\Omega_{s'}(\boldsymbol{K}-\tfrac{\boldsymbol{q}}{2})-\hbar\omega_{\lambda}(\boldsymbol{q})\big) \\
&= \frac{2\pi}{\hbar}\sum_{\lambda}\left(n_{\lambda}(\pm\boldsymbol{q})+\tfrac{1}{2}\pm\tfrac{1}{2}\right)\delta\big(\Omega_s(\boldsymbol{K})-\Omega_{s'}(\boldsymbol{K}-\tfrac{\boldsymbol{q}}{2})\mp\hbar\omega_{\lambda}(\pm\boldsymbol{q})\big)\times\cdots \\
&\qquad \cdots\Bigg|\sum_{\boldsymbol{k}_r}A^{*}_{s'}(\boldsymbol{K}-\tfrac{\boldsymbol{q}}{2},\boldsymbol{k}_r-\tfrac{\boldsymbol{q}}{2})A_s(\boldsymbol{K},\boldsymbol{k}_r)\;g_{\mathrm{intra}}(\lambda,\boldsymbol{q},\boldsymbol{k}_r+\boldsymbol{K}) \\
&\qquad\qquad +\sum_{\boldsymbol{k}_r}A^{*}_{s'}(\boldsymbol{K}-\tfrac{\boldsymbol{q}}{2},\boldsymbol{k}_r+\tfrac{\boldsymbol{q}}{2})A_s(\boldsymbol{K},\boldsymbol{k}_r)\;g_{\mathrm{intra}}(\lambda,\boldsymbol{q},\boldsymbol{k}_r-\boldsymbol{K}+\boldsymbol{q})\Bigg|^2 \\
&= \frac{g^2\pi}{4N_u m}\sum_{\lambda}\frac{n_{\lambda}(\pm\boldsymbol{q})+\frac{1}{2}\pm\frac{1}{2}}{\omega_{\lambda}(\boldsymbol{q})}\;\delta\big(\Omega_s(\boldsymbol{K})-\Omega_{s'}(\boldsymbol{K}-\tfrac{\boldsymbol{q}}{2})\mp\hbar\omega_{\lambda}(\pm\boldsymbol{q})\big)\times\cdots \\
&\quad \cdots\Bigg|\sum_{\boldsymbol{k}_r}A^{*}_{s'}(\boldsymbol{K}-\tfrac{\boldsymbol{q}}{2},\boldsymbol{k}_r-\tfrac{\boldsymbol{q}}{2})A_s(\boldsymbol{K},\boldsymbol{k}_r)\;\left(\tilde{f}_{1,\lambda}(\boldsymbol{k}_r+\boldsymbol{K}-\boldsymbol{q},\boldsymbol{q})+\tilde{f}_{2,\lambda}(\boldsymbol{k}_r+\boldsymbol{K},\boldsymbol{q})\right) \\
&\qquad +\sum_{\boldsymbol{k}_r}A^{*}_{s'}(\boldsymbol{K}-\tfrac{\boldsymbol{q}}{2},\boldsymbol{k}_r+\tfrac{\boldsymbol{q}}{2})A_s(\boldsymbol{K},\boldsymbol{k}_r)\;\left(\tilde{f}_{1,\lambda}(\boldsymbol{k}_r-\boldsymbol{K},\boldsymbol{q})+\tilde{f}_{2,\lambda}(\boldsymbol{k}_r-\boldsymbol{K}+\boldsymbol{q},\boldsymbol{q})\right)\Bigg|^2
\end{aligned}
\tag{4.39}
$$

Here, the upper sign corresponds to phonon emission and the lower sign corresponds to phonon absorption.

Therefore, the scattering rate out of state $|s, \boldsymbol{K}\rangle$ is

$$
\begin{aligned}
\Gamma(s,\boldsymbol{K}) &= \sum_{\boldsymbol{q}} S(s,\boldsymbol{K};s',\boldsymbol{K}-\tfrac{\boldsymbol{q}}{2}) \\
&= \frac{g^2\pi}{4N_u m}\sum_{\lambda,\boldsymbol{q}} \frac{n_\lambda(\pm\boldsymbol{q})+\frac{1}{2}\pm\frac{1}{2}}{\omega_\lambda(\boldsymbol{q})}\,\delta\Big(\Omega_s(\boldsymbol{K})-\Omega_{s'}(\boldsymbol{K}-\tfrac{\boldsymbol{q}}{2})\mp\hbar\omega_\lambda(\pm\boldsymbol{q})\Big)\times\cdots \\
&\quad \cdots\Bigg|\sum_{\boldsymbol{k}_r} A^*_{s'}(\boldsymbol{K}-\tfrac{\boldsymbol{q}}{2},\boldsymbol{k}_r-\tfrac{\boldsymbol{q}}{2})A_s(\boldsymbol{K},\boldsymbol{k}_r)\,\big(\tilde{f}_{1,\lambda}(\boldsymbol{k}_r+\boldsymbol{K}-\boldsymbol{q},\boldsymbol{q})+\tilde{f}_{2,\lambda}(\boldsymbol{k}_r+\boldsymbol{K},\boldsymbol{q})\big) \\
&\qquad +\sum_{\boldsymbol{k}_r} A^*_{s'}(\boldsymbol{K}-\tfrac{\boldsymbol{q}}{2},\boldsymbol{k}_r+\tfrac{\boldsymbol{q}}{2})A_s(\boldsymbol{K},\boldsymbol{k}_r)\,\big(\tilde{f}_{1,\lambda}(\boldsymbol{k}_r-\boldsymbol{K},\boldsymbol{q})+\tilde{f}_{2,\lambda}(\boldsymbol{k}_r-\boldsymbol{K}+\boldsymbol{q},\boldsymbol{q})\big)\Bigg|^2 \\
&= \frac{g^2\pi}{4N_u m}\sum_{\lambda,\mu} \frac{1}{\Delta q}\int dq\,\frac{n_\lambda(\pm\boldsymbol{q})+\frac{1}{2}\pm\frac{1}{2}}{\omega_\lambda(\boldsymbol{q})}\,\delta\Big(\Omega_s(\boldsymbol{K})-\Omega_{s'}(\boldsymbol{K}-\tfrac{\boldsymbol{q}}{2})\mp\hbar\omega_\lambda(\pm\boldsymbol{q})\Big)\times\cdots \\
&\quad \cdots\Bigg|\sum_{\boldsymbol{k}_r} A^*_{s'}(\boldsymbol{K}-\tfrac{\boldsymbol{q}}{2},\boldsymbol{k}_r-\tfrac{\boldsymbol{q}}{2})A_s(\boldsymbol{K},\boldsymbol{k}_r)\,\big(\tilde{f}_{1,\lambda}(\boldsymbol{k}_r+\boldsymbol{K}-\boldsymbol{q},\boldsymbol{q})+\tilde{f}_{2,\lambda}(\boldsymbol{k}_r+\boldsymbol{K},\boldsymbol{q})\big) \\
&\qquad +\sum_{\boldsymbol{k}_r} A^*_{s'}(\boldsymbol{K}-\tfrac{\boldsymbol{q}}{2},\boldsymbol{k}_r+\tfrac{\boldsymbol{q}}{2})A_s(\boldsymbol{K},\boldsymbol{k}_r)\,\big(\tilde{f}_{1,\lambda}(\boldsymbol{k}_r-\boldsymbol{K},\boldsymbol{q})+\tilde{f}_{2,\lambda}(\boldsymbol{k}_r-\boldsymbol{K}+\boldsymbol{q},\boldsymbol{q})\big)\Bigg|^2 .
\end{aligned}
\tag{4.40}
$$

For a carbon nanotube of length L and radius r, the total number of graphene unit cells is

$$
N_u = \frac{2\pi r L}{A_u}, \tag{4.41}
$$

where A_u is the graphene unit-cell area. We also have $\Delta q = \frac{2\pi}{L}$. Therefore, the scattering rate is

$$\begin{aligned}
\Gamma(s,\boldsymbol{K}) = \frac{g^2 A_u}{16\pi m r}\sum_{\lambda,\mu}\int dq\ \frac{n_\lambda(\pm\boldsymbol{q})+\frac{1}{2}\pm\frac{1}{2}}{\omega_\lambda(\boldsymbol{q})}\ \delta\Big(\Omega_s(\boldsymbol{K})-\Omega_{s'}(\boldsymbol{K}-\tfrac{\boldsymbol{q}}{2})\mp\hbar\omega_\lambda(\pm\boldsymbol{q})\Big)\times\cdots \\
\cdots\Bigg|\ \sum_{\boldsymbol{k}_r} A^*_{s'}(\boldsymbol{K}-\tfrac{\boldsymbol{q}}{2},\boldsymbol{k}_r-\tfrac{\boldsymbol{q}}{2})A_s(\boldsymbol{K},\boldsymbol{k}_r)\ \big(\tilde{f}_{1,\lambda}(\boldsymbol{k}_r+\boldsymbol{K}-\boldsymbol{q},\boldsymbol{q})+\tilde{f}_{2,\lambda}(\boldsymbol{k}_r+\boldsymbol{K},\boldsymbol{q})\big) \\
+\sum_{\boldsymbol{k}_r} A^*_{s'}(\boldsymbol{K}-\tfrac{\boldsymbol{q}}{2},\boldsymbol{k}_r+\tfrac{\boldsymbol{q}}{2})A_s(\boldsymbol{K},\boldsymbol{k}_r)\ \big(\tilde{f}_{1,\lambda}(\boldsymbol{k}_r-\boldsymbol{K},\boldsymbol{q})+\tilde{f}_{2,\lambda}(\boldsymbol{k}_r-\boldsymbol{K}+\boldsymbol{q},\boldsymbol{q})\big)\Bigg|^2 \\
= \frac{g^2 A_u}{16\pi m r}\sum_{\lambda,\mu}\frac{n_\lambda(\pm\boldsymbol{q}_0)+\frac{1}{2}\pm\frac{1}{2}}{\omega_\lambda(\boldsymbol{q}_0)\left|\frac{1}{2}\Omega'_{s'}(\boldsymbol{K}-\frac{\boldsymbol{q}_0}{2})-\hbar\omega'_\lambda(\pm\boldsymbol{q}_0)\right|}\times\cdots \\
\cdots\Bigg|\ \sum_{\boldsymbol{k}_r} A^*_{s'}(\boldsymbol{K}-\tfrac{\boldsymbol{q}_0}{2},\boldsymbol{k}_r-\tfrac{\boldsymbol{q}_0}{2})A_s(\boldsymbol{K},\boldsymbol{k}_r)\ \big(\tilde{f}_{1,\lambda}(\boldsymbol{k}_r+\boldsymbol{K}-\boldsymbol{q}_0,\boldsymbol{q}_0)+\tilde{f}_{2,\lambda}(\boldsymbol{k}_r+\boldsymbol{K},\boldsymbol{q}_0)\big) \\
+\sum_{\boldsymbol{k}_r} A^*_{s'}(\boldsymbol{K}-\tfrac{\boldsymbol{q}_0}{2},\boldsymbol{k}_r+\tfrac{\boldsymbol{q}_0}{2})A_s(\boldsymbol{K},\boldsymbol{k}_r)\ \big(\tilde{f}_{1,\lambda}(\boldsymbol{k}_r-\boldsymbol{K},\boldsymbol{q}_0)+\tilde{f}_{2,\lambda}(\boldsymbol{k}_r-\boldsymbol{K}+\boldsymbol{q}_0,\boldsymbol{q}_0)\big)\Bigg|^2 .
\end{aligned} \tag{4.42}$$

In the last equation, $\boldsymbol{q}_0$ represents the states that conserve both momentum and energy:

$$\Omega_{s'}(\boldsymbol{K}-\tfrac{\boldsymbol{q}_0}{2}) = \Omega_s(\boldsymbol{K})\mp\hbar\omega_\lambda(\pm\boldsymbol{q}_0). \tag{4.43}$$

Here, $\Omega_s(\boldsymbol{K})$ is the exciton energy. Figure 4.1 shows the calculated exciton–phonon scattering rates in a (10,0) carbon nanotube due to phonon emission. As we can see, the scattering rate between A_1 and A_2 excitons are almost zero because of their different symmetries.

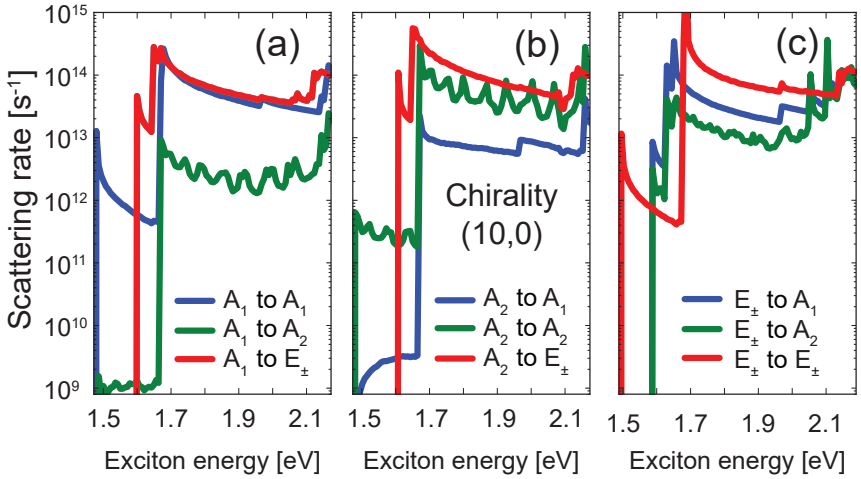

Figure 4.1: Exciton–phonon scattering rates in a (10,0) carbon nanotube due to phonon emission.

Chapter 5

Phonon-assisted Nonresonant Exciton Transfer

In this Chapter, we use the Coulomb-coupling Hamiltonian and the exciton–phonon interaction Hamiltonian in the context of second-order Fermi's Golden Rule to calculate the phonon-assisted exciton transfer rate. We show the results of the calculation for exciton transfer among bright excitonic state and between bright and dark excitonic states in pairs of perpendicular and parallel CNTs with various chiralities.

5.1 Theory of non-resonant exciton transfer

According to second-order Fermi's Golden Rule, the transition amplitude between excitonic states is [73]

$$S\big(i,f\big) = \frac{2\pi}{\hbar}\left|\sum_{m}\frac{\langle f|\hat{V}|m\rangle\langle m|\hat{V}|i\rangle}{E_i - E_m}\right|^2 \times \delta\big(E_i - E_f\big), \tag{5.1}$$

where $|i\rangle$, $|m\rangle$, and $|f\rangle$ are the initial, transition, and final quantum states, respectively. Also, $\hat{V}$ is the perturbation Hamiltonian. In the second-order scattering process, the quantum system momentarily jumps into a transition state, which does not have to obey energy conservation and then jumps to the final quantum state, which obeys the energy conservation (See Fig. 5.1). We should note that the expression for the second-order transition rate is valid in cases where the energy difference $\Delta E = E_i - E_m$ is not zero for any choice of transition state $|m\rangle$. However, when we are dealing with a continuum of energy levels, the energy

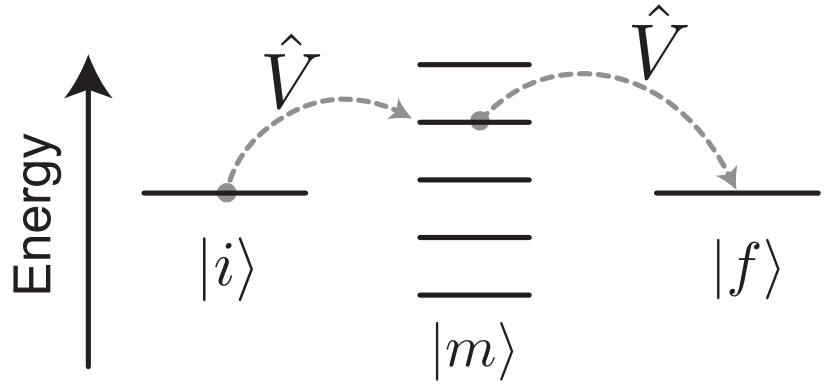

Figure 5.1: Schematic of a second-order process. The quantum system momentarily jumps into a transiton (intermediate) quantum state $|m\rangle$, which does not have to conserve energy.

difference could be zero for some transition states. In these cases, one needs to account for inescapable level broadening and use $\Delta E = E_i - E_m + i\gamma_i$ in the denominator of Eq. (5.1), where γ_i is the level broadening of the initial state $|i\rangle$ [72, 74, 75, 76].

In the problem of exciton transfer in carbon nanotubes, the perturbation Hamiltonian is

$$\hat{V} = \hat{H}_{\text{coul}} + \hat{H}_{\text{ex-ph},1} + \hat{H}_{\text{ex-ph},2}, \tag{5.2}$$

where $\hat{H}_{\text{coul}}$ is the Hamiltonian of Coulomb coupling between electrons of donor and acceptor CNTs, and $\hat{H}_{\text{ex-ph},n}$ is the interaction Hamiltonian between excitons and phonons in the n-th carbon nanotube

$$\hat{H}_{\text{ex-ph},n} = \sum_{s,s'} \sum_{\lambda} \sum_{\boldsymbol{K},\boldsymbol{q}} g_{nss'}(\lambda, \boldsymbol{q}, \boldsymbol{K}) \big(c^{\dagger}_{n,\lambda}(\boldsymbol{q}) + c_{n,\lambda}(-\boldsymbol{q})\big) \; |n, s', \boldsymbol{K} - \tfrac{\boldsymbol{q}}{2}\rangle\langle n, s, \boldsymbol{K}|, \tag{5.3}$$

$$\hat{H}_{\text{coul}} = \sum_{\boldsymbol{K},s} \sum_{\boldsymbol{K}',s'} M(\boldsymbol{K}, s; \boldsymbol{K}', s') \; |2, s', \boldsymbol{K}'\rangle\langle 1, s, \boldsymbol{K}| + \text{h.c.}. \tag{5.4}$$

The relevant matrix elements are derived in Sections 4.5 and 3.2.

We note that the initial, transition (intermediate), and final states of the system consist of electronic and phononic parts:

$$|i\rangle = |i^{\text{e}}\rangle \otimes |i^{\text{ph}}\rangle, \quad |m\rangle = |m^{\text{e}}\rangle \otimes |m^{\text{ph}}\rangle, \quad |f\rangle = |f^{\text{e}}\rangle \otimes |f^{\text{ph}}\rangle. \tag{5.5}$$

Therefore, the second-order transition amplitude is

$$S(i,f) = \frac{2\pi}{\hbar}\left|\sum_{|m^{\mathrm{e}}\rangle}\sum_{|m^{\mathrm{ph}}\rangle}\frac{\langle f^{\mathrm{e}}|\otimes\langle f^{\mathrm{ph}}|V|m^{\mathrm{e}}\rangle\otimes|m^{\mathrm{ph}}\rangle \quad \langle m^{\mathrm{e}}|\otimes\langle m^{\mathrm{ph}}|V|i^{\mathrm{e}}\rangle\otimes|i^{\mathrm{ph}}\rangle}{E_i^{\mathrm{e}}+E_i^{\mathrm{ph}}-E_m^{\mathrm{e}}-E_m^{\mathrm{ph}}}\right|^2 \times \cdots$$

$$\cdots\delta\big(E_i^{\mathrm{e}}+E_i^{\mathrm{ph}}-E_f^{\mathrm{e}}-E_f^{\mathrm{ph}}\big)$$

$$= \frac{2\pi}{\hbar}\left|\sum_{|m^{\mathrm{e}}\rangle}\sum_{|m^{\mathrm{ph}}\rangle}\frac{\langle f^{\mathrm{e}}|\otimes\langle f^{\mathrm{ph}}|V|m^{\mathrm{e}}\rangle\otimes|m^{\mathrm{ph}}\rangle \quad \langle m^{\mathrm{e}}|\otimes\langle m^{\mathrm{ph}}|V|i^{\mathrm{e}}\rangle\otimes|i^{\mathrm{ph}}\rangle}{\Delta E_{im}^{\mathrm{e}}+\Delta E_{im}^{\mathrm{ph}}}\right|^2 \times \cdots$$

$$\cdots\delta\big(\Delta E_{if}^{\mathrm{e}}+\Delta E_{if}^{\mathrm{ph}}\big). \tag{5.6}$$

We take the electronic part of the initial and final states to be single exciton states

$$|i^{\mathrm{e}}\rangle = |1,s_1,\boldsymbol{K}_1\rangle = B_{1s_1}^{\dagger}(\boldsymbol{K}_2)|\mathrm{GS}\rangle \quad \text{and} \quad |f^{\mathrm{e}}\rangle = |2,s_2,\boldsymbol{K}_2\rangle = B_{2s_2}^{\dagger}(\boldsymbol{K}_2)|\mathrm{GS}\rangle. \tag{5.7}$$

The phononic part of the final state is the same of phononic part of the initial state with one phonon created or annihilated

$$|f^{\mathrm{ph}}\rangle = |i^{\mathrm{ph}}+(n,\lambda,\boldsymbol{q})\rangle = c_{n\lambda}^{\dagger}(\boldsymbol{q})|i^{\mathrm{ph}}\rangle \quad \text{or} \quad |f^{\mathrm{ph}}\rangle = |i^{\mathrm{ph}}-(n,\lambda,\boldsymbol{q})\rangle = c_{n\lambda}(\boldsymbol{q})|i^{\mathrm{ph}}\rangle. \tag{5.8}$$

Here, $B_{ns}^{\dagger}(\boldsymbol{K})$ ($B_{ns}(\boldsymbol{K})$) is the creation (annihilation) operator of an exciton in the n-th carbon nanotube, with quantum number s and center-of-mass momentum $\boldsymbol{K}$. Also, $c_{n\lambda}^{\dagger}(\boldsymbol{q})$ ($c_{n\lambda}(\boldsymbol{q})$) is the creation (annihilation) operator of a phonon the n-th carbon nanotube, in phonon branch λ, and wave vector $\boldsymbol{q}$.

There are two types of second-order exciton transfer that are possible through the interaction Hamiltonian in Eq. (5.2): (i) intratube exciton scattering via interaction with phonons in the donor carbon nanotube, followed by the intertube exciton scattering via Coulomb coupling of intermediate state with the final state in the acceptor CNT; (ii) intertube exciton scattering via Coulomb coupling followed, by intratube exciton scattering via interaction with phonons in the acceptor tube. Figure 5.2 shows a schematic of these two types of process. In each of these processes, the exciton–phonon scattering is possible through phonon

absorption and emission; however, the phonon emission rate is usually dominant and we will show the resutls only for this process. It is also important to note that the intertube exciton transfer is facilitated by Coulomb coupling, therefore, strong Coulomb coupling between the excitonic states is essential in efficient second-order exciton coupling.

5.2 Phonon emission followed by Coulomb coupling

In this process, the initial and final states are

$$|i\rangle = |1, s_1, \boldsymbol{K}_1\rangle \otimes |i^{\rm ph}\rangle \quad \text{and} \quad |f\rangle = |2, s_2, \boldsymbol{K}_2\rangle \otimes |i^{\rm ph} + (1, \lambda, \boldsymbol{q})\rangle \ . \tag{5.9}$$

Therefore, the nonzero matrix elements in Eq. (5.1) are for the transition states of the following form:

$$|m\rangle = |1, s', \boldsymbol{K}_1 - \tfrac{\boldsymbol{q}}{2}\rangle \otimes |i^{\rm ph} + (1, \lambda, \boldsymbol{q})\rangle, \tag{5.10}$$

where the quantum number, s', runs over all available excitonic states with the center-of-mass momentum $\boldsymbol{K} - \frac{\boldsymbol{q}}{2}$. Therefore, the exciton transition rate is

$$\begin{aligned} S(s_1, \boldsymbol{K}_1; s_2, \boldsymbol{K}_2; \lambda, \boldsymbol{q}) = \frac{2\pi}{\hbar} \left| \sum_{s'} \frac{g_{1s_1s'}(\lambda, \boldsymbol{q}, \boldsymbol{K}_1)\ M(\boldsymbol{K}_1 - \frac{\boldsymbol{q}}{2}, s'; \boldsymbol{K}_2, s_2)}{\Omega_{1,s_1}(\boldsymbol{K}_1) - \Omega_{1,s'}(\boldsymbol{K}_1 - \frac{\boldsymbol{q}}{2}) - \hbar\omega_{1,\lambda}(\boldsymbol{q})} \right|^2 \times \cdots \\ \cdots \big(n_\lambda(\boldsymbol{q}) + 1\big) \times \delta\big(\Omega_{1,s_1}(\boldsymbol{K}_1) - \Omega_{2,s_2}(\boldsymbol{K}_2) - \hbar\omega_{1,\lambda}(\boldsymbol{q})\big). \end{aligned} \tag{5.11}$$

In order to get the total scattering rate from state $|1, s_1, \boldsymbol{K}_1\rangle$, we need to perform a summation over the final excitonic (s_2 and $\boldsymbol{K}_2$) and phononic (λ and $\boldsymbol{q}$) states.

$$\begin{aligned} \Gamma(s_1, \boldsymbol{K}_1) = \frac{2\pi}{\hbar} \sum_{s_2, \boldsymbol{K}_2} \sum_{\lambda, \boldsymbol{q}} \Bigg[\big(n_\lambda(\boldsymbol{q}) + 1\big) \left| \sum_{s'} \frac{g_{1s_1s'}(\lambda, \boldsymbol{q}, \boldsymbol{K}_1)\ M(\boldsymbol{K}_1 - \frac{\boldsymbol{q}}{2}, s'; \boldsymbol{K}_2, s_2)}{\Omega_{1,s_1}(\boldsymbol{K}_1) - \Omega_{1,s'}(\boldsymbol{K}_1 - \frac{\boldsymbol{q}}{2}) - \hbar\omega_{1\lambda}(\boldsymbol{q})} \right|^2 \times \cdots \\ \cdots \delta\big(\Omega_{1,s_1}(\boldsymbol{K}_1) - \Omega_{2,s_2}(\boldsymbol{K}_2) - \hbar\omega_{1\lambda}(\boldsymbol{q})\big) \Bigg]. \end{aligned} \tag{5.12}$$

However, owing to different shapes of the Coulomb-coupling matrix element in for the cases of parallel and nonparallel (misoriented) tubes, the total scattering rates and the selection rules will be different for different orientations. In the following sections, we derive the rates for these two cases.

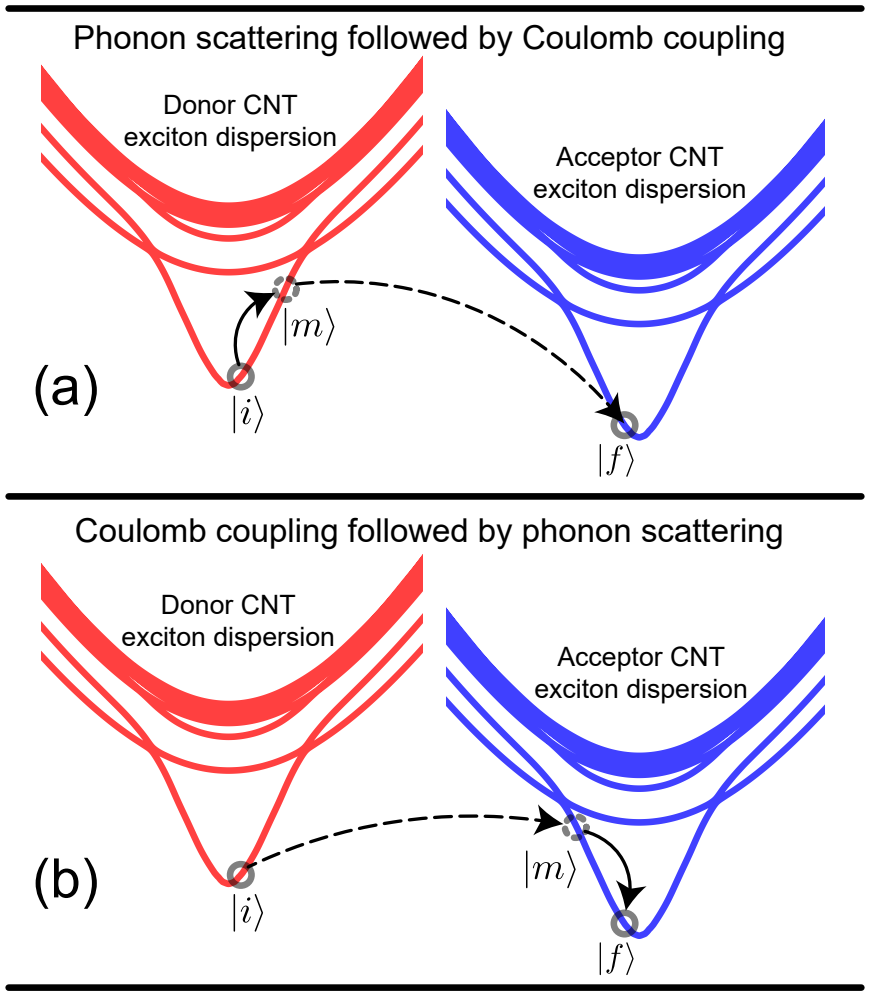

Figure 5.2: Schematic of second-order exciton scattering. Panel (a) shows exciton hopping where intratube exciton–phonon scattering is followed by intertube exciton scattering via Coulomb coupling. Panel (b) shows exciton hopping where intertube exciton scattering via Coulomb coupling is followed by intratube exciton–phonon scattering. Black dashed lines represent scattering via Coulomb coupling and black solid lines represent scattering via exciton–phonon interaction. Solid red and blue curves show the exciton energy dispersions in donor and acceptor CNTs, respectively.

5.3 Case of nonparallel tubes

We explicitely write the size-dependence the matrix elements. The Coulomb-coupling matrix element is [see Eq. (3.26)],

$$M(s_1, \boldsymbol{K}_1; s_2, \boldsymbol{K}_2) = \frac{1}{\sqrt{L_1 L_2}}\, M_\perp(s_1, \boldsymbol{K}_1; s_2, \boldsymbol{K}_2), \tag{5.13}$$

where $M_\perp$ is the size-independent part the Coulomb-coupling matrix element for nonparallel CNTs:

$$M_\perp(s_1, \boldsymbol{K}_1; s_2, \boldsymbol{K}_2) = J_\theta(\boldsymbol{K}_1, \boldsymbol{K}_2) \times Q(s_1, \boldsymbol{K}_1, s_2, \boldsymbol{K}_2). \tag{5.14}$$

By using the relation $N_u = \frac{2\pi r L}{A_u}$ and the exciton–phonon matrix element in Eq. (4.38), we get

$$g_{1ss'}(\lambda, \boldsymbol{q}, \boldsymbol{K}) = \frac{1}{\sqrt{L}} \tilde{g}_{1ss'}(\lambda, \boldsymbol{q}, \boldsymbol{K}), \tag{5.15}$$

where we have defined the size-independent matrix element as

$$\begin{aligned}
\tilde{g}_{ss'}(\lambda, \boldsymbol{q}, \boldsymbol{K}) = &- \left(\frac{g^2 \hbar A_u}{16\pi r m \omega_\lambda(\boldsymbol{q})} \right)^{\frac{1}{2}} \times \cdots \\
&\cdots \left(\sum_{\boldsymbol{k}_r} A^*_{s'}(\boldsymbol{K} - \tfrac{\boldsymbol{q}}{2}, \boldsymbol{k}_r - \tfrac{\boldsymbol{q}}{2}) A_s(\boldsymbol{K}, \boldsymbol{k}_r) \big(\tilde{f}_{1,\lambda}(\boldsymbol{k}_r + \boldsymbol{K} - \boldsymbol{q}, \boldsymbol{q}) + \tilde{f}_{2,\lambda}(\boldsymbol{k}_r + \boldsymbol{K}, \boldsymbol{q}) \big) \right. \\
&\left. + \sum_{\boldsymbol{k}_r} A^*_{s'}(\boldsymbol{K} - \tfrac{\boldsymbol{q}}{2}, \boldsymbol{k}_r + \tfrac{\boldsymbol{q}}{2}) A_s(\boldsymbol{K}, \boldsymbol{k}_r) \big(\tilde{f}_{1,\lambda}(\boldsymbol{k}_r - \boldsymbol{K}, \boldsymbol{q}) + \tilde{f}_{2,\lambda}(\boldsymbol{k}_r - \boldsymbol{K} + \boldsymbol{q}, \boldsymbol{q}) \big) \right).
\end{aligned} \tag{5.16}$$

Therefore, by converting the summation over the wave vector $\boldsymbol{q}$ to an integral in Eq. (5.12), we get

$$\begin{aligned}
\Gamma(s_1, \boldsymbol{K}_1) = \frac{1}{2\pi\hbar L_1} \sum_{s_2, \mathscr{M}_2} \sum_{\lambda,\mu} \iint dK_2\, dq \, \Bigg[&\big(n_\lambda(\boldsymbol{q}) + 1 \big) \times \cdots \\
&\cdots \left| \sum_{s'} \frac{\tilde{g}_{1 s_1 s'}(\lambda, \boldsymbol{q}, \boldsymbol{K}_1)\; \tilde{M}(\boldsymbol{K}_1 - \frac{\boldsymbol{q}}{2}, s'; \boldsymbol{K}_2, s_2)}{\Omega_{1,s_1}(\boldsymbol{K}_1) - \Omega_{1,s'}(\boldsymbol{K}_1 - \frac{\boldsymbol{q}}{2}) - \hbar\omega_{1\lambda}(\boldsymbol{q})} \right|^2 \delta\big(\Omega_{1,s_1}(\boldsymbol{K}_1) - \Omega_{2,s_2}(\boldsymbol{K}_2) - \hbar\omega_{1,\lambda}(\boldsymbol{q}) \big) \Bigg].
\end{aligned} \tag{5.17}$$

After performing the integral over phonon wave vector, we get

$$\Gamma(s_1, \boldsymbol{K}_1) = \frac{1}{2\pi\hbar L_1} \sum_{s_2, \mathscr{M}_2} \sum_{\lambda,\mu} \int dK_2 \; \frac{n_\lambda(\boldsymbol{q}_0) + 1}{|\hbar\dot{\omega}_{1\lambda}(\boldsymbol{q}_0)|} \times \cdots \\ \cdots \left| \sum_{s'} \frac{\tilde{g}_{1s_1s'}(\lambda, \boldsymbol{q}_0, \boldsymbol{K}_1) \; \tilde{M}(\boldsymbol{K}_1 - \frac{\boldsymbol{q}_0}{2}, s'; \boldsymbol{K}_2, s_2)}{\Omega_{1,s_1}(\boldsymbol{K}_1) - \Omega_{1,s'}(\boldsymbol{K}_1 - \frac{\boldsymbol{q}_0}{2}) - \hbar\omega_{1\lambda}(\boldsymbol{q}_0)} \right|^2 . \tag{5.18}$$

Here, $\boldsymbol{q}_0$ is the wave vector of the phonon that conserves the energy in the transfer process.

$$\Omega_{s'}(\boldsymbol{K} - \tfrac{\boldsymbol{q}_0}{2}) = \Omega_s(\boldsymbol{K}) \mp \hbar\omega_\lambda(\pm\boldsymbol{q}_0). \tag{5.19}$$

However, note that the momentum does not need to be conserved, because the tubes are misoriented.

Equation (5.18) for the total exciton transfer rate is particularly interesting because of the presense of the phonon density of states,

$$\frac{1}{\hbar\dot{\omega}_{1,\lambda}(\boldsymbol{q})} = \left(\hbar \frac{\partial\omega_{1,\lambda}(\boldsymbol{q})}{\partial q}\right)^{-1}. \tag{5.20}$$

This term is absent in common phonon-assisted second order processes in bulk materials which conserve both momentum and energy. In these cases of phonon-assisted second-order processes, the degree of freedom over phonon wave vector is eliminated by momentum conservation which would result in a dependence on the electronic (excitonic) density of states. The phonon density of states is much higher than the electronic density of states, therefore we would expect a second-order exciton transfer rate with a higher rate that is normally expected from a second-order process. An example of these types of second-order process is the nRET for parallel CNTs, as we will show in the next Section the exciton-transfer rate only depends on the exciton density of states.

Singlet excitons in CNTs are divided into two classes based on their angular momentum along the circumference of the CNT. Excitons with zero angular momentum ($\mathscr{M} = 0$) are A-type excitons and excitons with nonzero angular momentum ($\mathscr{M} \neq 0$) are known as E-type excitons. Furthermore, A-type excitons also split into two classes based on their inversion symmetry. The symmetric A-type excitons are denoted as A_1 excitons while the

antisymmetric A-type excitons are denoted as A_2 excitons. The A_2 excitons are optically active [1] (bright excitons), while the A_1 excitons are optically inactive due to their symmetry (dark excitons). Also, E-type excitons are optically inactive due to their large angular momentum. Therefore, the Coulomb coupling and the first-order ET rate among A_2 excitons are generally two orders of magnitude higher than the Coulomb coupling and ET rate between E-type and A_2 excitons [77]. In the following, we show the calculation of nRET rates between bright and dark excitonic states in several different pairs of CNTs.

5.3.1 Exciton transfer among bright states

Figure 5.3(a) shows this phonon-assisted ET rates among A_2 excitonic states of perpendicular CNTs. The ET happens through emitting a phonon in the donor CNT followed by the Coulomb coupling of the transition excitonic state in the donor CNT to the final excitonic state in the acceptor CNT. The ET rates are within the range of measurements [50, 51, 52, 53, 54, 55, 56, 57, 58, 70] and have the same order of magnitude as the theoretical calculations of the first-order ET rates [77], which makes them important from both experimental and theoretical points of view. Due to its second-order nature, the phonon-assisted ET process has a smaller transition rate than the resonant first-order ET process. However, the special form of the Coulomb-coupling matrix element in Eq. (5.13), which does not conserve momentum, creates an extra degree of freedom (phonon momentum) in the case of of nonparallel CNTs, which compensates for the small transition rate.

As we can see in Fig. 5.3(a), the ET rate increases with increasing exciton kinetic energy. However, the ET rate at the bottom of excitonic band is more important because of higher exciton occupation number. Figure 5.3(b) shows the ET rate multiplied by the exciton occupation number, where we have assumed that the excitons are distributed according to the thermal equilibrium distribution function: $N(\Omega) = \left(e^{-\beta\Omega}\frac{\partial K}{\partial \Omega}\right)/\mathcal{Z}$. The effective ET rates measured in experiments are the area below these curves. We have reported the effective ET rates in Table 5.1. As we can see, the effective ET rate between perpendicular CNTs with

[1] Optically active means being able to absorb or emit photons.

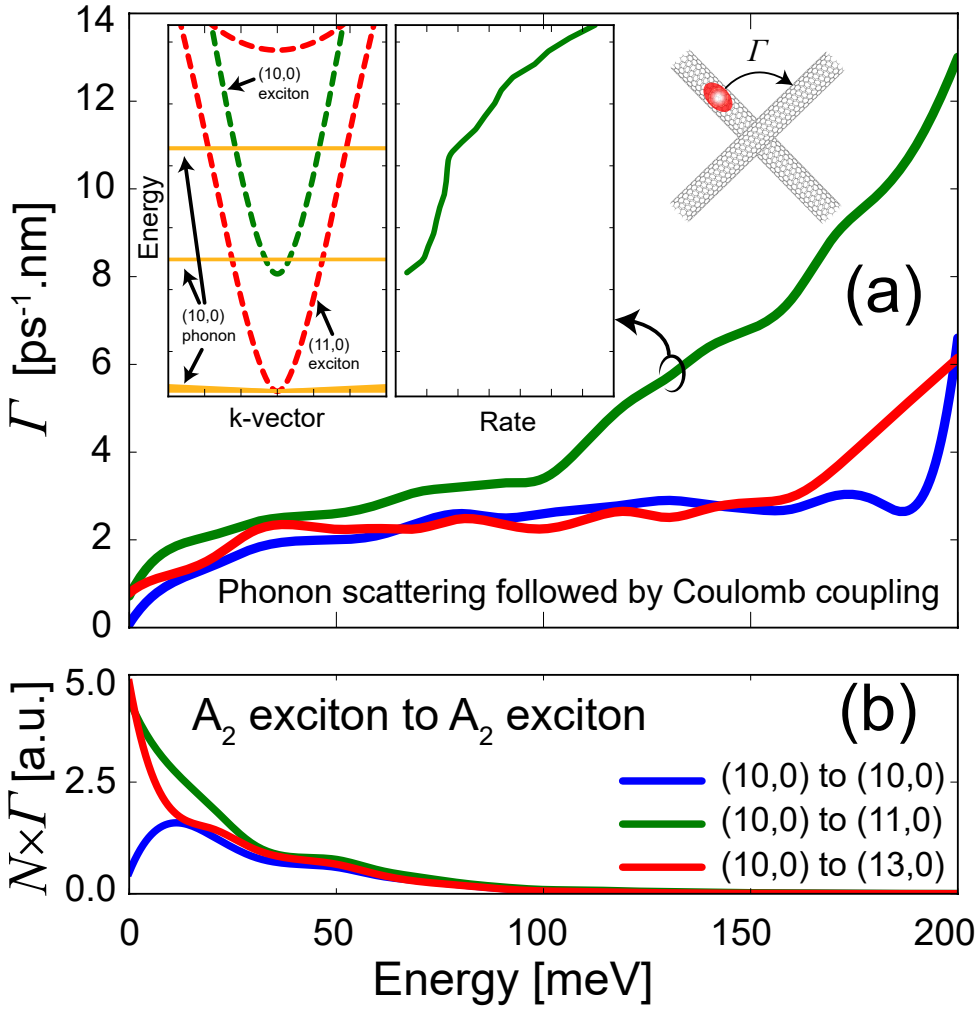

Figure 5.3: (a) Phonon-assisted ET rates among A_2 excitons in pairs of perpendicular CNTs (phonon emission followed by Coulomb coupling). The energy axis starts from the bottom of the excitonic band in the donor CNT. The insets show the energy dispersion of initial and final excitonic states in comparison to the ET rate. The green dashed line is the excitonic energy dispersion in (10,0) donor CNT. The red dashed lines are the excitonic dispersions of (11,0) acceptor CNT. Horizontal solid yellow lines are phononic energy dispersions in (10,0) CNT. (b) Phonon-assisted ET rates multiplied by the thermal equilibrium occupation number at temperature $T = 300$K.

same chirality is lower by a factor of two than the ET rate between pairs of perpendicular CNTs with different chiralities. This is because of the ET rate at the bottom of excitonic energy dispersion. When the donor and acceptor CNTs are similar, the excitons at the bottom of the band cannot emit any phonon and the phonon-assisted ET rate is zero (see blue curves in Fig. 5.3). However, for excitons with higher energies, we start to see emission of acoustic phonons and the ET rate is nonzero. On the other hand, if the acceptor CNT has a smaller energy gap, the excitons at the bottom of the dispersion curve have enough energy for radiating acoustic phonons and the scattering rate is considerably higher [green and red curves in Fig. 5.3(b)]. As the exciton energy increases past the optical-phonon energies, we see a larger jump in the scattering rates. The inset in Fig. 5.3 shows the scattering rate between (10,0) and (11,0) CNTs on the same energy scales as the excitonic and phononic energy dispersions in the CNTs. We can see the turn-on of new exciton scattering pathways as the emission of new optical phonons becomes possible.

As we stated before, the phonon-assisted ET rates via process types (i) and (ii) are similar in terms of their mathematical expressions. However, the minor differences in the selection rules results in major differences in the behaviors of ET rates via process types (i) and (ii). Figure 5.4(a) shows the second-order ET rates via Coulomb coupling followed by phonon scattering [Fig. 5.2(b)]. As we can see, in all cases (similar and dissimilar donor and acceptor CNTs), the ET rates tend to zero at the bottom of the exciton energy band. This is due to the shape of the Coulomb-coupling matrix element, Eq. (5.13), where it tends to zero for $\boldsymbol{K}_1 = 0$ or $\boldsymbol{K}_2 = 0$. When the Coulomb coupling happens first, we have $\boldsymbol{K}_1 \approx 0$ for the states at the bottom of excitonic energy band, leading to a zero scattering rate regardless of the bandgap of the acceptor CNT. Therefore, as we can see in Fig. 5.4, the highly populated excitonic states have very small ET rates, which produces lower effective ET rates than the rates in process type (i).

We also observe a few orders of magnitude jump in the ET rate at the energies at which optical phonons become available: $\Omega_{1,s_1}(\boldsymbol{K}_1) - \min(\Omega_2) = \hbar\omega_{\text{optical}}$. The huge jumps are a consequence of the high density of final excitonic states at the bottom of acceptor CNT

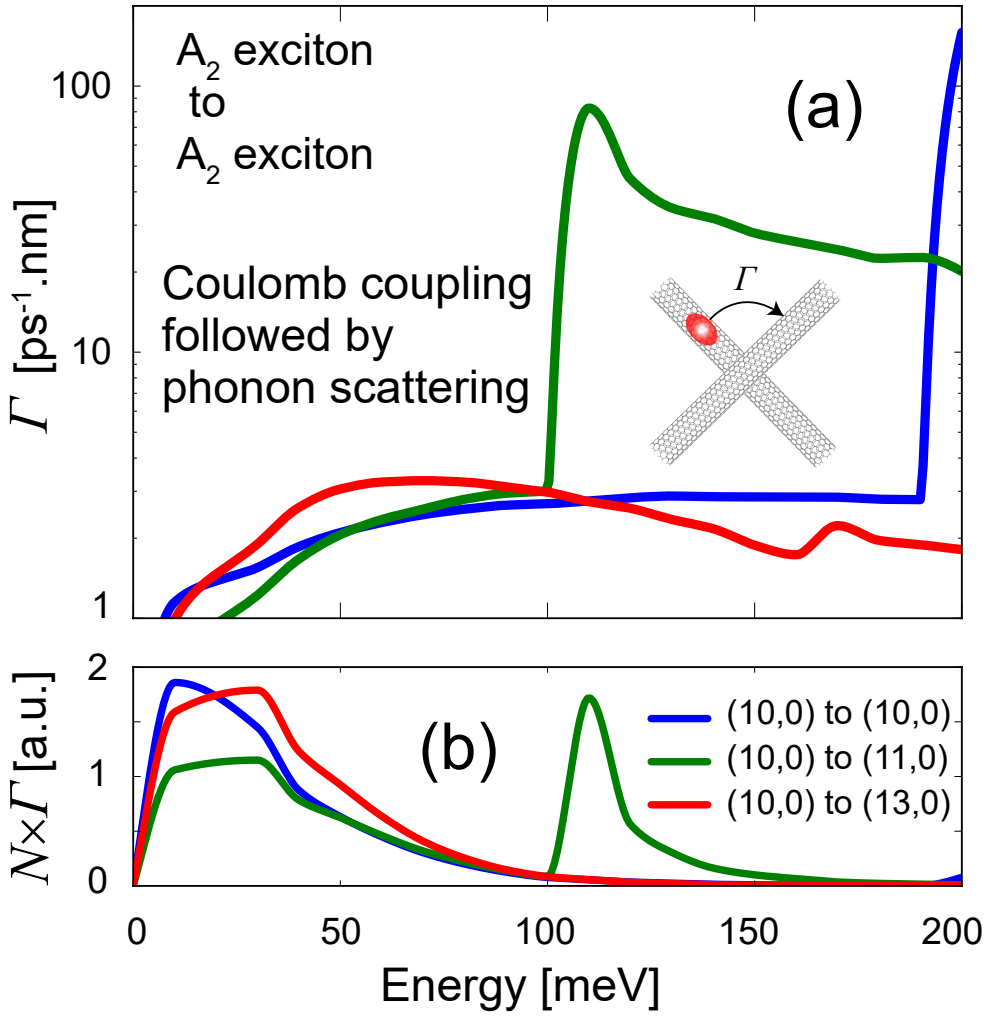

Figure 5.4: (a) Phonon-assisted ET rates among A_2 excitons in pairs of perpendicular CNTs via Coulomb coupling followed by phonon scattering. The energy axis starts from the bottom of excitonic band in the donor CNT. (b) Phonon-assisted ET rates multiplied by the thermal equilibrium occupation number at temperature $T = 300$K.

energy band. These ET rates are comparable to the intratube exciton relaxation rates (due to exciton–phonon and exciton–impurity interactions) and it is possible to observe transfer of hot excitons between CNTs via second-order process type (ii), before their relaxation to lower energy excitonic states.

5.3.2 Exciton transfer between bright and dark states

Now, we turn into the ET between bright and dark excitonic states. The first-order ET from E-type dark excitonic states to bright excitonic states are at least two orders of magnitude smaller that the first-order ET among A_2 bright excitonic states [77]. The reason is the weak Coulomb coupling of E-type excitons to any other type of exciton. However, we can overcome this limitation in the context of second-order exciton scattering. Figure 5.5(a) shows the scattering rates of E-type excitons in (10,0) CNT to A_2 excitons in acceptor CNTs with various chiralities. As we can see, if the excitons have enough energy to emit an acoustic or optical phonon, the transfer rate from dark to bright excitonic states can exceed 10^{12} s^{-1}nm, about two orders of magnitude improvement upon the first-order ET rate between the same excitonic states. As we can see in the insets to Fig. 5.5(a), the ET process is of type (i) where in the first step the initial dark excitonic state (E) converts to a bright transition state (A_2) via phonon scattering. In the second step, the transition excitonic state couples to the final excitonic state via Coulomb interaction.

Unlike the case of ET from A_2 exciton, the ET rate from low energy E-type excitons is small even when the acceptor CNT has a smaller band gap. This behavior can be understood by noting the large difference in angular momentum between E-type and A_2 excitons. Therefore, both acoustic and optical phonons that facilitate the second-order ET of E-type excitons have a large angular moementum with energies higher than 50 meV. This means that the low-energy excitons can only transfer if the excitonic energy of the acceptor CNT is lower by more than 50 meV. Among different choices of sample CNTs, this criterion is satisfied when ET happens from (10,0) to (13,0), where we observe a much higher effective ET rates than the other choices [Figure 5.5(b)].

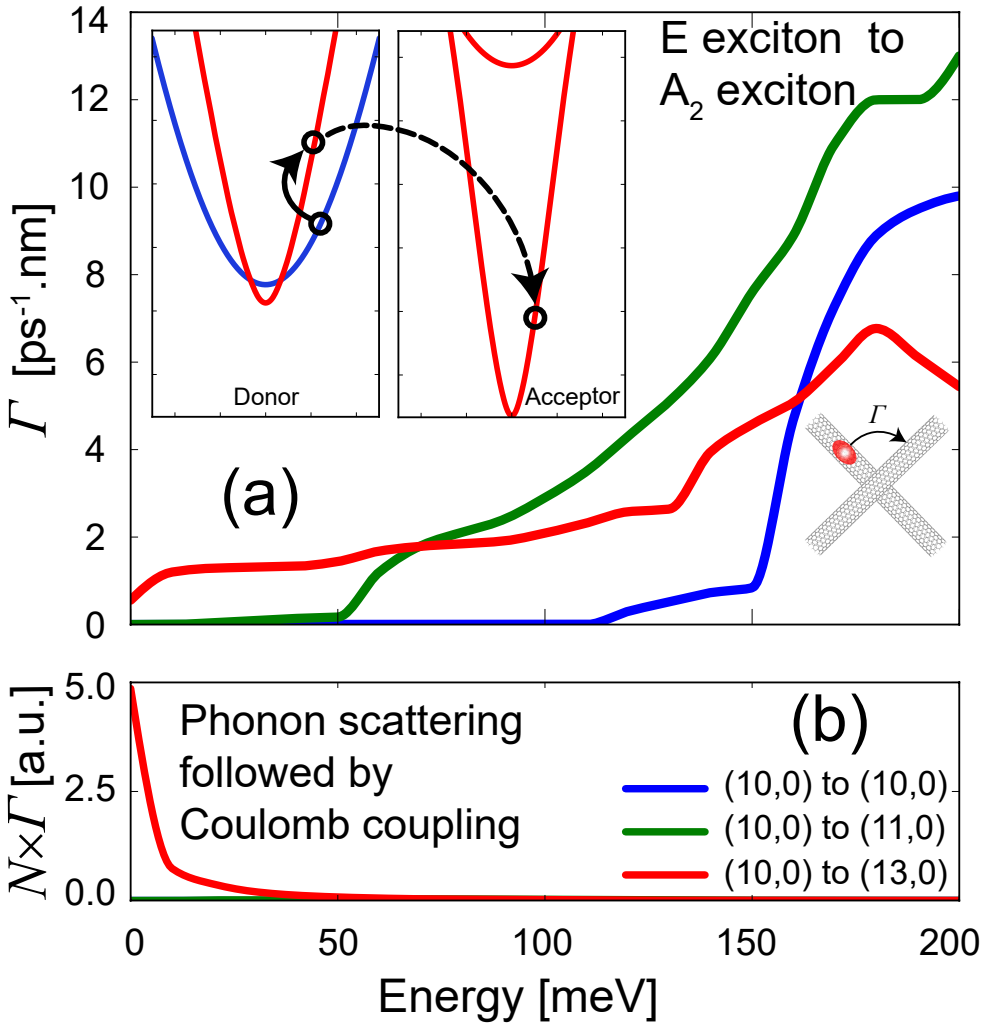

Figure 5.5: (a) Phonon-assisted ET rates from E-excitons to A_2 excitons in pairs of perpendicular CNTs. The energy axis starts from the bottom of excitonic band in the donor CNT. Insets show a schematic of ET mechanism, where in the first step the E-type exciton is converted to an A_2 exciton in the donor CNT via phonon scattering. Then in the second step the A_2 transition excitonic state is converted to the an A_2 exciton in acceptro CNT. Solid blue (red) curve shows dispersion of E-type (A_2) excitons. Solid black arrow shows exciton–phonon scattering, while dashed black arrow shows Coulomb coupling process. (b) Phonon-assisted ET rates multiplied by the thermal equilibrium occupation number at temperature $T = 300$K.

5.4 Case of parallel tubes

When the two CNTs are parallel, the Coulomb coupling matrix element is independent of the length of the CNTs and conserves the center-of-mass momentum in the exciton transfer process

$$M(s_1, \boldsymbol{K}_1; s_2, \boldsymbol{K}_2) = \delta_{K_1,K_2} \times M_{\parallel}(s_1, \boldsymbol{K}_1; s_2, \boldsymbol{K}_2), \tag{5.21}$$

where, according to Eq. (3.39), we have defined

$$M_{\parallel}(s_1, \boldsymbol{K}_1; s_2, \boldsymbol{K}_2) = C(\mathscr{M}_1, \mathscr{M}_2; K_1) \times Q(s_1, \boldsymbol{K}_1; s_2, \boldsymbol{K}_2). \tag{5.22}$$

Furthermore, the exciton–phonon interaction matrix element is the same as in Eq. (5.15). By converting the summation over the wave vector $\boldsymbol{q}$ to an integral in Eq. (5.12), we get

$$\begin{aligned}\Gamma(s_1, \boldsymbol{K}_1) = \frac{1}{\hbar} \sum_{s_2, \boldsymbol{K}_2} \sum_{\lambda,\mu} \int dq \; \Bigg[\big(n_\lambda(\boldsymbol{q}) + 1\big) \times \delta_{K_1 - \frac{q}{2}, K_2} \times \cdots \\ \cdots \left| \sum_{s'} \frac{\tilde{g}_{1 s_1 s'}(\lambda, \boldsymbol{q}, \boldsymbol{K}_1) \; M_{\parallel}(\boldsymbol{K}_1 - \frac{\boldsymbol{q}}{2}, s'; \boldsymbol{K}_2, s_2)}{\Omega_{1,s_1}(\boldsymbol{K}_1) - \Omega_{1,s'}(\boldsymbol{K}_1 - \frac{\boldsymbol{q}}{2}) - \hbar\omega_{1,\lambda}(\boldsymbol{q})} \right|^2 \delta\big(\Omega_{1,s_1}(\boldsymbol{K}_1) - \Omega_{2,s_2}(\boldsymbol{K}_2) - \hbar\omega_{1,\lambda}(\boldsymbol{q})\big) \Bigg]\end{aligned} \tag{5.23}$$

After performing the integral, we get

$$\begin{aligned}\Gamma(s_1, \boldsymbol{K}_1) = \frac{1}{\hbar} \sum_{s_2, \boldsymbol{K}_{2,0}} \sum_{\lambda,\mu} \frac{n_\lambda(\boldsymbol{q}_0) + 1}{|\frac{1}{2}\dot{\Omega}_{2,s_2}(\boldsymbol{K}_{2,0}) - \hbar\dot{\omega}_{1,\lambda}(\boldsymbol{q}_0)|} \times \cdots \\ \cdots \left| \sum_{s'} \frac{\tilde{g}_{1 s_1 s'}(\lambda, \boldsymbol{q}_0, \boldsymbol{K}_1) \; M_{\parallel}(\boldsymbol{K}_1 - \frac{\boldsymbol{q}_0}{2}, s'; \boldsymbol{K}_{2,0}, s_2)}{\Omega_{1,s_1}(\boldsymbol{K}_1) - \Omega_{1,s'}(\boldsymbol{K}_1 - \frac{\boldsymbol{q}_0}{2}) - \hbar\omega_{1,\lambda}(\boldsymbol{q}_0)} \right|^2 .\end{aligned} \tag{5.24}$$

Here, $\boldsymbol{q}_0$ and $\boldsymbol{K}_{2,0}$ are the wave vectors of phonon and excitonic states that conserve both energy and momentum $\Omega_{2,s_2}(\boldsymbol{K}_{2,0}) = \Omega_{1,s_1}(\boldsymbol{K}_1) - \hbar\omega_{1,\lambda}(\boldsymbol{q}_0)$ and $\boldsymbol{K}_{2,0} = \boldsymbol{K}_1 - \frac{\boldsymbol{q}_0}{2}$.

We note that, in the case of parallel CNTs, the phonon density of states, which we was for nonparallel tubes, is replaced with the density of excitonic states. Therefore, in contrast

to the perpendicular case, the phonon-assisted exciton scattering rate between parallel tubes does not benefit from the large density of phononic states. However, the Coulomb coupling between parallel CNTs is much stronger than the Coulomb coupling between perpendicular CNTs. For example, the first-order ET between parallel CNTs could potentially be two orders of magnitude faster (rate of 0.01 ps^{-1}) than the first-order ET between nonparallel CNTs [77]. However, the number of exictonic states that obey the selection rules is limited for most combinations of donor and acceptor CNT chiralities, therefore the first-order ET rate is usually less than 1 ps^{-1} [77]. In the second-order exciton scattering, the presence of phonons helps with finding the final excitonic states that obey the selection rules. Hence, the second-order ET rate rises by enabling ET between larger number of excitonic states in donor and acceptor CNTs.

As we can see in Fig. 5.6(a), the exciton scattering rates between bright states are higher than 1 ps^{-1} regardless of the chirality of donor and acceptor CNTs. Figure 5.6(b) shows the exciton scattering rate from E-type excitons to A_2 excitons in pairs of parallel CNTs. The scattering rates have the same trend as the rates in Fig. 5.5(a). Again, the scattering rate of low-energy excitons is large when the difference between bottoms of excitonic dispersion energies in donor and acceptor CNTs is large enough to allow phonon emission.

In summary, the second-order ET rates between parallel CNTs are about two orders of magnitude lower that the maximal first-order ET rates between parallel CNTs, which happens only when the excitonic energy dispersions in the donor and acceptor CNTs are exactly the same. However, in most cases the first-order ET rate is much lower (~ 0.1 ps^{-1}) since the exciton dispersions in the donor and acceptor CNTs are different either due to sample inhomogeneity or different chirality of the tubes. Therefore, the second-order ET processes are important since the reported rates are faster than the first-order ET rates.

5.5 Conclusion

In this Chapter, we performed a calculation of second-order phonon-assisted ET between pairs of CNTs with parallel and perpendicular orientations. We showed that the ET rates

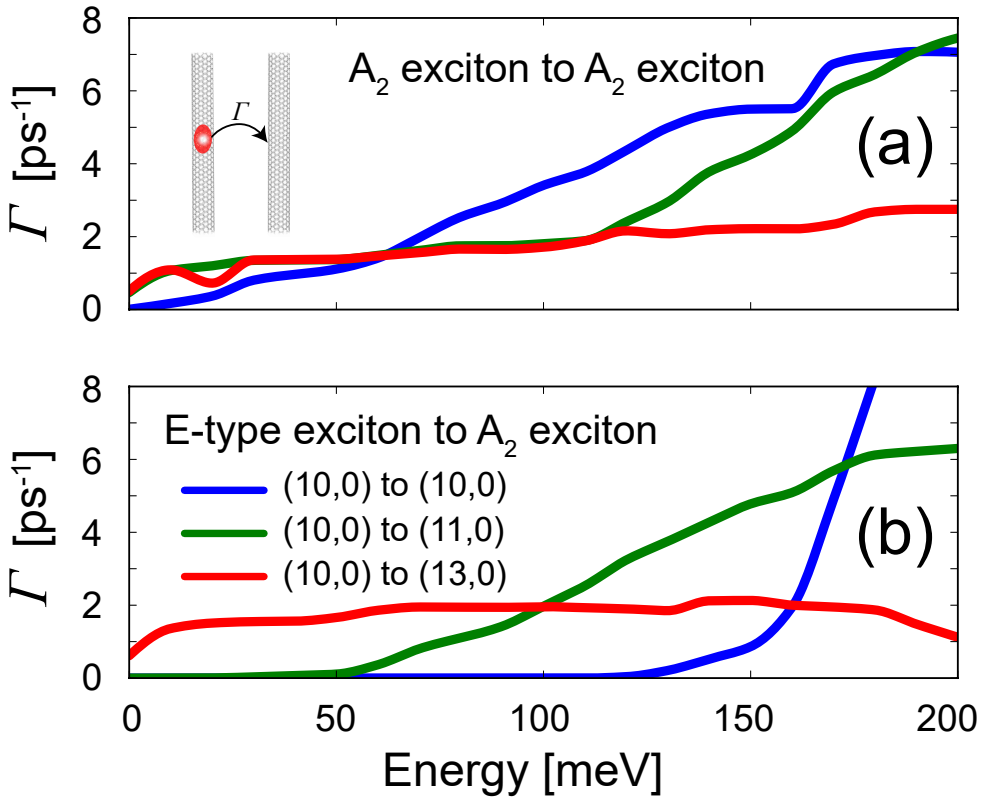

Figure 5.6: (a) Phonon-assisted ET rates among A_2 excitons in pairs of parallel CNTs (intratube phonon scattering followed by intertube Coulomb coupling). (b) Phonon-assisted ET rates from E excitons to A_2 excitons in pairs of parallel CNTs (intratube phonon scattering followed by intertube Coulomb coupling). The energy axes starts from the bottom of the excitonic band in the donor CNT.

and the selection rules for the initial and final states are dramatically different between these two cases. Table 5.1 shows a summary of the effective ET rates between bright and dark excitonic states of three sample CNTs. As we can see, the second-order ET rates between bright excitonic states are generally higher than 1 ps^{-1} which is roughtly the same order of magnitude as first-order ET rate. The second-order ET rate between dark and bright excitonic states also can reach values as high as 1 ps^{-1}, which is about two orders of magnitude larger than the first-order ET rates between bright and dark excitons. The ET from dark excitonic states is facilitated by intratube exciton–phonon scattering into a bright excitonic state followed by the intertube ET via efficient Coulomb coupling between the bright excitonic states.

We showed that these conclusions are true for both parallel and perpendicular tube orientations. The large ET rate between perpendicular CNTs stems from the relatively high density of phononic states in comparision to the excitonic states. In the case of parallel CNTs, the large excitonic scattering rate is a result of a more relaxed selection rule which is due to introduction of phonons.

These findings are important from the theoretical standpoint: the second-order process is as probable as the first-order process. Also, our results are important from the experimental point of view that the dark excitonic states are able to directly transfer between the tubes in a CNT film with a considerably higher rate than previously assumed.

		(10,0) → (10,0)		(10,0) → (11,0)		(10,0) → (13,0)	
Orientation	Proc. type	$A_2 \leftrightarrow A_2$	$E \leftrightarrow A_2$	$A_2 \leftrightarrow A_2$	$E \leftrightarrow A_2$	$A_2 \leftrightarrow A_2$	$E \leftrightarrow A_2$
Perpendicular	(i)	6.14×10^{-1}	1.41×10^{-3}	1.30	2.59×10^{-2}	1.12	6.55×10^{-1}
Perpendicular	(ii)	6.22×10^{-1}	2.36×10^{-2}	7.85×10^{-1}	1.11	7.21×10^{-1}	3.28×10^{-1}
Parallel	(i)	1.17	3.89×10^{-3}	1.44	8.18×10^{-2}	1.42	1.57
Parallel	(ii)	3.28×10^{-1}	1.17×10^{-1}	1.29×10^{-1}	2×10^{-1}	3.61×10^{-2}	1.63×10^{-2}

Table 5.1: Effective exciton transfer rates between perpendicular and parallel sets of carbon nanotubes at temperature $T = 300$ K. The rates for perpendicular orientation are reported in [ps^{-1}.nm] and the rates for parallel orientation are reported in [10^{12} s^{-1} = 1 ps^{-1}].

Chapter 6

Conclusion and Future Work

In the first part of this work, we presented a comprehensive theoretical analysis of the Coulomb-mediated intertube resonant exciton transfer (RET) in CNT composites, in which we paied attention to the complex structure of excitonic dispersions, exciton confinement, screening due to surrounding media, and temperature dependence of the RET rate. We solved the Bethe-Salpeter equation within the GW approximation in the basis of single-particle states obtained from nearest-neighbor tight binding to calculate the exciton dispersions and wave functions. We calculated the intertube RET rate due to the Coulomb interaction between CNTs of different chiralities and orientations. We showed that momentum conservation plays an important role in determining the RET rate between parallel CNTs of different chirality. While the RET rate between bundled parallel tubes with similar chirality in pristine samples is $\sim 10^{14}$ s^{-1}, much higher than the RET between misoriented or different-chirality CNTs ($\sim 10^{12}$ s^{-1}), exciton confinement due to disorder strongly reduces the RET rate between parallel tubes of similar chirality but has little effect on the RET rate otherwise. Consequently, the RET rate dependence on the orientation of donor and acceptor CNTs is not as prominent as previously predicted, and the RET rate is instead expected to be isotropic and 10^{12} s^{-1} in most experiments. Moreover, the RET rate drops by about one order of magnitude if intratube exciton scattering between bright and dark excitonic states is allowed. Our study showed that the transfer from S_{22} to S_{11} excitonic states happens with the same rate as the transfer process among same-subband states ($S_{11} \rightarrow S_{11}$ and

$S_{22} \rightarrow S_{22}$). We also showed that the RET rate increases with increasing temperature. Furthermore, the screening of the Coulomb interaction by the surrounding medium reduces the RET rate by changing the exciton wave function and energy dispersion, as well as by reducing the Coulomb coupling between the donor and acceptor CNTs. These results show that the wide range of exciton-transfer-rate measurements, spanning two orders of magnitude, stems from variations in sample preparation and thus the degree of environmental disorder and homogeneity, as the exciton transfer in pristine samples and in the samples in which environmental disorder results in exciton confinement differ by two orders of magnitude.

In the second part, we presented a calculation of the phonon-assisted nonresonant exciton-transfer (nRET) rates via second-order Fermi's Golden Rule. This transfer process consists of two successive scattering events: intratube scattering of excitons via their interaction with phonons and intertube scattering of excitons due to Coulomb coupling between two CNTs. The exciton–phonon interactions are calculated using the Su-Schrieffer-Heeger (SSH) model. The Coulomb coupling between excitonic states is calculated using the transition monopole approximation (TMA). Our results show that the second-order nRET process between CNTs has a rate of about 10^{12} s^{-1}, which is on par with the first-order RET process, the subject of the first part of this thesis. The reason behind this fast second-order process is twofold and depends on the orientation of the donor and acceptor tubes: (1) When the CNTs are nonparallel, the large density of phononic states that facilitate the nRET process causes the high transfer rate; (2) When the CNTs are parallel, the participation of phononic states helps with finding the initial and final quantum states that conserve the momentum and energy simultaneously, thereby increasing the number of donor and acceptor excitonic states, which leads to the fast phonon-assisted nRET. We also find that, for optically inactive E-type excitons, the phonon-assisted transfer rate ($\sim 10^{12}$ s^{-1}) is at least two orders of magnitude higher than the rate of first-order RET process ($\sim 10^{10}$ s^{-1}). These results are important from an experimental point of view, as optically inactive excitons are invisible in the most common measurement methods (time-resolved photoluminescence spectroscopy and pump-probe spectroscopy); therefore, one needs to complement measurements with

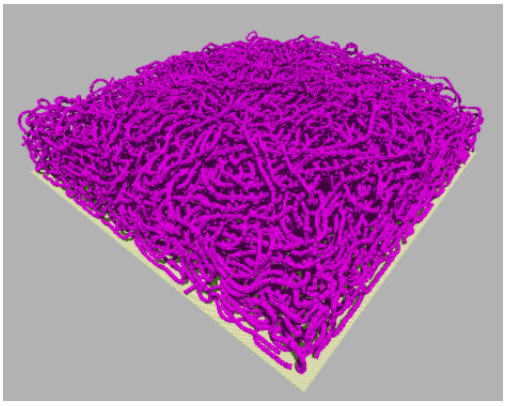

Figure 6.1: A realistic CNT mesh generated using BulletPhysics open source software.

theoretical calculations in order to get a correct picture of exciton dynamics in these types of nanostructures.

The results that were discussed so far enable us to simulate realistic CNT structures and films, and compare our results with measurements. In order to make the simulation as accurate as possible, we have generated a realistic CNT mesh by performing a mechanical simulation of CNTs using the BulletPhysics open source software (Fig. 6.1). In the next step, we will use the exciton transfer rates that we calculated in previous chapters along with the realistic CNT mesh geometry in a Monte Carlo simulation to calculate dynamics of exciton populations in different types of CNTs and exciton anisotropy. Comparing the simulation results with measurements [57, 56, 58, 70] will enable us to achieve a better understanding of the role of different parameters in CNT films (e.g., CNT chirality composition, density of tubes, tube alignment) in optimizing the exciton diffusion length. The results will be useful for applications of CNT films in photovoltaic devices [78].

DISCARD THIS PAGE

Appendix A: Numeric implementation of the Coulomb matrix element

In this Section, we talk about a few points in the implementation of the transfer rate calculation based on Eq. (3.38). In the calculation of excitonic wave functions, the basis that we use is formed in the following way. We calculate center-of-mass momentum $K = i_K \Delta K$. Therefore the calculated wavefunction is

$$|N, i_K, s\rangle = \sum_{i_{k_r}} A_s(i_K, i_{k_r})\, \hat{u}^\dagger(i_{k_r}\Delta k_r + i_K \Delta K)\, \hat{v}(i_{k_r}\Delta k_r - i_K \Delta K)|N, 0\rangle. \tag{A.1}$$

Here, Δk_r is the spacing between tight-binding basis function used in forming the exciton wavefunction. Ideally, Δk_r is equal to ΔK. However, the computation cost becomes very large for small ΔK and we have to take $\Delta k_r > \Delta K$.

This assumption has further implications in the way we calculate normalized k-space matrix element. As we discussed before, this quantity is size independent. The reasoning is as follows. The scale of coefficient $A(K, k_r)$ is dependent on the number of unit cells in a CNT:

$$A(K, k_r) \propto \frac{1}{\sqrt{N_u}} = \sqrt{\frac{A_u}{2\pi r_0}} \times \frac{1}{\sqrt{L}}. \tag{A.2}$$

On the other hand the number of relative coordinate wave vectors, k_r, is proportional on the number of unit cells

$$\sum_{k_r} \propto N_u = \frac{2\pi r_0}{A_u} \times L. \tag{A.3}$$

Therefore, the size dependence of the normalized k-space matrix element, $Q(K_1, K_2)$, is

$$Q(K_1, K_2) \propto \underbrace{\frac{1}{\sqrt{L_1}} \sum_{k_{r_1}} A_{s_1}(K_1, k_{r_1})}_{\frac{1}{\sqrt{L_1}} \times L_1 \times \frac{1}{\sqrt{L_1}} = 1} \times \overbrace{\frac{1}{\sqrt{L_2}} \sum_{k_{r_2}} A_{s_2}(K_2, k_{r_2}) \ldots}^{\frac{1}{\sqrt{L_2}} \times L_2 \times \frac{1}{\sqrt{L_2}} = 1} \propto 1. \tag{A.4}$$

In the numerical implementation of this calculation, the length of CNT is taken to be $L = \frac{2\pi}{\Delta k_r}$, which produces the correct size dependence. We could use another length value with

is given by $L = \frac{2\pi}{\Delta K}$, however, since we are doing a summation over $\boldsymbol{k}_r$, we use the former value for length.

Appendix B: Free-exciton transition matrix element

In this Section, we calculate the interaction integral in Eq. (3.29) when the integral limits for x and x' are infinite:

$$\mathcal{I} = \iint_{-\infty}^{+\infty} dx\, dx'\, e^{-2iK_1 x} e^{2iK_2 x'} \Big((x'\cos\theta - r_0'\cos\phi'\sin\theta - x)^2 + \cdots \\ \cdots (x'\sin\theta + r_0'\cos\phi'\cos\theta - r_0\cos\phi)^2 + (D + r_0'\sin\phi' - r_0\sin\phi)^2 \Big)^{-\frac{1}{2}}. \tag{B.1}$$

We use the following integral

$$\int_{-\infty}^{+\infty} dx\, \frac{e^{-ikx}}{\sqrt{x^2+\alpha^2}} = 2\mathcal{K}_0(\alpha k), \tag{B.2}$$

and integrate over x, which yields

$$\begin{aligned}\mathcal{I} =& 2\int_{-\infty}^{+\infty} dx'\, e^{2iK_2x'} e^{-2iK_1(x'\cos\theta - r_0'\cos\phi'\sin\theta)} \times \\ & \mathcal{K}_0\left(2|K_1|\sqrt{(x'\sin\theta + r_0'\cos\phi'\cos\theta - r_0\cos\phi)^2 + (D + r_0'\sin\phi' - r_0\sin\phi)^2}\right) \\ =& 2\, e^{2iK_1 r_0'\cos\phi'\sin\theta} \int_{-\infty}^{+\infty} dx'\, e^{2i(K_2 - K_1\cos\theta)x'} \times \\ & \mathcal{K}_0\left(2|K_1|\sqrt{(x'\sin\theta + r_0'\cos\phi'\cos\theta - r_0\cos\phi)^2 + (D + r_0'\sin\phi' - r_0\sin\phi)^2}\right).\end{aligned} \tag{B.3}$$

Now, we use the following integral to calculate the integral over x'

$$\int_{-\infty}^{+\infty} dx\, e^{ikx}\mathcal{K}_0(\alpha\sqrt{x^2+\beta^2}) = \pi\frac{\exp(-\beta\sqrt{k^2+\alpha^2})}{\sqrt{k^2+\alpha^2}}, \tag{B.4}$$

which yields

$$\begin{aligned}\mathcal{I} =& 2\pi\, e^{2iK_1 r_0'\cos\phi'\sin\theta} \times e^{-2i(K_2 - K_1\cos\theta)(r_0'\cos\phi'\cos\theta - r_0\cos\phi)/\sin\theta} \times \cdots \\ & \cdots \frac{\exp\left(-2\frac{|D + r_0'\sin\phi' - r_0\sin\phi|}{\sin\theta}\sqrt{(K_2 - K_1\cos\theta)^2 + (K_1\sin\theta)^2}\right)}{2\sqrt{(K_2 - K_1\cos\theta)^2 + (K_1\sin\theta)^2}}.\end{aligned} \tag{B.5}$$

After algebraic simplification, we get

$$\begin{aligned}\mathcal{I} =&\pi\ \exp\left(2i\frac{K_1(r_0'\cos\phi' - r_0\cos\phi\cos\theta) + K_2(r_0\cos\phi - r_0'\cos\phi'\cos\theta)}{\sin\theta}\right)\times\cdots \\ &\cdots\frac{\exp\left(-2\frac{|D+r_0'\sin\phi'-r_0\sin\phi|}{\sin\theta}\sqrt{K_2^2+K_1^2-2K_1K_2\cos\theta}\right)}{\sqrt{K_2^2+K_1^2-2K_1K_2\cos\theta}}.\end{aligned} \tag{B.6}$$

Therefore, Eq. (3.29) becomes

$$\begin{aligned}J_\theta(K_1,K_2) =&\pi\frac{r_0r_0'}{A_u^2}\int d\phi\ d\phi'\ \frac{\exp\left(-2\frac{|D+r_0'\sin\phi'-r_0\sin\phi|}{\sin\theta}\sqrt{K_2^2+K_1^2-2K_1K_2\cos\theta}\right)}{\sqrt{K_2^2+K_1^2-2K_1K_2\cos\theta}}\times\cdots \\ &\cdots\exp\left(2i\frac{K_1(r_0'\cos\phi' - r_0\cos\phi\cos\theta) + K_2(r_0\cos\phi - r_0'\cos\phi'\cos\theta)}{\sin\theta}\right)\end{aligned} \tag{B.7}$$

Appendix C: Second-order exciton scattering: Coulomb coupling followed by exciton–phonon scattering

In this appendix, we calculate the second-order exciton transfer rate for the transfer process type (ii), in which the initial state has Coulombic coupling to a transition (intermediate) state. The transition state is then scattered to the final state via exciton–phonon interaction. In this type of process, the initial and final states are

$$|i\rangle = |1, s_1, \boldsymbol{K}_1\rangle \otimes |i^{\mathrm{ph}}\rangle \quad \text{and} \quad |f\rangle = |2, s_2, \boldsymbol{K}_2\rangle \otimes |i^{\mathrm{ph}} + (2, \lambda, \boldsymbol{q})\rangle \tag{C.1}$$

Therefore, the nonzero matrix elements in Eq. (5.1) are for the transition states in the following form

$$|m\rangle = |2, s', \boldsymbol{K}_2 + \tfrac{\boldsymbol{q}}{2}\rangle \otimes |i^{\mathrm{ph}}\rangle, \tag{C.2}$$

where the quantum number, s', runs over all available excitonic states with a center-of-mass momentum $\boldsymbol{K}_2 + \frac{\boldsymbol{q}}{2}$. Therefore, the transition rate would be

$$\begin{aligned} S(s_1, \boldsymbol{K}_1; s_2, \boldsymbol{K}_2; \lambda, \boldsymbol{q}) = \frac{2\pi}{\hbar} \left| \sum_{s'} \frac{M(\boldsymbol{K}_1, s_1; \boldsymbol{K}_2 + \frac{\boldsymbol{q}}{2}, s')\ g_{2s's_2}(\lambda, \boldsymbol{q}, \boldsymbol{K}_2 + \frac{\boldsymbol{q}}{2})}{\Omega_{1,s_1}(\boldsymbol{K}_1) - \Omega_{2,s'}(\boldsymbol{K}_2 + \frac{\boldsymbol{q}}{2})} \right|^2 \times \cdots \\ \cdots \big(n_\lambda(\boldsymbol{q}) + 1\big) \times \delta\big(\Omega_{1,s_1}(\boldsymbol{K}_1) - \Omega_{2,s_2}(\boldsymbol{K}_2) - \hbar\omega_{2,\lambda}(\boldsymbol{q})\big) \end{aligned} \tag{C.3}$$

In order to get the total scattering rate from state $|1, s_1, \boldsymbol{K}_1\rangle$, we sum over all the final excitonic (s_2 and $\boldsymbol{K}_2$) and phononic (λ and $\boldsymbol{q}$) states

$$\begin{aligned} \Gamma(s_1, \boldsymbol{K}_1) = \frac{2\pi}{\hbar} \sum_{s_2, \boldsymbol{K}_2} \sum_{\lambda, \boldsymbol{q}} \Bigg[\big(n_\lambda(\boldsymbol{q}) + 1\big) \times \delta\big(\Omega_{1,s_1}(\boldsymbol{K}_1) - \Omega_{2,s_2}(\boldsymbol{K}_2) - \hbar\omega_{2,\lambda}(\boldsymbol{q})\big) \times \cdots \\ \cdots \left| \sum_{s'} \frac{M(\boldsymbol{K}_1, s_1; \boldsymbol{K}_2 + \frac{\boldsymbol{q}}{2}, s')\ g_{2s's_2}(\lambda, \boldsymbol{q}, \boldsymbol{K}_2 + \frac{\boldsymbol{q}}{2})}{\Omega_{1,s_1}(\boldsymbol{K}_1) - \Omega_{2,s'}(\boldsymbol{K}_2 + \frac{\boldsymbol{q}}{2})} \right|^2 \Bigg] \end{aligned} \tag{C.4}$$

However, because of different forms of the Coulomb-coupling matrix element in for the cases of parallel and nonparallel tube orientations, the total scattering rates and the selection

rules will be different. Performing a calculation similar to the one in Section 5.2, we get the following expression for the total exciton transfer rate between nonparallel CNTs

$$\Gamma(s_1, \boldsymbol{K}_1) = \frac{1}{2\pi\hbar L_1} \sum_{s_2, \mathscr{M}_2} \sum_{\lambda,\mu} \int dK_2 \left[\frac{n_{2,\lambda}(\boldsymbol{q}_0) + 1}{|\hbar\dot{\omega}_{2,\lambda}(\boldsymbol{q}_0)|} \times \cdots \right. \\ \left. \cdots \left| \sum_{s'} \frac{\tilde{M}(\boldsymbol{K}_1, s_1; \boldsymbol{K}_2 + \frac{\boldsymbol{q}_0}{2}, s') \; \tilde{g}_{2s's_2}(\lambda, \boldsymbol{q}_0, \boldsymbol{K}_2 + \frac{\boldsymbol{q}_0}{2})}{\Omega_{1,s_1}(\boldsymbol{K}_1) - \Omega_{2,s'}(\boldsymbol{K}_2 + \frac{\boldsymbol{q}_0}{2})} \right|^2 \right], \tag{C.5}$$

where $\boldsymbol{q}_0$ is the wave vector of phonon modes that conserve the energy $\Omega_{2,s_2}(\boldsymbol{K}_2) = \Omega_{1,s_1}(\boldsymbol{K}_1) - \hbar\omega_{2,\lambda}(\boldsymbol{q})$.

Performing a similar procedure, we get the following expression for the total exciton transfer rate between parallel CNTs

$$\Gamma(s_1, \boldsymbol{K}_1) = \frac{1}{\hbar} \sum_{s_2, \boldsymbol{K}_{2,0}} \sum_{\lambda,\mu} \frac{n_\lambda(\boldsymbol{q}_0) + 1}{|\frac{1}{2}\dot{\Omega}_{2,s_2}(\boldsymbol{K}_{2,0}) - \hbar\dot{\omega}_{2,\lambda}(\boldsymbol{q}_0)|} \times \cdots \\ \cdots \left| \sum_{s'} \frac{M_\parallel(\boldsymbol{K}_1, s_1; \boldsymbol{K}_{2,0} + \frac{\boldsymbol{q}_0}{2}, s') \; \tilde{g}_{2s's_2}(\lambda, \boldsymbol{q}_0, \boldsymbol{K}_{2,0} + \frac{\boldsymbol{q}_0}{2})}{\Omega_{1,s_1}(\boldsymbol{K}_1) - \Omega_{2,s'}(\boldsymbol{K}_{2,0} + \frac{\boldsymbol{q}_0}{2})} \right|^2, \tag{C.6}$$

where $\boldsymbol{q}_0$ and $\boldsymbol{K}_{2,0}$ are the wave vectors of phonon and excitonic states that conserve both energy and momentum: $\Omega_{2,s_2}(\boldsymbol{K}_{2,0}) = \Omega_{1,s_1}(\boldsymbol{K}_1) - \hbar\omega_{1,\lambda}(\boldsymbol{q}_0)$ and $\boldsymbol{K}_{2,0} = \boldsymbol{K}_1 - \frac{\boldsymbol{q}_0}{2}$.

LIST OF REFERENCES

[1] T. A. Shastry and M. C. Hersam, "Carbon nanotubes in thin-film solar cells," *Adv. Energy Mater.*, vol. 6, p. 1601205, 2016.

[2] R. B. Weisman and S. M. Bachilo, "Dependence of optical transition energies on structure for single-walled carbon nanotubes in aqueous suspension: An empirical kataura plot," *Nano Lett.*, vol. 3, p. 1235, 2003.

[3] S. Iijima, "Helical microtubules of graphitic carbon," *Nature*, vol. 354, no. 6348, pp. 56–58, 1991.

[4] S. Iijima and T. Ichihashi, "Single-shell carbon nanotubes of 1-nm diameter," *Nature*, vol. 363, p. 603, 1993.

[5] R. Saito, M. Fujita, G. Dresselhaus, and M. S. Dresselhaus, "Electronic structure of chiral graphene tubules," *Appl. Phys. Lett.*, vol. 60, pp. 2204–2206, 1992.

[6] R. Saito, G. Dresselhaus, and M. S. Dresselhaus, *Physical properties of carbon nanotubes*, vol. 35. World Scientific, 1998.

[7] P. Avouris, M. Freitag, and V. Perebeinos, "Carbon-nanotube photonics and optoelectronics," *Nature Photonics*, vol. 2, pp. 341–350, 2008.

[8] P. Avouris, Z. Chen, and V. Perebeinos, "Carbon-based electronics," *Nature nanotechnology*, vol. 2, pp. 605–615, 2007.

[9] M. D. Volder, S. H. Tawfick, R. H. Baughman, and A. J. Hart, "Carbon nanotubes: present and future commercial applications," *science*, vol. 339, pp. 535–539, 2013.

[10] M. S. Arnold, A. A. Green, J. F. Hulvat, S. I. Stupp, and M. C. Hersam, "Sorting carbon nanotubes by electronic structure using density differentiation," *Nature Nanotechnology*, vol. 1, pp. 60–65, 2006.

[11] M. Gong, T. A. Shastry, Y. Xie, M. Bernardi, D. Jasion, K. A. Luck, T. J. Marks, J. C. Grossman, S. Ren, and M. C. Hersam, "Polychiral semiconducting carbon nanotube–fullerene solar cells," *Nano Lett.*, vol. 14, pp. 5308–5314, 2014.

[12] G. M. Mutlu, G. Budinger, A. A. Green, D. Urich, S. Soberanes, S. E. Chiarella, G. F. Alheid, D. R. McCrimmon, I. Szleifer, and M. C. Hersam, "Biocompatible nanoscale dispersion of single-walled carbon nanotubes minimizes in vivo pulmonary toxicity," *Nano Lett.*, vol. 10, pp. 1664–1670, 2010.

[13] H. Kataura, Y. Kumazawa, Y. Maniwa, I. Umezu, S. Suzuki, Y. Ohtsuka, and Y. Achiba, "Optical properties of single-wall carbon nanotubes," *Synthetic metals*, vol. 103, pp. 2555–2558, 1999.

[14] M. Bernardi, J. Lohrman, P. V. Kumar, A. Kirkeminde, N. Ferralis, J. C. Grossman, and S. Ren, "Nanocarbon-based photovoltaics," *ACS nano*, vol. 6, pp. 8896–8903, 2012.

[15] S. M. Bachilo, M. S. Strano, C. Kittrell, R. H. Hauge, R. E. Smalley, and R. B. Weisman, "Structure-assigned optical spectra of single-walled carbon nanotubes," *Science*, vol. 298, pp. 2361–2366, 2002.

[16] K. Aitola, K. Sveinbjörnsson, J. Correa-Baena, A. Kaskela, A. Abate, Y. Tian, E. Johansson, M. Grätzel, E. I. Kauppinen, A. Hagfeldt, and G. Boschloo, "Carbon nanotube-based hybrid hole-transporting material and selective contact for high efficiency perovskite solar cells," *Energy & Environmental Science*, vol. 9, pp. 461–466, 2016.

[17] T. P. Tyler, T. A. Shastry, B. J. Leever, and M. C. Hersam, "Narrow diameter distributions of metallic arc discharge single-walled carbon nanotubes via dual-iteration density gradient ultracentrifugation," *Advanced Materials*, vol. 24, pp. 4765–4768, 2012.

[18] M. J. O'Connell, S. M. Bachilo, C. B. Huffman, V. C. Moore, M. S. Strano, E. H. Haroz, K. L. Rialon, P. J. Boul, W. H. Noon, C. Kittrell, J. Ma, R. H. Hauge, R. B. Weisman, and R. E. Smalley, "Band gap fluorescence from individual single-walled carbon nanotubes," *Science*, vol. 297, p. 5581, 2002.

[19] L. Huang, H. N. Pedrosa, and T. D. Krauss, "Ultrafast ground-state recovery of single-walled carbon nanotubes," *Phys. Rev. Lett.*, vol. 93, p. 017403, 2004.

[20] S. M. Tabakman, K. Welsher, G. Hong, and H. Dai, "Optical properties of single-walled carbon nanotubes separated in a density gradient: length, bundling, and aromatic stacking effects," *J. Phys. Chem. C*, vol. 114, p. 19569, 2010.

[21] R. Saito, G. Dresselhaus, and M. S. Dresselhaus, "Trigonal warping effect of carbon nanotubes," *Phys. Rev. B*, vol. 61, p. 2981, 2000.

[22] G. G. Samsonidze, R. Saito, N. Kobayashi, A. Gruneis, J. Jiang, A. Jorio, S. G. Chou, G. Dresselhaus, and M. S. Dresselhaus, "Family behavior of the optical transition energies in single-wall carbon nanotubes of smaller diameters," *Appl. Phys. Lett.*, vol. 85, p. 5703, 2004.

[23] T. Ando, "Excitons in carbon nanotubes," *J. Phys. Soc. Jpn.*, vol. 66, p. 1066, 1997.

[24] F. Wang, G. Dukovic, L. E. Brus, and T. F. Heinz, "The optical resonances in carbon nanotubes arise from excitons," *Science*, vol. 308, p. 838, 2005.

[25] C. L. Kane and E. J. Mele, "Ratio problem in single carbon nanotube fluorescence spectroscopy," *Phys. Rev. Lett.*, vol. 90, p. 207401, 2003.

[26] J. Maultzsch, R. Pomraenke, S. Reich, E. Chang, D. Prezzi, A. Ruini, E. Molinari, M. S. Strano, C. Thomsen, and C. Lienau, "Exciton binding energies in carbon nanotubes from two-photon photoluminescence," *Phys. Rev. B*, vol. 72, p. 241402(R), 2005.

[27] C. D. Spataru, S. Ismail-Beigi, L. X. Benedict, and S. G. Louie, "Excitonic effects and optical spectra of single-walled carbon nanotubes," *Phys. Rev. Lett.*, vol. 92, p. 077402, 2004.

[28] V. Perebeinos, J. Tersoff, and P. Avouris, "Scaling of excitons in carbon nanotubes," *Phys. Rev. Lett.*, vol. 92, p. 257402, 2004.

[29] T. G. Pedersen, "Variational approach to excitons in carbon nanotubes," *Phys. Rev. B*, vol. 67, p. 073401, 2003.

[30] S. K. Doorn, P. T. Araujo, K. Hata, and A. Jorio, "Excitons and exciton-phonon coupling in metallic single-walled carbon nanotubes: Resonance raman spectroscopy," *Phys. Rev. B*, vol. 78, p. 165408, 2008.

[31] F. Wang, D. J. Cho, B. Kessler, J. Deslippe, P. J. Schuck, S. G. Louie, A. Zettl, T. F. Heinz, and Y. R. Shen, "Observation of excitons in one-dimensional metallic single-walled carbon nanotubes," *Phys. Rev. Lett.*, vol. 99, p. 227401, 2007.

[32] P. May, H. Telg, G. Zhong, J. Robertson, C. Thomsen, and J. Maultzsch, "Observation of excitonic effects in metallic single-walled carbon nanotubes," *Nano Lett.*, vol. 82, p. 195412, 2010.

[33] R. Loudon, "One-dimensional hydrogen atom," *Am. J. Phys.*, vol. 27, p. 649, 1959.

[34] R. B. Capaz, C. D. Spataru, S. Ismail-Beigi, and S. G. Louie, "Diameter and chirality dependence of exciton properties in carbon nanotubes," *Phys. Rev. B*, vol. 74, p. 121401, 2006.

[35] C. D. Spataru, S. Ismail-Beigi, L. X. Benedict, and S. G. Louie, "Quasiparticle energies, excitonic effects and optical absorption spectra of small-diameter single-walled carbon nanotubes," *Appl. Phys. A*, vol. 78, pp. 1129–1136, 2004.

[36] E. Chang, G. Bussi, A. Ruini, and E. Molinari, "Excitons in carbon nanotubes: An ab initio symmetry-based approach," *Phys. Rev. Lett.*, vol. 92, p. 196401, 2004.

[37] C. D. Spataru, S. Ismail-Beigi, R. B. Capaz, and S. G. Louie, "Theory and ab initio calculation of radiative lifetime of excitons in semiconducting carbon nanotubes," *Phys. Rev. Lett.*, vol. 95, p. 247402, 2005.

[38] J. Jiang, R. Saito, G. G. Samsonidze, A. Jorio, S. G. Chou, G. Dresselhaus, , and M. S. Dresselhaus, "Chirality dependence of exciton effects in single-wall carbon nanotubes: Tight-binding model," *Phys. Rev. B*, vol. 75, p. 035407, 2007.

[39] A. Hagen, G. Moos, V. Talalaev, and T. Hertel, "Electronic structure and dynamics of optically excited single-wall carbon nanotubes," *Appl. Phys. A*, vol. 78, p. 1137, 2004.

[40] F. Wang, G. Dukovic, L. E. Brus, and T. F. Heinz, "Time-resolved fluorescence of carbon nanotubes and its implication for radiative lifetimes," *Phys. Rev. Lett.*, vol. 92, p. 177401, 2004.

[41] V. Perebeinos, J. Tersoff, and P. Avouris, "Radiative lifetime of excitons in carbon nanotubes," *Nano Letters*, vol. 5, p. 2495, 2005.

[42] A. Hagen, M. Steiner, M. B. Raschke, C. Lienau, T. Hertel, H. Qian, A. J. Meixner, and A. Hartschuh, "Exponential decay lifetimes of excitons in individual single-walled carbon nanotubes," *Phys. Rev. Lett.*, vol. 95, p. 197401, 2005.

[43] J. Kono, G. N. Ostojic, S. Zaric, M. S. Strano, V. C. Moore, J. Shaver, R. H. Hauge, and R. E. Smalley, "Ultra-fast optical spectroscopy of micelle-suspended single-walled carbon nanotubes," *Appl. Phys. A*, vol. 78, p. 1093, 2004.

[44] G. N. Ostojic, S. Zaric, J. Kono, M. S. Strano, V. C. Moore, R. H. Hauge, and R. E. Smalley, "Interband recombination dynamics in resonantly excited single-walled carbon nanotubes," *Phys. Rev. Lett.*, vol. 92, p. 117402, 2004.

[45] Y.-Z. Ma, J. Stenger, J. Zimmermann, S. M. Bachilo, R. E. Smalley, R. B. Weisman, and G. R. Fleming, "Ultrafast carrier dynamics in single-walled carbon nanotubes probed by femtosecond spectroscopy," *J. Chem. Phys.*, vol. 120, p. 3368, 2004.

[46] M. W. Graham, J. Chmeliov, Y.-Z. Ma, H. Shinohara, A. A. Green, M. C. Hersam, L. Valkunas, and G. R. Fleming, "Exciton dynamics in semiconducting carbon nanotubes," *J. Phys. Chem. B*, vol. 115, p. 5201, 2010.

[47] C. Manzoni, A. Gambetta, E. Menna, M. Meneghetti, G. Lanzani, and G. Cerullo, "Intersubband exciton relaxation dynamics in single-walled carbon nanotubes," *Phys. Rev. B*, vol. 94, p. 207401, 2005.

[48] P. H. Tan, A. G. Rozhin, T. Hasan, P. Hu, V. Scardaci, W. I. Milne, and A. C. Ferrari, "Photoluminescence spectroscopy of carbon nanotube bundles: Evidence for exciton energy transfer," *Phys. Rev. Lett.*, vol. 99, p. 137402, 2007.

[49] G. D. Scholes, "Long-range resonance energy transfer in molecular systems," *Annu. Rev. Phys. Chem.*, vol. 54, p. 57, 2003.

[50] T. Koyama, Y. Miyata, K. Asaka, H. Shinohara, Y. Saito, and A. Nakamura, "Ultrafast energy transfer of one-dimensional excitons between carbon nanotubes: a femtosecond time-resolved luminescence study," *J. Phys. Chem. Lett.*, vol. 2, p. 127, 2010.

[51] A. Maeda, S. Matsumoto, H. Kishida, T. Takenobu, Y. Iwasa, H. Shimoda, O. Zhou, M. Shiraishi, and H. Okamoto, "Gigantic optical stark effect and ultrafast relaxation of excitons in single-walled carbon nanotubes," *J. Phys. Soc. Jpn.*, vol. 75, p. 043709, 2006.

[52] T. Koyama, K. Asaka, N. Hikosaka, H. Kishida, Y. Saito, and A. Nakamura, "Ultrafast exciton energy transfer in bundles of single-walled carbon nanotubes," *J. Phys. Chem. Lett.*, vol. 2, p. 127, 2010.

[53] S. Berger, C. Voisin, G. Cassabois, C. Delalande, and P. Roussignol, "Temperature dependence of exciton recombination in semiconducting single-wall carbon nanotubes," *Nano Lett.*, vol. 7, p. 398, 2007.

[54] H. Qian, C. Georgi, N. Anderson, A. A. Green, M. C. Hersam, L. Novotny, and A. Hartschuh, "Exciton energy transfer in pairs of single-walled carbon nanotubes," *Nano Letters*, vol. 8, p. 1363, 2008.

[55] L. Lüer, J. Crochet, T. Hertel, G. Cerullo, and G. Lanzani, "Ultrafast excitation energy transfer in small semiconducting carbon nanotube aggregates," *ACS Nano*, vol. 4, p. 4265, 2010.

[56] R. D. Mehlenbacher, M. Y. Wu, M. Grechko, J. E. Laaser, M. S. Arnold, and M. T. Zanni, "Photoexcitation dynamics of coupled semiconducting carbon nanotubes thin films," *Nano Lett.*, vol. 97, p. 091905, 2013.

[57] M. Grechko, Y. Ye, R. D. Mehlenbacher, T. J. McDonough, M. Y. We, R. M. Jacobbreger, M. S. Arnold, and M. T. Zanni, "Diffusion-assisted photoexcitation transfer in coupled semiconducting carbon nanotube thin films," *ACS Nano*, vol. 8, p. 5383, 2014.

[58] R. D. Mehlenbacher, T. J. McDonough, M. Grechko, M.-Y. Wu, M. S. Arnold, and M. T. Zanni, "Energy transfer pathways in semiconducting carbon nanotubes revealed using two-dimensional white-light spectroscopy," *Nature Commiunications*, vol. 6, p. 6732, 2015.

[59] C. Y. Wong, C. Curutchet, S. Tretiak, and G. D. Scholes, "Ideal dipole approximation fails to predict electronic coupling and energy transfer between semiconducting single-wall carbon nanotubes," *J. Chem. Phys.*, vol. 130, p. 081104, 2009.

[60] O. Postupna, H. M. Jaeger, and O. V. Prezhdo, "Photoinduced dynamics in carbon nanotube aggregates steered by dark excitons," *J. Phys. Chem. Lett.*, vol. 5, pp. 3872–3877, 2014.

[61] A. R. Nugraha, R. Saito, K. Sato, P. T. Araujo, A. Jorio, and M. S. Dresselhaus, "Dielectric constant model for environmental effects on the exciton energies of single wall carbon nanotubes," *Appl. Phys. Lett.*, vol. 13, p. 1495, 2013.

[62] V. N. Popov, L. Henrard, and P. Lambin, "Resonant raman intensity of the radial breathing mode of single-walled carbon nanotubes within a nonorthogonal tight-binding model," *Nano Letters*, vol. 4, p. 1795, 2004.

[63] M. Rohlfing and S. G. Louie, "Electron-hole excitations and optical spectra from first principles," *Phys. Rev. B.*, vol. 62, p. 4927, 2000.

[64] N. E. Brener, "Screened-exchange plus coulomb-hole correlated hartree-fock energy bands for lif," *Phys. Rev. B*, vol. 11, p. 1600, 1975.

[65] H. Zhao and S. Mazumdar, "Electron-electron interaction effects on the optical excitations of semiconducting single-walled carbon nanotubes," *Phys. Rev. Lett.*, vol. 93, p. 157402, 2004.

[66] E. B. Barros, R. B. Capaz, A. Jorio, G. G. Samsonidze, A. G. S. Filho, S. Ismail-Beigi, C. D. Spataru, S. G. Louie, G. Dresselhaus, and M. S. Dresselhaus, "Selection rules for one- and two-photon absorption by excitons in carbon nanotubes," *Phys. Rev. B*, vol. 73, p. 241406(R), 2006.

[67] B. P. Krueger, G. D. Scholes, and G. R. Fleming, "Calculation of couplings and energy-transfer pathways between the pigments of lh2 by the ab initio transition density cube method," *J. Phys. Chem. B*, vol. 102, p. 5378, 1998.

[68] J. C. Chang, "Monopole effects on electronic excitation interactions between large molecules. i. application to energy transfer in chlorophylls," *J. Chem. Phys.*, vol. 67, p. 3901, 1977.

[69] E. Malic, J. Maultzsch, S. Reich, and A. Knorr, "Excitonic absorption spectra of metallic single-walled carbon nanotubes," *Phys. Rev. B*, vol. 82, p. 035433, 2010.

[70] R. D. Mehlenbacher, J. Wang, N. M. Kearns, M. J. Shea, J. T. Flach, T. J. McDonough, M. Y. Wu, M. S. Arnold, and M. Zanni, "Ultrafast exciton hopping observed in bare semiconducting carbon nanotube thin films with 2dwl spectroscopy," *J. of Phys. Chem. Lett.*, vol. 7, p. 2024, 2016.

[71] P. T. Araujo, A. Jorio, M. S. Dresselhaus, K. Sato, and R. Saito, "Diameter dependence of the dielectric constant for the excitonic transition energy of single-wall carbon nanotubes," *Phys. Rev. Lett.*, vol. 103, p. 146802, 2009.

[72] V. Perebeinos, J. Tersoff, and P. Avouris, "Effect of exciton-phonon coupling in the calculated optical absorption of carbon nanotubes," *Phys. Rev. Lett.*, vol. 94, p. 027402, 2005.

[73] J. J. Sakurai and J. Napolitano, *Modern quantum mechanics*. Addison-Wesley, 2011.

[74] Y. Toyozawa, "Theory of line-shapes of the exciton absorption bands," *Prog. Theor. Phys.*, vol. 20, pp. 53–81, 1958.

[75] B. Segall and G. Mahan, "Phonon-assisted recombination of free excitons in compound semiconductors," *Phys. Rev.*, vol. 171, p. 935, 1968.

[76] J. Jiang, R. Saito, K. Sato, J. S. Park, G. G. Samsonidze, A. Jorio, G. Dresselhaus, and M. S. Dresselhaus, "Exciton-photon, exciton-phonon matrix elements, and resonant raman intensity of single-wall carbon nanotubes," *Phys. Rev. B*, vol. 75, p. 035405, 2007.

[77] A. H. Davoody, F. Karimi, M. S. Arnold, and I. Knezevic, "Theory of exciton energy transfer in carbon nanotube composites," *J. Phys. Chem. C*, vol. 120, pp. 16354–16366, 2016.

[78] M. S. Arnold, J. L. Blackburn, J. J. Crochet, S. K. Doorn, J. G. Duque, A. Mohite, and H. Telg, "Recent developments in the photophysics of single-walled carbon nanotubes for their use as active and passive material elements in thin film photovoltaics," *Phys. Chem. Chem. Phys.*, vol. 15, p. 14896, 2013.